Electronic States of Correlated Transition Metal Oxides:
$Ca_{1-x}Sr_xVO_3$ and Sr_2RuO_4.

電子相関の強い遷移金属酸化物

$Ca_{1-x}Sr_xVO_3$とSr_2RuO_4の電子状態

井　上　　公

Electronic States of Correlated Transition Metal Oxides: $Ca_{1-x}Sr_xVO_3$ and Sr_2RuO_4.

Thesis
Submitted for the Degree of
Doctor of Science
in the University of Tokyo

by

Isao H. INOUE

Electrotechnical Laboratory,
Tsukuba 305-8568, Japan.

October 8th, 1998

Contents

List of Abbreviations

DOS density of state

FLAPW full-potential linear-augmented-plane-wave (band calculation)

FZ floating zone (method)

IPT iterated perturvation theory

LDA local density approximation

LHB lower Hubbard band

LISA local-impurity self-consistent approximation (for the large dimension Hubbard model)

MI metal-to-insulator (transition)

MIT metal-to-insulator transition

PES photoemission spectroscopy

RPES resonance photoemission spectroscopy

TG thermogravimetric (analysis)

TM transition metal

UHB upper Hubbard band

UPS ultra-violet photoemission spectroscopy

XAS x-ray absorption spectroscopy

XPS x-ray photoemission spectroscopy

XRD x-ray diffraction (spectroscopy)

Preface

Statement

I herein affirm that the matter embodied in this Thesis entitled 'Electronic States of Correlated Transition Metal Oxides: $Ca_{1-x}Sr_xVO_3$ and Sr_2RuO_4' is the result of investigations carried out since 1992 till 1998 mainly in the Electrotechnical Laboratory (ETL). The Thesis contains no material that has been published elsewhere, except where due reference has been made. Due acknowledgment has been made wherever the work described is based on the findings of other investigators. Any omission which might have occurred by oversight or error in judgment is regretted.

Acknowledgment

I began this study in 1992 when I joined the staff of ETL. My aim has been to explore a variety of phenomena associated with transition metal oxides, in which the electron correlations dominate the inter-atomic overlaps which give rise to conventional band pictures.

Although I had only experience in photoemission measurements in the graduate course, I decided to start this study by trying to prepare some kinds of perovskite-related vanadium oxides. Rather to my surprise, it took me the whole of the first year to produce a series of poly-crystalline $Ca_{1-x}Sr_xVO_3$ samples, and only very recently have I succeeded to produce a series of single-crystalline $Ca_{1-x}Sr_xVO_3$ samples with an immense help of my student O. Goto. Sufficient time has elapsed to undergo a number of improvements and updates made by the success of the single crystal growth, which has eventually forced me to spend a long term to complete this study.

Since I was a layman of this field, everything proved a difficult venture which could never be completed by myself within this long but actually a short period. Throughout this study, I was assisted by many people for sample preparation and characterization, for a variety of measurements, and for performing computer calculations. I would like to express my gratitude hereinafter to all to whom I am indebted.

In particular, I would like to thank my mentor A. Fujimori, an associate professor of University of Tokyo. I am grateful to him for the help he has extended to me for all these years. I have been inspired very much by his thought-provoking suggestions.

I would also like to thank the former leader of the Electron Physics Section, Y. Nishihara (now a professor of Ibaraki University), the director of the Physical Science Division, H. Shimizu, and the director-general of ETL, K. Kajimura, for giving me the opportunity to work in this institute and for their generous support.

I have been greatly supported by both present and former members of ETL, as well as the secretary, post-doctoral fellows and (intern) students from several universities who worked and studied there: H. Unoki, Y. Yamaguchi, K. Murata, K. Oka, H. Bando, F. Iga, A. Fukushima, Y. Aiura, H. Kawanaka, N. Shirakawa, T. Ito, I. Hase, Y. Tanaka, Y. Shimoi, S. Abe, N. A. Fortune, K. Koga, T. Maruyama, K. Morikawa, H. Fukuchi, H. Fu-

jiwara, Y. Haruyama, Y. Kodama, H. Makino, O. Goto, and K. Inoue, who have always instructed me on many experimental and theoretical techniques, and whose discussions and encouragement were the stimulus for much of this work; in particular, I am deeply indepted to Goto-kun and Makino-kun for their efforts with the single-crystal growth, to Hase-kun for his band calculations, and to Shirakawa-san who developed the LaTeX style files for this Thesis.

I gratefully acknowledge the valuable comments of T. Mizokawa, who was my classmate in the department of physics at the University of Tokyo. He first drew my attention to the importance of the $\vec{k}$-dependent self-energy in the interpretation of photoemission spectra. My thanks are also due to K. Matho, K. Kusakabe and T. Kotani for valuable discussions about the $\vec{k}$-dependent self-energy.

I wish to thank one of my best friends, Marcelo J. Rozenberg, who is now an associate professor of University of Buenos Aires, and who has always stimulated me with numerous discussions via email. We enjoyed fruitful collaborations especially during his one-month stays in ETL both in 1995 and 1996. Moreover, he kindly became a Santa Clause for my daughter. I would also like to thank his family for their kind hospitality during my stay in Paris in 1996.

I would like to express my special thanks to D. D. Sarma, an associate professor of Indian Institute of Science. I stayed in his group for one month in 1995 and again in 1998. He taught me philosophical aspects of physics which I will never forget. I would also like to thank his students, Kalobaran Maiti, Priya Mahadevan, Jagjit, Krishna, Shafi, Nimmi, Raghu, and Sudipta Barman; I was deeply impressed by their sincere attitude towards the research.

My thanks are also due to Nigel E. Hussey, who is now a postdoctoral fellow in ISSP, University of Tokyo and who performed a part of the electrical resistivity measurements of $Ca_{1-x}Sr_xVO_3$ when he first visited ETL from Cambridge. He also improved the quality of English of this Thesis considerably.

To my dismay, I discovered that it is impossible, at the end of this seven-year study, to recall all the other occasions at which I was given invaluable criticism, advice, and instruction. Among others, I am indepted to: A. Kakizaki, A. Kimura, A. Harasawa, A. Yagishita, T. Saito, Y. Tokura, Y. Maeno, S. Nishizaki, T. Fujita, Y. Ueda, S. Shin, M. Ishikawa, T. Oguchi, T. Tsujii, A. Yoshimori, G. A. Sawatzky, G. Kotliar, A. Georges, H. Nakotte, F. Lichtenberg, J. G. Bednorz, and N. W. Ashcroft.

Part of this work has been supported by the Sakigake-21 Grant [Precursor Research for Embryonic Science and Technology (PRESTO)] of Japan Science and Technology Corporation (JST). I would like to thank the staff of the 'Field and Reaction' office of the Sakigake-21 Grant, Mushiake-san, Yamauchi-san, and Shingu-san, for a lot of clerical work that helped to keep my budget afloat.

I regret that I could not complete this Thesis while my father was alive; he looked forward to seeing this. I dedicate this book to the memory of my late father.

Finally, I would like to express my most heartfelt thanks to my children, my mother, and my wife Asaka who never lost her faith in my ability; their support was always felt and appreciated across the distances.

Isao H. INOUE
September, 1998

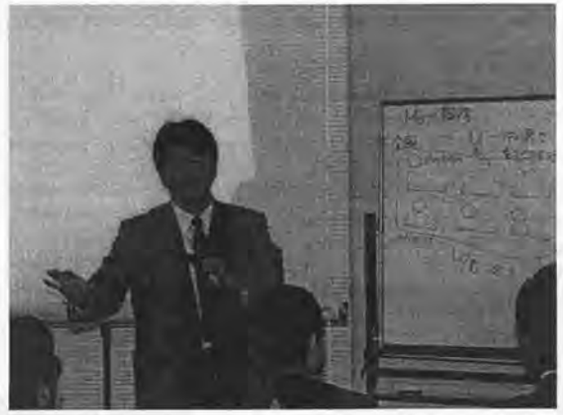

Chapter 1

Introduction and Scope

The aim of this Thesis is to explore anew the nature of the so-called "Mott Transition"[1] taking account of the issue that a nonlocal interaction may become important near the transition point from the correlated metal to the Mott insulator. Before going into the specialized topics described in the following chapters, we try to provide a perspective by giving here a concise introduction of the Mott transition and the perovskite-type transition metal oxides.

FIG. 1.1. Portrait of Sir Nevill Francis Mott, England (1905-1996).[2] He was awarded a Nobel Prize in 1977 with Philip Warren Anderson and John Van Vleck for their fundamental theoretical investigations of the electronic structure of magnetic and disordered systems. *Mott transition* is derived from his original work.[1]

1.1. Outline of the Mott transition

At the center of present-day interest in solid state physics is the whole comprehension of the electronic states of materials in the intermediate region between a simple metal and the so-called Mott insulator, dating back to the long-standing controversy about the itinerant versus localized features of electrons in some transition metal (TM) oxides.[3,4] In these systems, the on-site electron-electron repulsions U are comparable to the energies associated with the overlap of atomic orbitals belonging to different atoms, which are characterized in a solid by the one-electron bandwidth W.

Electron correlation plays an important role in most of the scenarios describing what happens in this system; the word *electron correlation* here signifies how much the dynamics of an electron are influenced by the occupancy of the one-electron states involved.

Let us at first illustrate this point briefly. Imagine the system contains N independent sites. If electrons with spin $\sigma = \uparrow$ are independent of those with $\sigma = \downarrow$, according to the Fermi-Dirac statistics, the number of available electronic configurations is 2^{2N} and thus the number of available one-electron states is $2N$. On the other hand, if no doubly occupied or empty site configurations are allowed, the number of available electronic configurations is reduced to 2^N and thereby the number of

the available one-electron states is N. This exclusion of the N one-electron states from the total $2N$ one-electron states is the simplest concept of strong *electron correlations*.

Actually, the large U eliminates doubly occupied states. In other words, a one-electron wave function can no longer be composed of a naive linear-combination of the atomic orbitals; it must incorporate the *conditional probability*, which expresses the dynamics of one-electron excitations in the presence of other electrons in the same shell.

A well-known historical example is NiO. If we calculate the electronic state of NiO within the independent electron approximation, we find that NiO is metallic with a partially filled d-band.[5] However, NiO is an insulator, because the electron correlations exclude most of the one-electron sites, which should be available in the independent electron approximation, and thus the effect of electron correlation forces NiO to behave as if it were a fully-filled band insulator; *i.e.*, charge fluctuation is completely suppressed. (It should be noted that the spin degrees of freedom are still alive.)

Let us describe this peculiar insulating state (the so-called Mott insulator) schematically, along with the Mott-Hubbard picture.[6,7] We imagine here that, in the half-filled system, the distance between the atoms is large, that the spins form an antiferromagnetic array, and that the system is thus insulating. Then, introduce an additional electron on atom i, and we denote the many-electron wave function of this state by Ψ_j^{N+1}. A state in which the added "electron" moves with wavenumber $\vec{k}$ can be described by the linear combination of Ψ_j^{N+1}, *i.e.*,

$$\sum_j e^{i\vec{k}\cdot\vec{a}_j}\Psi_j^{N+1}\,,$$

where $\vec{a}_j$ stands for lattice site j. These states form an energy band, which is called the upper Hubbard band (UHB). In the same way, if

FIG. 1.2. Portrait of Enrico Fermi, Italy (1901-1954).[2] He was awarded a Nobel Prize in 1938 for his demonstrations of the existence of new radioactive elements produced by neutron irradiation, and for his related discovery of nuclear reactions brought about by slow neutrons; absorption of neutrons. "Fermion" is named in his pioneering work.

an electron is removed from the atom j, and Ψ_j^{N-1} is the many-electron wave function of this system, then

$$\sum_j e^{i\vec{k}\cdot\vec{a}_j}\Psi_j^{N-1}$$

is the wave function representing the movement of this "hole." These states form an energy band called the lower Hubbard band (LHB).

If we neglect the long-range electron-hole interaction, a metal-insulator transition occurs if we increase the value of a, *i.e.*, decrease both the one-electron bandwidth $W_{\rm UHB}$ and $W_{\rm LHB}$. In the extreme case ($a \to \infty$), the separation of the energy becomes equal to the on-site electron-electron repulsion energy U, so, in the intermediate region, the metal-insulator transition is realized at

$$U = \frac{1}{2}\times(W_{\rm LHB}+W_{\rm UHB})\,.$$

FIG. 1.3. Portrait of Lev Davidovic Landau, Soviet Union (1908-1968).[2] He was awarded a Nobel Prize in 1962 for his pioneering theories of condensed matter, especially liquid helium. One of the most important concept in the solid state physics, "Landau Fermi liquid", was given birth by his excellent intuition and insight.

Actually, some materials in this

$$U \cong \frac{1}{2}\times(W_{\rm LHB}+W_{\rm UHB}) \equiv W$$

region, such as V_2O_3,[8] show a spectacular Mott transition (Mott-Hubbard transition) even under relatively small changes in either temperature, chemical doping, or pressure. The concepts of the Landau-Fermi liquid such as the Fermi surface or the quasiparticle are, however, believed to be still applicable even in this metallic phase near the Mott transition, although they suddenly lose meaning in the insulating phase, because no double occupancies of the same orbital state are allowed in the Mott insulating phase. Then, the only way to realize the Mott transition from the metallic phase based on the Fermi liquid theory is to realize the divergence of the single-particle mass. Thus, the following intriguing properties reported so far near the Mott transition boundary are considered to be the characteristics of the anomalous metallic state of the correlated electron system, especially, near the Mott transition; a large effective mass (with the mass-enhancement in the range of $2-10$), a large coefficient of the T^2 term in electrical resistivity at low temperature, a large spectral weight redistribution, and, in some cases, antiferromagnetic ordering with a small magnetic moment.[7,9]

Brinkman and Rice were the first to describe the mass enhancement in the correlated metal.[10] They used a method due to Gutzwiller,[11] by which the total energy of the system is minimized as a function of the fraction of doubly occupied states. This fraction η is expressed as

$$\eta \cong \frac{1}{4}\left(1-\beta\frac{U}{W}\right)\,.$$

where β is not far from unity. The mass enhancement in this framework is most simply obtained in the following way. Given that an electric field E acts for time δt, which is much smaller than the relaxation time, the electric current δj produced by $N\eta$ carriers of each sign is given by

$$\delta j = \left(\frac{2\eta N e^2\delta t}{m_{\rm o}}\right)E\,,$$

where $m_{\rm o}$ is the free electron mass. On the other hand, if we regard this current as due to the quasiparticle with effective mass m^*, it reads

$$\delta j = \left(\frac{Ne^2\delta t}{m^*}\right)E\,.$$

Equating these two, we find,

$$\frac{m^*}{m_{\rm o}} = \frac{1}{2\eta}\,,$$

which is the famous Brinkman and Rice's result.

However, the adiabatic continuity, which is the major premise of the Fermi liquid theory approach, cannot be satisfied when the interaction breaks the symmetry of the

FIG. 1.4. Portrait of Charles Augustin de Coulomb, France (1736-1806).[2] The famous "Coulomb's law" was derived from his study for electrostatic charges, in which he observed that the force between charges behaves as the reciprocal of the square of the distance between them. The SI unit of electrical charge, the Coulomb, is named in his honor.

spin or orbital degrees of freedom. In addition, near the Mott transition boundary, the positive Coulomb interaction and the negative band energies are of comparable magnitude and therefore almost compensate each other. Hence, much smaller (long range) exchange/correlation energy, or entropic (thermal) or atomic disorder contributions to the total free energy might produce qualitative changes in the nature of the many-electron states. From this kind of viewpoint, we investigate in this Thesis the spectral weight transfer and effective mass of some correlated electron systems.

1.2. Perovskite-type transition metal oxides

Most of the compounds with the general formula of ABO_3 have the perovskite structure. The atomic arrangement in this structure was first found for mineral "perovskite" $CaTiO_3$. The unit cell of ABO_3 is represented by the A ions at the corners of a cube with B ions at the body center and the oxygen ions at the center of the faces (Fig. 1.5). The BO_6 octahedron forms a three-dimensional network, so that, if the system is metallic, electric conduction is three-dimensional along this BO_6 network. In the perovskite-type oxides, the A cation is coordinated with twelve oxygen ions, and the B cation with six. Thus, the ionic radius of the A cation is normally found to be somewhat larger than that of the B cation. Therefore, the largest number of perovskite-type compounds are described by the general formula $A^{2+}B^{4+}O_3$, where the A^{2+} cations are alkaline-earth ions, cadmium, lead and so on, while the B^{4+} cations are TM and some rare-earth ions, which are, in general, smaller than the candidates of the A site. A diagrammatic presentation of the crystal structure with respect to the ionic radii of the A and B cations for $A^{2+}B^{4+}O_3$ type compounds as well as the $A^{3+}B^{3+}O_3$ are shown in Figs. 1.6 and 1.7, respectively.[12] The boundaries are determined from room-temperature experimental studies. Although there are some discrepancies, especially for ferroelectric materials, in this diagram, it still holds well for many compounds and is very instructive.

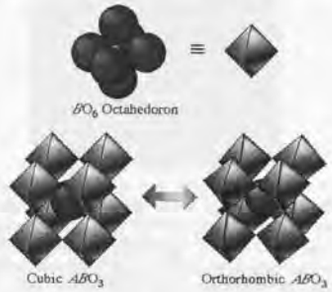

FIG. 1.5. Perovskite structure, ABO_3. The A ion is surrounded by the eight BO_6 octahedra. The tilting of the BO_6 octahedra changes the lattice symmetry from cubic to orthorhombic, tetragonal, or rhombohedral.

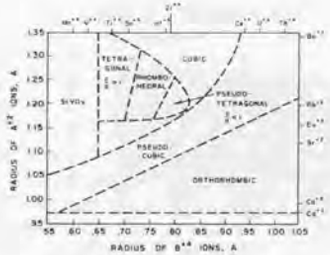

FIG. 1.6. Classification of the structure for the $A^{2+}B^{4+}O_3$ type compounds.[12]

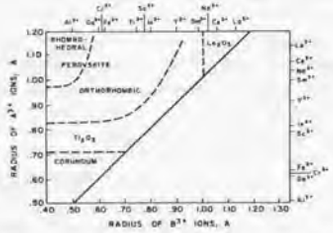

FIG. 1.7. Classification of the structure for the $A^{3+}B^{3+}O_3$ type compounds.[12]

If the A ion is at the body center, then the oxygen ions are at the edges and the B ions are at the corners. In the K_2NiF_4 structure, the ABO_3 unit cell with the A ions at the body center is placed on the other type of ABO_3 unit cell with the B ions at the body center (Fig. 1.8). (Note that we can regard the boundary of these two types of stacking cells as the NaCl-type structure.) This is often called a layered perovskite structure. The BO_6 octahedron forms, in this case, a two-dimensional network, so that the electronic properties of the materials can be anisotropic; in particular cases, it can even be two-dimensional.

Perovskite-type transition metal oxides

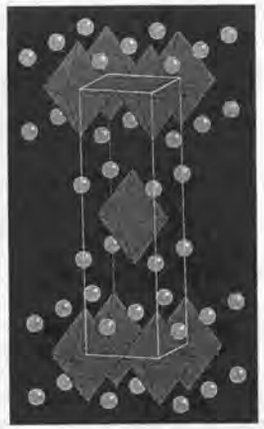

FIG. 1.8. K_2NiF_4 structure: an alternation of the two types of ABO_3 unit. This structure is often called a layered perovskite.

ABO_3, with B a transition metal cation, provide us with an ideal stage on which to study the electron correlations in solids. It is considered to be the most important advantage of the perovskite structure that the BO_6 network is stable for substitutions of the A-site ion, which is completely ionized in most cases without contributing to the band formation. By this ionization of the A-site, electrons are left in the oxygen $2p$ bands and/or the TM $3d$ bands.

Then, there are three strategies for investigating the systematic development of the electronic states with this ABO_3 compounds.[13]

filling control Nominal number of conduction electrons per unit formula is controlled by the chemical substitution of an A ion for that of different valence.

bandwidth control B–O–B bond angle can be changed by changing the ionic radius of the A-site ion. The bond-angle buck-

ling is governed by the so-called tolerance factor f of the perovskite-type compounds ABO_3 defined as

$$f = \frac{R_A + R_O}{\sqrt{2}\,(R_B + R_O)},$$

where R_A, R_O, and R_B are the ionic radii of the A ion, the O ion (oxygen), and the B ion, respectively. When the value of f is almost 1, the system is cubic; while for $f < 1$, the lattice structure changes to rhombohedral and then to the orthorhombic $GdFeO_3$ type. In the orthorhombic perovskite structure, it is known that the B–O–B bond angle decreases continuously with decreasing f almost irrespective of the set of A and B.[14] The buckling of the B–O–B bond angle reduces W, since the effective d-electron transfer interaction between the neighboring B sites is governed by the super-transfer process via the O $2p$ state. Thus, the ratio of U to W (U is considered to be kept almost constant by the substitution) can be systematically controlled.

dimension control By changing the crystal structure from the simple perovskite to the layered perovskite, we can follow how the electronic states change by reducing the network paths of the system.

Accordingly, the perovskite-type TM oxides are ideal systems in which one can control the filling of the d band and the ratio U/W intentionally.

Anomalous electronic properties in a metallic phase near the Mott transition have provoked a great deal of controversy for a long time, and have been investigated anew since the discovery of the high-T_c cuprate superconductors with layered perovskite structures.[15] A number of enlightening works have been done so far in this field,[16] especially for the perovskite-type TM oxides, by controlling the $3d$ band-filling and the $3d$ bandwidth. These studies are summarized in a schematic phase diagram shown in Fig. 1.9.[13]

The four thin lines, which connect the circles representing TM cations at the B site, correspond to $A = Y^{3+}$, La^{3+}, Ca^{2+} and Sr^{2+}. U is the electron-electron repulsion energy, W is the one-electron bandwidth, and Δ is the charge transfer energy between the transition metal $3d$ band and the oxygen $2p$ band. "Charge-transfer insulator" is beyond the scope of this Thesis but is an important concept to understand the physics of TM oxides: in the charge-transfer insulator, the charge gap opens between the highest occupied one-electron state in the O $2p$ band and the lowest unoccupied one-electron states in the TM $3d$ band, which are eliminated from the occupied one-electron states in TM $3d$ band by the electron correlations. Within a simple independent-electron theory, all the materials in Fig. 1.9 except for the d^0 band insulator should be metallic. However, several compounds in the shaded portion are insulating, *i.e.*, Mott insulators due to the presence of strong electron correlations.

Although the history of the study of perovskite-type TM oxides is very long, we have not yet been able to grasp a comprehensive view of the physics. The phase diagram (Fig. 1.9) can become a kind of map in order to dig out a gold mine; as the English saying goes, "a new mine of wealth in the narratives of forgotten Englishmen."

1.3. Scope

In this Thesis, two perovskite-related systems are studied. One is the vanadium oxides, $Ca_{1-x}Sr_xVO_3$. We have synthesized a solid solution of the perovskite-type metallic vanadates, $CaVO_3$, $SrVO_3$, and their solid-solutions $Ca_{1-x}Sr_xVO_3$, each of which holds nominally one $3d$ electron per vanadium ion. In the $Ca_{1-x}Sr_xVO_3$ system, as we isovalently substitute a Ca^{2+} ion for a Sr^{2+} ion, a lattice distortion occurs. Then, we can see how the electronic states change as we change the bandwidth systematically.

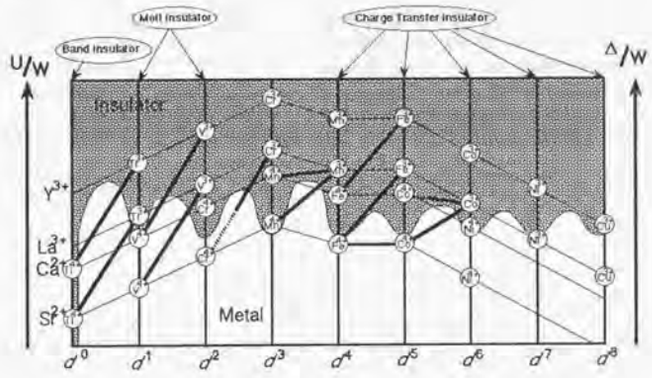

FIG. 1.9. Schematic phase diagram of ABO_3 for $A = Y^{3+}$, La^{3+}, Ca^{2+} and Sr^{2+}. U is the electron-electron repulsion energy, W is the one-electron bandwidth, and Δ is the charge transfer energy between the transition metal $3d$ band and the oxygen $2p$ band.

The other is the superconducting Sr_2RuO_4 with a layered-perovskite structure, which is the same crystal structure as that of $La_{2-x}Ba_xCuO_4$. Sr_2RuO_4 exhibits superconductivity below $T_c = 1.50\,K$. The effect of low-dimensionality is studied.

First of all, some of the experimental and calculational methods are reviewed in Chapter 2. The methods described there are rather fundamental and quite generally applicable to a variety of materials.

In Chapter 3, we report electronic properties of $CaVO_{3-\delta}$ observed by delicately controlling the oxygen stoichiometry. Drastic and unconventional changes of magnetoresistance, magnetic susceptibility, and Hall effect in single-crystalline $CaVO_{3-\delta}$ ($\delta > 0$) are shown.

We describe the method of preparing single crystals of a new vanadate system $Ca_{1-x}Sr_xVO_3$ in Chapter 4. The cubic-orthorhombic lattice distortion, magnetic susceptibility measurements, electronic specific heat coefficient, and electric resistivity data are described in this Chapter 4.

X-ray and ultraviolet photoelectron spectroscopy spectra of $Ca_{1-x}Sr_xVO_3$ for several values of x are reported in Chapter 5. The photoemission spectra of $Ca_{1-x}Sr_xVO_3$ are different from the density of states obtained by band calculations using the local density approximation; a fingerprint of the presence of strong electron correlations in this system. We also report a novel metal-insulator transition, which is only realized at the surface of $Ca_{1-x}Sr_xVO_3$ with the change of x, while the bulk remains metallic. Optical conductivity of $Ca_{1-x}Sr_xVO_3$ is discussed in an Appendix, which gives complementary and interesting information on the electronic states of this system.

Photoemission spectrum of Sr_2RuO_4 is described in Chapter 6. The surface deterioration and concomitant change of the spec-

tral shape, results of resonance photoemission spectroscopy, and evidence for significant spectral weight redistribution of the Ru $4d$ band are discussed in this chapter.

In Chapters 4, 5, and 6, we also discuss the effect of nonlocal electron correlations in order to explain the missing critical enhancement of the effective mass and the large spectral weight redistribution consistently.

Chapter 2

Review of Experimental Techniques and Calculations

In this chapter, some of the experimental and calculational methods, which were used in this study, are described. The sample preparation methods shown in the first two sections were applied to the study of $Ca_{1-x}Sr_xVO_3$ material, while the Sr_2RuO_4 samples have been synthesized and characterized by Maeno's group in Kyoto University and others. Thereby, the first section of sample preparation is not a general review but rather a recipe how to prepare the $Ca_{1-x}Sr_xVO_3$ material. Although especially the details of sample preparation techniques are different from material to material, the methods described as follows are rather fundamental and quite generally applicable to a variety of materials.

2.1. Sample Preparation

2.1.1. Solid State Synthesis

A 'ceramic method' was employed in order to prepare polycrystalline samples. 4N $CaCO_3$, $SrCO_3$, and VO_2 were used as starting reagents. We prepared CaO and dried $SrCO_3$ by preheating both the $CaCO_3$ and $SrCO_3$ compounds in air for 24 h at 1000°C, and weighed the powders while they were still over 100°C. We confirmed that the dried CaO and $SrCO_3$, as well as VO_2, were all single phase by x-ray diffraction (XRD). The starting compounds, CaO, $SrCO_3$, and VO_2 were then mixed in the required molar ratio $Ca : Sr : V = 1 - x : x : 1$ and then calcined several times at 1250 °C in flowing argon atmosphere (~ 1000 cc/min) with intermittent grindings. Because the reaction proceeds in the solid state, the reaction rate depends on the diffusion rate of the constituents through the product phases. As the reaction proceeds, diffusion paths become longer, and hence the reaction rate decreases. Therefore the intermittent mechanical grinding of the reaction product is important in this method.

As the Sr concentration is increased, it is required to add hydrogen gas at a rate up to ~ 50 cc/min. The amount of hydrogen gas flow for each calcination process must be controlled in order to avoid too much reduction and peroxidization. The amount of the oxidation was conveniently checked by examining the XRD spectrum, *i.e.*, the lattice constants, of the reaction product every time after the intermittent grinding. This process was repeated until completion of the reaction.

Finally, the powder was put into rubber tubes and each tube was pressed under hydrostatic pressure of 1000 atm to form a cylindrical rod of ~ 6 mm diameter and ~ 10 cm length. The rods were sintered at 1300°C in the same atmosphere described above.

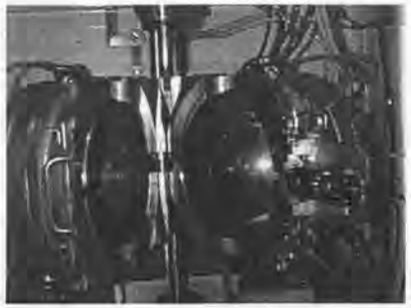

FIG. 2.1. Infrared-radiation furnace (Type SC-N35HD, Nichiden Machinery Ltd.) with two 1.5 kW halogen lamps as radiation sources.

2.1.2. Floating Zone Method

Single crystals of $Ca_{1-x}Sr_xVO_3$ were grown by the floating zone (FZ) method in an infrared-radiation furnace (type SC-N35HD, Nichiden Machinery Ltd.) with two 1.5-kW halogen lamps as radiation sources (Fig. 2.1). At first, the sintered rod is cut into two parts: one is ~ 2 cm long for the "seed" rod, which is held at the top of the lower shaft, and the rest of the sintered rod, called the "feed" rod, is suspended at the bottom of the upper shaft. If possible, it is desirable to use a piece of exprepared single crystal as the seed rod. Each rod is rotated at ~ 20 rpm in opposite directions. The lamp power is raised gradually until both of the rods are melted, then the molten zone is attached to the top of the seed. The molten zone is passed through the whole feed rod at a rate of ~ 1 cm/h in flowing argon atmosphere without any interruption or change of lamp power.

2.2. Sample Characterization

2.2.1. X-ray Diffraction Measurements

Powder x-ray diffraction (XRD) measurement is the most convenient method to characterize the samples. Each time we prepared samples, a small part or, in some cases, the whole of the sample was pulverized for the XRD measurement. The powder was attached on a slide by a piece of double-sided adhesive tape and mounted on a commercial x-ray diffractometer with Cu $K\alpha_{1,2}$ radiation (Philips, PW). The wavelength λ was taken to be 1.54051 Å for $K\alpha_1$ and 1.54433 Å for $K\alpha_2$. 2θ was swept from 10° to 120° at 0.05° step. All the measurements were performed at room temperature. The observed XRD spectra of $CaVO_3$ and $SrVO_3$ were compared with the reported data in the Powder Diffraction File compiled by the Joint Committee on Powder Diffraction Standards (JCPDS). By indexing the h, k, l values to each peak in XRD spectra according to the JCPDS file, the lattice constants have been determined. Peak positions of the observed spectra were read off manually, taking the midpoint of the full width at half maximum.

In order to quarry single-crystalline samples with an appropriate crystallographic geometry out of the rod prepared by the FZ method, we took Laue photographs with a commercial apparatus (Philips). The observed Laue diagrams were compared with the calculated ones by the "laueX" interactive program,[17] which allows one to simulate a Laue diagram from the knowledge of the orientation of the crystal, the cell parameters and the position of the detector. We used preliminary data of the atomic coordinates of $CaVO_3$ and $SrVO_3$.[18] The program also does the indexing of an experimental Laue diagram, evaluates the intensities of the Laue spots, and draws them as spots whose size is proportional to their intensity. After determining the geometry of the crystal axes, we cut the sample making use of a precision diamond saw.

2.2.2. Quantification of Stoichiometry

The oxygen off-stoichiometry in $Ca_{1-x}Sr_xVO_3$ was determined by using a Perkin-Elmer TGA-7 thermogravimetric (TG) analyzer from the weight gain on heating the sample to around 1300 K in flowing air and assuming that the final oxidation state of a vanadium ion is +5. Neither further weight gain due to peroxidation nor weight loss due to the desorption of the oxygen was observed, after the highest-oxidized material $(Ca_{1-x}Sr_x)_2V_2O_7$, which is an insulator with the pylochlore structure, was obtained.

As-prepared samples contain some amount of oxygen defects. The result of TG measurements indicated that, with increasing temperature, the samples are abruptly oxidized at around 420 K.[19] Moreover, after this oxidation, the oxygen concentration of the samples becomes stoichiometric and no further oxidation occurs until the temperature reaches around 700 K. Thereby, we can easily prepare samples without any oxygen off-stoichiometry by annealing the samples in air at $\sim 200\,^{\circ}$C for around 24 hours.

The stoichiometry of the ratio Ca : Sr : V = $1-x : x : 1$ was confirmed by the inductively coupled plasma atomic emission spectrometer (SEICO, SPS7000). The amount of off-stoichiometry in the single-crystalline samples were within the error bar, *i.e.*, less than 1%.

2.2.3. Transport Measurements

In order to perform the dc-electric resistivity measurement, the single crystalline samples were cut and shaped into a rectangular parallelepiped. A typical example of the dimension of the parallelepiped was $3 \times 1 \times 0.3\,\mathrm{mm}^3$. Electric resistivity measurements were done with a standard dc four-probe method. Four copper leads ($50\,\mu\mathrm{m}\phi$) were attached with silver paste (Du Pont 4922). Measuring current was typically ± 30 mA which was applied by a constant current source. The data were collected on both heating and cooling cycles.

In the magnetoresistance measurement, the sample was installed in a ^{3}He cryostat equipped with a superconducting magnet.

2.2.4. Magnetic Measurements

dc-susceptibility measurements were performed using a commercial rf-SQUID magnetometer (Quantum Design, MPMS). The measuring field was calibrated with a Pd standard. Details of this experiment for the $Ca_{1-x}Sr_xVO_3$ samples are described in Section 4.3.2.

2.2.5. Specific Heat Measurements

Specific heat data were obtained on both polycrystalline samples and single-crystalline samples between ~ 0.5 and ~ 20 K using a semiadiabatic heat-pulse method.[20] Details of this experiment for the $Ca_{1-x}Sr_xVO_3$ samples are described in Section 4.3.3.

2.3. High-Energy Spectroscopy: General Description

2.3.1. Energetics of Photoemission Spectroscopy

When an electron in a material is ejected via the photoelectric effect by an impinging photon with the energy of $\hbar\omega$, the energy conservation rule gives us

$$E_n + \hbar\omega = E_{n-1} + \varepsilon_k \,,$$

where E_n is the total energy of the initial n-electron system, E_{n-1} is the total energy of the final $(n-1)$-electron system, and ε_k is the

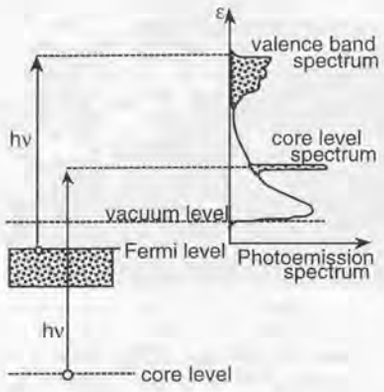

FIG. 2.2. Schematic diagram of photoemission spectroscopy.

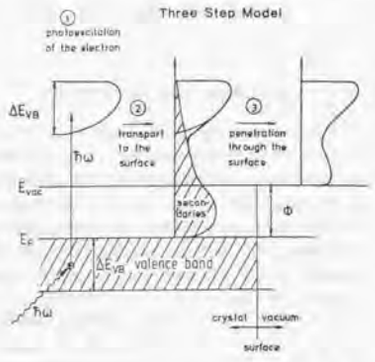

FIG. 2.3. PES as a three-step process: 1) photoexcitation of an electron; 2) travel to the surface with concomitant production of secondary electrons (shaded area); 3) penetration through the surface barrier and escape into the vacuum.

kinetic energy of the the emitted photoelectron measured from the Fermi level of the sample. According to the Koopman's theorem,[21] $(E_n - E_{n-1})$ can be related to the binding energy E_B of the single-particle energy level, from which the electron is ejected. As we count the number of the emitted electrons as a function of the kinetic energy ε_k or the binding energy E_B, an experimental spectrum is obtained as schematically shown in Fig.2.2. This measurement is called photoemission spectroscopy (PES). The obtained spectrum can be comparable to the one-electron energy distribution function in the solid.

To consider the photoemission process more appropriately, the so-called "three-step model" is extremely useful,[22] though it is a purely phenomenological approach. The basis for this model is shown in Fig.2.3. In this model, the complicated photoemission process is broken up into three steps: the excitation of the photoelectron, its passage through the solid to the surface and its penetration through the surface into the vacuum, where it is detected. During the second process, the transporting electron may be scattered and lose energy, becoming what is known as a secondary electron. To do the third step, the electron must overcome the surface work function, which in the simple picture, will simply cause the electron to lose a part of its energy, resulting in a rigid shift of the spectrum.

When the incident radiation used in a PES experiment is x-ray (for example, Mg Kα radiation with $\hbar\omega = 1253.6$ eV or Al Kα radiation with $\hbar\omega = 1486.6$ eV) the experiment is called x-ray photoemission spectroscopy (XPS). If the photon energy is ranged from several eV to a few hundreds eV, viz a vacuum ultraviolet region, the technique is called ultra-violet photoemission spectroscopy (UPS). One of the widely used light sources for UPS measurement is a helium discharge lamp with two discrete resonance lines (He I: 21.2 eV, He II: 40.8 eV). Another light source is synchrotron

radiation light emitted from charged particles moving with a velocity close to the velocity of light is also used as a complementary tool for UPS measurement as a tunable light source. The synchrotron radiation light covers the whole of the VUV region.

UPS is mainly used to study the valence band, while XPS is employed to study relatively high-binding energy core-levels as well as the valence band with less resolution.

A cross-section of photoelectron excitation is determined by optical transition probability, i.e., dipole transition probability. This probability depends on both the angular momentum and the energy of the atomic orbital of the electron in the initial bound state. Thereby, we can obtain information on the dominant angular momentum character for each feature in the PES spectrum by comparing the XPS and UPS spectra on the same binding-energy region.

2.3.2. Resonance Photoemission Spectroscopy

PES intensity of some valence band features shows a Fano-like intensity modulation as a function of photon energy near the absorption threshold of a core-level. This phenomenon is often referred as "resonance photoemission" (RPES), and has been extensively used to identify the chemical origin of valence band features.[23]

In Fig.2.4, a schematic drawing of the RPES is shown. The resonance is explained as a quantum interference between a direct excitation of a valence-band electron and autoionization (or direct recombination), giving a Fano-type resonance in the photoemission spectrum. The interaction responsible for the autoionization is the Coulomb interaction between the electrons, which is the same interaction as that attributed to Auger transitions. (It is noted that the Auger transition is a real process and dominates the core-hole lifetime of light elements.) Both the autoionization

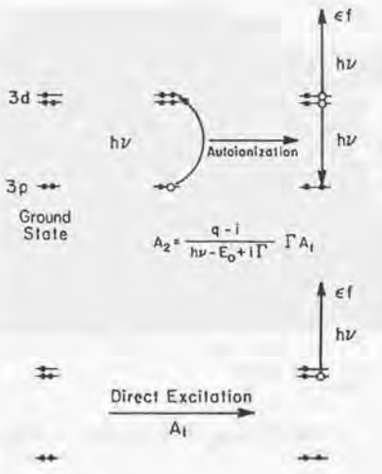

FIG. 2.4. Direct excitation of a valence-band electron (amplitude A1) interferes with an autoionization (A2) process to give a Fano resonance.

and the Auger transition yield an electron in continuum states above the Fermi level. It is evident from Fig.2.4 that we consider the second order perturbation. This means that we must add the amplitudes for the two processes and then square to obtain the probability. The two processes can interfere with one another, resulting in greatly decreased transition rates below threshold and enhanced ones above it.

RPES is a powerful tool for tracing the orbital origin of valence band features by comparing the threshold energy to appropriate core-level binding energies of the constituent atoms in the material under investigation. Moreover, for a strong resonance effect, the intermediate state is required to be fairly localized. This is the reason why RPES is often observed in the transition-metal oxides and the rare-earth compounds.

2.3.3. X-ray Absorption Spectroscopy

X-ray absorption spectroscopy (XAS) is one of the methods used to probe the unoccupied states. In an XAS measurement, electrons in the filled state (usually deep core-levels) are excited to the empty states in the solid by the impinging x-rays. The absorption strength of the x-rays can be measured by the following three typical methods: the transmission mode, the fluorescence-yield mode or the electron-yield mode.[24] If the absorption strength is plotted as a function of the photon energy, the spectrum can be comparable to the energy distribution function of the unoccupied states.

2.4. High-Energy Spectroscopy: Experimental

2.4.1. Photoemission Spectroscopy Experiment

PES should be performed under ultra-high vacuum (UHV) conditions, because the measurement is more sensitive to the surface rather than the bulk of the sample as is described in Sect.2.4.3. UHV is achieved with turbo-molecular pumps, ion pumps, and sublimation pumps.

A typical setup of the apparatus of PES experiments is depicted in Fig. 2.5, where the main chamber is connected to the electron energy analyzer, and to several pumps through the large pipes below the main chamber. The flanges on the main chamber are used for view-ports, light sources, electric feed-throughs, wobble-sticks, gauges, a manipulator on a XYZ stage, and so on. The whole system is held by the trestle table, which is also a framework of panels of a knockdown oven used for baking out the chamber.

In our laboratory setup, two light-sources (an ultra-violet light source and an x-ray source) and an electron energy analyzer (VG Microtech, CLAM-II) followed by an electron detector, are equipped on the UHV chamber, which is made of "Mu-metal". Mu-Metal is a nickel-iron alloy (77 % Ni, 15 % Fe, plus Cu and Mo) which has extremely high magnetic permeability at low field strengths, and the Mu-metal chamber can be used as a very effective magnetic screen with low residual magnetic field (typically $< 5\,\mathrm{mG}$).

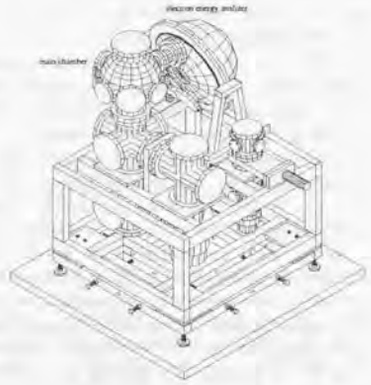

FIG. 2.5. Schematic picture of a typical setup of the apparatus of PES experiments. The electron energy analyzer, the main chamber, and large pipes below the main chamber for pumping units are depicted. There are several sizes of flanges on the main chamber used for view-ports, light sources, electric feed-throughs, wobble-sticks, gauges, and so on. A manipulator on a XYZ stage is usually mounted at the top of the main chamber. The whole system is supported by the trestle table, on which we construct a knockdown oven made of aluminum panels, for use when we bake out the chamber.

The energy analyzer is the spherical detection analyzer, which consists of two concentric hemispheres. In front of the energy-analyzer, a preretardation stage is equipped. This mode of operation is used to decrease (increase) the energy of electrons without changing their absolute energy spread. The decreased (increased) energy, *i.e.* the energy at which the electrons enter the analyzer is usually called the pass-energy and we set the pass-energy $5 - 10\,\mathrm{eV}$ for UPS and $50 - 100\,\mathrm{eV}$ for XPS depending on the experiments. The advantage of the preretardation is obvious; since the intrinsic resolution of the analyzer is proportional to the pass-energy, by retardation the effective resolution is enhanced.

We carried out PES experiments using a synchrotron light-source (BL-11D, BL-18A at the Photon Factory in the High Energy Accelerator Research Organization) and also a He discharge lamp and a Mg Kα x-ray source in the laboratory setup. In the experiment at BL-11D, we measured poly-crystalline $Ca_{1-x}Sr_xVO_3$ samples using the photon energy corresponding to the V $3p$ core-level threshold: 45 eV for off-resonance and 50 eV for on-resonance. RPES experiment of single-crystalline Sr_2RuO_4 samples was performed at BL-18A, with the photon energy ranging from 20 eV to 60 eV. Other UPS and XPS measurements were carried out using the commercial stand-alone spectrometer in the Electrotechnical Laboratory.

FIG. 2.6. Photograph of our PES apparatus. The electron energy analyzer (VG Microtech, CLAM-II), which is seen above the head of the author, are equipped on the "Mu-metal" UHV chamber. The Mg Kα x-ray source and the He discharge lamp are equipped below the CLAM-II analyzer.

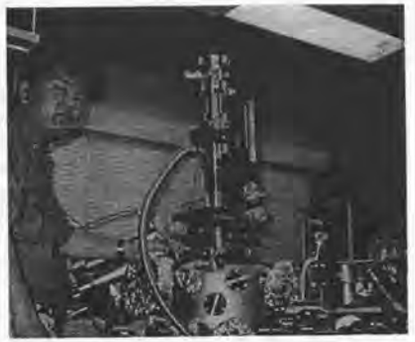

FIG. 2.7. On the top of the main chamber, the manipulator on the XYZ stage is equipped. The He-gas closed-cycle cryosystem (Daikin, CryoKelvin UV204SCLR) is incorporated to the manipulator with differentially pumped rotary feed-through.

2.4.2. X-ray Absorption Spectroscopy Experiments

XAS experiments were performed using synchrotron radiation at beamline BL-2B of the Photon Factory, High Energy Accelerator Research Organization. The experiment was carried out in the total electron-yield mode. Details of this experiment are described in Section 5.3.3.

2.4.3. Sample Surface Preparation

The mean free path of an electron in a solid whose kinetic energy is above the vacuum level is called a 'penetration depth' or 'escape depth.' The escape depth is strongly dependent on the kinetic energy of the electron, and follows what is known as the "universal curve"[25] The curve is shown in Fig.2.8. As seen from Fig.2.8, PES experiments have a

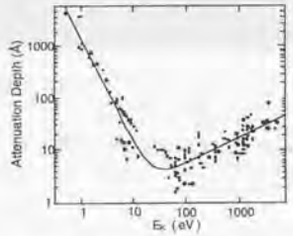

FIG. 2.8. The "universal curve" of electron escape depth versus kinetic energy.[25]

very high surface sensitivity of ~10 Å or less, when the kinetic energies of the electrons are in the range of 20 – 200 eV. This means that the surface preparation is a significant issue for the success of a PES experiment.

Especially, for the transition-metal oxides which we study in this work, special attention should be paid, because they contain oxygen atoms that are fairly loosely bound to the lattice and thereby easily escape from the surface. Therefore, it is obvious that many well-known surface-preparation procedures, for example, high-temperature annealing or ion-beam bombardment, are generally inappropriate, since they inevitably vary the surface composition by either outgassing oxygen from the surface region or preferentially sputtering the oxygen atoms so that the surface region becomes oxygen deficient.

Among the other surface preparation techniques that have been used, in-situ scraping and in-situ fracturing (cleaving) appear to be chemically the most non-destructive. In principle, both of these surface-preparation methods should be capable of exposing a clean surface. Especially, for angle-integrated photoemission measurements, in-situ scraping is most preferable. In some cases, experimental caveats may easily ruin this ideal notion of obtaining a clean surface by in-situ fracturing, because the sample is easy to cleave at grain boundaries, to which bulk contamination and impurities tend to accumulate as frequently observed in the oxides.

In addition, if we bake the samples in the vacuum chamber in order to get higher vacuum, this baking procedure depletes the samples of oxygen and changes their character. We have set a fast-entry load-lock system, so that our samples can be introduced into the chamber without baking. These precautions have increased the reliability of our experiments.

2.4.4. Decomposition of the surface and bulk spectrum

No matter how carefully we have prepared the surface of the sample, since the photoemission technique itself is extremely surface sensitive, we can probe typically the first few tens of angstroms within the surface. This is well known to the entire community of surface scientists who have used this very aspect to probe the surface of materials, which would be otherwise inaccessible. On the other hand, scientists, who are interested in the bulk properties, have also used this technique extensively with the tacit assumption that *the electronic structures at the surface and in the bulk are very similar*. This is in general a valid assumption in most materials, as has often been demonstrated by a good agreement between experimentally obtained photoemission spectra and calculated ones on the basis of the bulk electronic structures.[26,27]

However, in some materials, the surface electronic states are intrinsically different from those of bulk. In this case, the sufficiently careful surface preparation may rather reveal the difference of the two states.

Maiti, Priya, and Sarma have devised a novel way to separate out the surface and bulk contributions from the total photoemission spectrum;[28] this enhances the power of the photoemission technique such that one now obtains separate information about the surface and the bulk electronic structures. In order to separate the surface and the bulk contributions, we assume that the total spectrum $\rho(\omega)$ at any given photon energy can be given by the linear combination of the surface spectrum $\rho^s(\omega)$ and the bulk spectrum $\rho^b(\omega)$, *i.e.*,

$$\rho(\omega) = (1 - e^{-d/\lambda})\rho^s(\omega) + e^{-d/\lambda}\rho^b(\omega)\,; \quad (2.1)$$

where d is the thickness of the surface layer with the altered electronic structure compared to the bulk and λ is the mean free path of electrons as seen in Fig. 2.8. From Eq. 2.1, the intensity ratio of the surface and the bulk contributions in any spectrum becomes

$$\frac{1 - e^{-d/\lambda}}{e^{-d/\lambda}} = e^{d/\lambda} - 1\,.$$

The value of d/λ for deep core-level electrons with a kinetic energy of $E_c \sim 1000$ eV can be obtained by measuring the XPS spectrum and by performing the spectral decomposition by a line-shape analysis. Since λ is known to be proportional to the square root of the electron kinetic energy in the higher energy limit, as realized in XPS measurement,[29] we can estimate the corresponding d/λ for the valence band (VB) electrons (kinetic energy of $E_{\rm VB}$) by multiplying the d/λ obtained for the core-level electrons (kinetic energy of E_c) with $\sqrt{E_c/E_{\rm VB}}$. Thus, we obtain the value of $d/\lambda_{\rm XPS}$ for the valence band XPS spectrum. We also need to estimate the same quantity for the valence band spectrum excited with He I radiation $d/\lambda_{\rm He\,I}$. Unfortunately there is no universally accepted dependence of λ on kinetic energy in the lower energy limit, unlike the higher energy limit. In view of this, we assume, in this Thesis, the $\lambda_{\rm XPS}/\lambda_{\rm He\,I}$ value of $Ca_{1-x}Sr_xVO_3$ to be the same as in the closely related series $Ca_{1-x}La_xVO_3$, where it was experimentally estimated[28]

$$\lambda_{\rm XPS}/\lambda_{\rm He\,I} = 3.4\,. \quad (2.2)$$

Then, Eq. 2.1 becomes two simultaneous equations for each energy point ω,

$$\rho_{\rm XPS}(\omega) = (1 - e^{-d/\lambda_{\rm XPS}})\rho^s(\omega) + e^{-d/\lambda_{\rm XPS}}\rho^b(\omega)$$
$$\rho_{\rm He\,I}(\omega) = (1 - e^{-d/\lambda_{\rm He\,I}})\rho^s(\omega) + e^{-d/\lambda_{\rm He\,I}}\rho^b(\omega)\,.$$

Since we measure $\rho_{\rm XPS}(\omega)$ and $\rho_{\rm He\,I}(\omega)$ at every energy point ω, the above two equations can be solved exactly at every energy point ω for the two unknowns $\rho^s(\omega)$ and $\rho^b(\omega)$.

The final results for ρ^b and ρ^s are not very sensitive to the assumption of Eq. 2.2 as described in Chap. 5.

2.5. High-Energy Spectroscopy: Description by Many-Body Theory

2.5.1. One-Particle Spectrum

Here we describe the photoemission spectrum following the many-body theory formulation by Kotani,[30] and Gunnarson and Schönhammer.[31]

The retarded Green's function at 0 K is expressed as

$$G_s(\vec{r},\vec{r}',t-t') = \begin{cases} -i\langle 0|\{\varphi_s(\vec{r},t),\varphi_s^\dagger(\vec{r}',t')\}|0\rangle & \text{for } t \geq t' \\ 0 & \text{for } t \leq t'\,, \end{cases}$$

where s stands for a spin variable, $|0\rangle$ represents the ground state and $\{A, B\} \equiv AB + BC$. The Fourier transformation of the above equation gives,

$$\begin{aligned} & G_s(\vec{k}, t-t') \\ &= \frac{1}{V}\int d\vec{r}d\vec{r}' G_s(\vec{r},\vec{r}', t-t')\mathrm{e}^{-i\vec{k}\cdot(\vec{r}-\vec{r}')} \\ &= \begin{cases} -i\langle 0|\{a_{\vec{k},s}(t), a^\dagger_{\vec{k},s}(t')\}|0\rangle & \text{for } t \geq t' \\ 0 & \text{for } t \leq t' \,. \end{cases} \end{aligned} \tag{2.3}$$

Here we define $|n\rangle$ as an excited state of the system and E_n as the energy of the state. By the closure or completeness of the eigenfunction $\sum_n |n\rangle\langle n| = 1$, we obtain for $t \geq t'$

$$\begin{aligned} & G_s(\vec{k}, t-t') \\ &= -i\sum_n \langle 0|a_{\vec{k},s}(t)|n\rangle\langle n|a^\dagger_{\vec{k},s}(t')|0\rangle \\ &\quad - i\sum_n \langle 0|a^\dagger_{\vec{k},s}(t)|n\rangle\langle n|a_{\vec{k},s}(t')|0\rangle \\ &= -i\sum_{n(k\geq k_F)} \left|\langle n|a^\dagger_{\vec{k},s}|0\rangle\right|^2 \mathrm{e}^{-i\frac{(E_n-E_0)(t-t')}{\hbar}} \\ &\quad - i\sum_{n(k\leq k_F)} \left|\langle n|a_{\vec{k},s}|0\rangle\right|^2 \mathrm{e}^{-i\frac{(E_0-E_n)(t-t')}{\hbar}} \,. \end{aligned}$$

Transforming the above equation with respect to the single-particle energy ω, we have

$$\begin{aligned} G_s(\vec{k},\omega) &= -\frac{1}{\hbar}\int_0^\infty d\tau G_s(\vec{k},\tau)\mathrm{e}^{-i\frac{\omega\tau}{\hbar}} \\ &= -\frac{1}{\hbar}\sum_{n(k\geq k_F)} \left|\langle n|a^\dagger_{\vec{k},s}|0\rangle\right|^2 \int_0^\infty d\tau \mathrm{e}^{-i\frac{(\omega-E_n+E_0)\tau}{\hbar}} \\ &\quad -\frac{1}{\hbar}\sum_{n(k\leq k_F)} \left|\langle n|a_{\vec{k},s}|0\rangle\right|^2 \int_0^\infty d\tau \mathrm{e}^{-i\frac{(\omega+E_0-E_n)\tau}{\hbar}} \,. \end{aligned}$$

Then, the imaginary part becomes

$$\begin{aligned} & -\frac{1}{\pi}\mathrm{Im}G_s(\vec{k},\omega) \\ &= \sum_{n(k\geq k_F)} \left|\langle n|a^\dagger_{\vec{k},s}|0\rangle\right|^2 \delta(\omega - E_n + E_0) \\ &\quad + \sum_{n(k\leq k_F)} \left|\langle n|a_{\vec{k},s}|0\rangle\right|^2 \delta(\omega + E_0 - E_n) \,. \end{aligned}$$

The first term of the right-hand side of this equation corresponds to the angle-resolved (and spin-resolved) inverse-photoemission spectrum, while the second term corresponds to the angle(spin)-resolved photoemission spectrum. That is,

$$\begin{aligned} & -\frac{1}{\pi}\mathrm{Im}G_s(\vec{k},\omega) \\ &= A_s^{\omega\geq E_F}(\vec{k},\omega) + A_s^{\omega\leq E_F}(\vec{k},\omega) \end{aligned} \tag{2.4}$$

To put it more concrete, if we neglect here the interaction between electrons and assume $a_{\vec{k},s}(t) = \mathrm{e}^{-i\varepsilon^o_{\vec{k}}t/\hbar}a_{\vec{k},s}$, then, we obtain immediately from Eq.2.3,

$$G_s(\vec{k}, t-t') = -i\mathrm{e}^{-i\frac{\varepsilon^o_{\vec{k}}(t-t')}{\hbar}} \text{ for } t \geq t'$$

The simplest way to introduce an interaction, *i.e.* the finite life time of the quasi-particle due to scattering, is to modify the simplest Green's function above to the following expression:

$$G_s(\vec{k}, t-t') = -i\mathrm{e}^{-i\frac{(\varepsilon^o_{\vec{k}}-i\hbar\gamma)(t-t')}{\hbar}} \text{ for } t \geq t'$$

$$\begin{aligned} \rho(\omega) &\equiv \sum_s \left[\int_{k\leq k_F} d\vec{k}A_s^{\omega\geq E_F}(\vec{k},\omega) + \int_{k\geq k_F} d\vec{k}A_s^{\omega\leq E_F}(\vec{k},\omega)\right] \\ &= -\frac{2}{\pi}\int_{all} d\vec{k}\mathrm{Im}G(\vec{k},\omega) \end{aligned}$$

where the factor 2 is the result of the summation with respect to the spin coordinates. The integral over the whole k-space is replaced by the integral in energy-space with the single-particle density of state (DOS) $D(\omega)$ for the non-interacting electron $\varepsilon^o_{\vec{k}}$. Hence, we have

$$\rho(\omega) = -\frac{1}{\pi}\int_{-\infty}^{\infty} d\varepsilon^o_{\vec{k}} D(\varepsilon^o_{\vec{k}})\mathrm{Im}G(\vec{k},\omega) \tag{2.6}$$

If there is no interaction among electrons, the self-energy becomes zero. Then,

$$-\frac{1}{\pi}\mathrm{Im}G(\omega,\varepsilon^o_{\vec{k}}) = \delta(\omega - \varepsilon^o_{\vec{k}}) \,,$$

Fourier transformation of $G_s(\vec{k}, t-t')$ with respect to the single-particle energy ω becomes,

$$G_s(\vec{k},\omega) = \frac{1}{\omega - \varepsilon^o_{\vec{k}} + i\hbar\gamma}$$

Even in the case that the interaction is not such a naive one and γ is a complicated function of ω and k, the expression above is still valid. The single-particle Green's function is then written as

$$G_s(\vec{k},\omega) = \frac{1}{\omega - \varepsilon^o_{\vec{k}} - \Sigma_s(\omega,\vec{k})} \tag{2.5}$$

where $\Sigma_s(\omega,\vec{k})$ is called the "self-energy".

In this Thesis, we study spin-unpolarized and angle-integrated photoemission spectra, which are obtained according to Eq.2.4:

so that

$$\rho(\omega) = D(\omega) \,,$$

i.e. the spectral DOS becomes equal to the non-interacting DOS. In this study, for $D(\omega)$, we use DOS calculated by a band calculation within the local density approximation (LDA).

2.5.2. Phenomenological Self-Energy Correction and Effective Mass

By combining the low-energy Fermi liquid phenomenology and the high-energy approximation of the Green's function we can cal-

culate the quasiparticle spectrum of a many-body system. The high-energy behavior can be obtained to a desired accuracy by terminating the continued fraction expansion of a Green's function which is valid asymptotically at high energies:[32]

$$G(\vec{k},\omega) = \cfrac{1}{\omega - \varepsilon^{o}_{k} - \omega_1 - \cfrac{s_2^2}{\omega-\omega_3-\cfrac{s_4^2}{\omega-\cdots}}} \tag{2.7}$$

A priori, all the parameters ω_ℓ (ℓ odd) and s_ℓ (ℓ even) depend on the momentum k, which is chosen within a Brillouin zone.

In addition, all these parameters can be expressed in terms of the "moments" of the angle-resolved quasi-particle spectrum $A(\vec{k},\omega)$. To express ω_ℓ or s_ℓ, one needs to know all "moments" from order 0 up to ℓ. "Moments" are real quantities and appear as coefficients in the expansion of $G(\vec{k},\omega)$ in powers of $1/\omega$. Each moment obeys a sum-rule.[33]

According to the discussion with K. Matho, we have assumed that a consistent approximation is generated by truncating the expansion at some *"modified Padé-level"* Lthat is independent of k.[34]

Normally, in the conventional Padé approximation of order L, ω_ℓ and s_ℓ are replaced by 0 for $\ell > L$. But, by definition of the "modified Padé-approximation", we introduce phenomenological complex parameters, ω_L, s_{L+1}, and ω_{L+2}, to take into account the energy-independent damping of the background excitations (N.B., the first L moments are kept coincident with those of the conventional Padé approximation).

For $L = 3, 5, \cdots$:

- Energy parameters ω_ℓ and s_ℓ for $\ell < L$ are real and determined by sum-rules.
- The last three complex quantities (ω_L, s_{L+1}, and ω_{L+2}) are different from the usual Padé approximation, *i.e.*, their real parts are not related to moments ($\mathrm{Re}(\omega_L)$ is still equal to the corresponding term in the usual Padé approximation).
- The values of s_{L+1} and ω_{L+2} are imposed by general requirements of the self-energy near $\omega = 0$, and $\vec{k} = \vec{k_F}$. In this study, we constrain them according to the Fermi liquid conditions:
  (i) $\mathrm{Im}\Sigma(\omega = 0, \vec{k} = \vec{k_F}) = 0$;
  (ii) the singularity has real positive weight

  $$0 < Q < 1\,,$$

  where Q is a residue for the simple pole of the Green's function.

At the modified Padé-level L, the number of poles in the self-energy is equal to $(L+1)/2$. Obviously, $L = 1$ is the lowest non-trivial level of approximation, and the self-energy has only a single pole.

For example, at level $L = 3$, it is ω_1 and s_2 that are real, determining the center of gravity and the first and second moments of $A(\vec{k},\omega)$. Higher moments than the third do not exist at level $L = 3$.

At $L = 1$, things become somewhat mixed up between high and low energy behaviour: ω_1,s_2, and ω_3 are all complex. The angle-resolved quasi-particle spectrum behaves asymptotically like a Lorenzian with an effective width given by $\mathrm{Im}(\omega_1)$. The only high-energy sum-rules, which can be satisfied, concern the normalization (0th moment) and the position of the center of gravity (first moment). The latter is given by $\omega = \mathrm{Re}(\omega_1) + \varepsilon^{o}_{k}$.

In this study, we consider the following phenomenological self-energy function to model the photoemission line-shape and the effective mass: for $L = 3$

$$\Sigma(\vec{k},\omega) = \gamma\varepsilon^{o}_{k} + \frac{g\Gamma\Delta}{\omega - i(\Gamma+\Delta) - \frac{\Gamma\Delta}{\omega}} \tag{2.8}$$

and for $L = 1$,

$$\Sigma(\vec{k},\omega) = \frac{g\omega_1\omega - \gamma\varepsilon^{o}_{k}(\gamma\varepsilon^{o}_{k} - \omega_1)}{g\omega - (\gamma\varepsilon^{o}_{k} - \omega_1)}\,. \tag{2.9}$$

The effective mass of the quasi-particle at E_F is defined in this Thesis as

$$m^* = \left(\frac{1}{\hbar^2\vec{k}}\frac{d\varepsilon_k}{d\vec{k}}\bigg|_{\vec{k}=\vec{k}_F}\right)^{-1}, \tag{2.10}$$

where ε_k is the quasi-particle energy which is given as a solution $\omega = \varepsilon_k$ of the equation

$$\omega = \varepsilon^{o}_{k} + \mathrm{Re}\Sigma(\vec{k},\omega)\,. \tag{2.11}$$

ε^{o}_{k} corresponds to the energy of a free electron. However in this study we consider ε^{o}_{k} as an energy dispersion of a single-electron band obtained by band-calculation with LDA. Thereby, ε^{o}_{k} gives a "band mass":

$$m_b = \left(\frac{1}{\hbar^2\vec{k}}\frac{d\varepsilon^{o}_{k}}{d\vec{k}}\bigg|_{\vec{k}=\vec{k}_F}\right)^{-1}. \tag{2.12}$$

Using Eqs. 2.10, 2.11 and 2.12, we deduce that the effective mass is described by the following expression:

$$\begin{aligned}\frac{m^*}{m_b} &= \frac{\left|\frac{d\varepsilon^{o}_{k}}{d\vec{k}}\right|_{\vec{k}=\vec{k}_F}}{\left|\frac{d\varepsilon_k}{d\vec{k}}\right|_{\vec{k}=\vec{k}_F}} \\ &= \left(1 - \frac{\partial\mathrm{Re}\Sigma(\vec{k},\omega)}{\partial\omega}\bigg|_{\omega=E_F}\right) \\ &\quad\times \frac{\left|\frac{d\varepsilon^{o}_{k}}{d\vec{k}}\right|_{\vec{k}=\vec{k}_F}}{\left|\frac{d\varepsilon^{o}_{k}}{d\vec{k}}\right|_{\vec{k}=\vec{k}_F} + \left.\frac{\partial\mathrm{Re}\Sigma(\vec{k},\omega)}{\partial\omega}\right|_{\vec{k}=\vec{k}_F}} \\ &\equiv \frac{m_\omega}{m_b}\times\frac{m_k}{m_b}\,,\end{aligned} \tag{2.13}$$

where m_ω/m_b is called the "ω-mass" and m_k/m_b is called the "k-mass".[35]

Chapter 3

Anomalous Electronic Properties of $CaVO_{3-\delta}$ Due to Oxygen Off-stoichiometry

Part of this chapter has been published as Ref. 19 and Ref. 36.

3.1. Introduction

Some perovskite-type light-3*d* TM oxides, such as $LaTiO_3$[37,38] show metal-to-insulator transitions (MIT's) by delicately controlling the oxygen and La/Ti stoichiometries. In these materials, simple one-electron band theory is no longer enough to give a good account of the electronic states, so it is sure that the electron correlations play an important role to realize this MIT. However, another important point which requires careful consideration is that, in this kind of oxide with the formula ABO_3, oxygen and A/B stoichiometries are fairly unstable. The off-stoichiometry is not accidental but characteristic of these compounds. Even though we can obtain sufficiently stoichiometric compounds in some of the ABO_3 materials for experimental purposes, the off-stoichiometry is still present intrinsically and such inevitable defects are called "native-defects" to indicate that their properties are reproducible.[39] Here, we have investigated the effects of this unavoidable off-stoichiometry under the presence of electron correlations between conduction electrons.

It is intriguing to compare the two perovskite-type TM oxides $LaTiO_3$ and $CaVO_3$ which have nominally one 3*d* electron per unit formula, since oxygen off-stoichiometry seems to have a different effect on the two materials. Stoichiometric $LaTiO_{3+\delta}$ ($\delta \cong 0.00$) has been reported to be an insulator but becomes metallic by further oxidation ($\delta > 0$).[37,38] On the other hand, we have revealed that stoichiometric $CaVO_{3-\delta}$ ($\delta \cong 0.00$) shows better metallic conductivity than off-stoichiometric $CaVO_{3-\delta}$. In general, $CaVO_{3-\delta}$ has "oxygen-defects" and it is difficult to oxidize further ($\delta < 0$) around room temperature. Nevertheless, a very slight peroxidation ($\delta \cong -0.05$) renders the system insulating without inducing any significant structural changes.[19] The MI transition on $LaTiO_3$ is discussed as hole-doping into a Mott-Hubbard-type insulating matrix; within this picture, however, we cannot comprehend the MI transition in $CaVO_{3-\delta}$ ($\delta < 0$).

Moreover, it should be noted that drastic, unconventional changes of the magnetoresistance, magnetic susceptibility, and Hall effect have been observed in single-crystalline $CaVO_{3-\delta}$ ($\delta > 0$).[36,40]

In this chapter, we report electronic properties of $CaVO_{3-\delta}$ observed by delicately controlling the oxygen stoichiometry. As for the study on the "negative-magnetoresistance" seen in $CaVO_{3-\delta}$, the author contributed only in the earliest stage. The study has been suc-

ceeded by other members in our group, and the recent results of the detail experiments have been discussed in their review article.[40]

3.2. Experiments

Poly-crystalline $CaVO_{3-\delta}$ was prepared by solid state reaction, and a single crystal was grown by floating-zone method as described in Chap. 2; both were examined to be single phase by powder x-ray diffraction measurements. According to the XRD measurements by Shirakawa et al., the orthorhombic $CaVO_3$ becomes monoclinic $CaVO_{3-\delta}$ upon reduction (Fig. 3.1 and Table 3.I).

TABLE 3.I. Lattice parameters of $CaVO_{2.8}$ and $CaVO_{3.0}$ at room temperature.

	a(Å)	b(Å)	c(Å)	γ(°)	b/a
$CaVO_{2.8}$	5.3825	7.4991	5.3887	90.227	1.393
$CaVO_{3.0}$	5.3130	7.5397	5.3329	90 (orthorhombic)	1.419

This can be attributed to the expansion of the VO_6 octahedra as a result of the electron doping.

Thermogravimetric analyses were performed for both the powdered poly-crystalline and single-crystalline samples of ~30 mg in flowing air using a commercial apparatus (Perkin-Elmer, TGA-7). If we use bulk samples, especially the bulk single-crystals, it takes for too much long to reach the final oxidation state in our TG measurement facility. Oxygen stoichiometry was actually determined from the weight gain on heating the sample to around 1300 K and assuming that the final oxidation state of vanadium was +5.

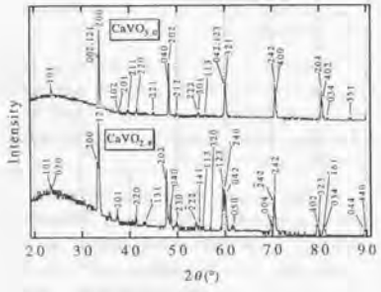

FIG. 3.1. X-ray powder diffraction patterns of $CaVO_{2.8}$ and $CaVO_{3.0}$ at room temperature.[40]

For the electrical resistivity measurements, the poly-crystalline samples were cut into rectangular parallelepiped shapes. The dimensions of the samples were $3 \times 1 \times 0.3\,mm^3$. The measurement were done while oxidizing the samples in air. We used the standard four-probe method, however, four-electrodes were made by evaporating gold instead of silver paste, and attaching gold wires onto the evaporated strips with gold paste (Tokuriki Honten, #8563). The measurement was done from room temperature up to 1000 K, and the temperature was changed as slowly as 0.5 K/min in order to coincide with the diffusion ratio of oxygen into the bulk sample.

In the magnetoresistance measurement, the sample was installed in a ^{3}He cryostat equipped with a superconducting magnet. The measurement was performed at 4.2 K. The sample was placed in an external field up to 12.5 Tesla perpendicular to the (100) plane, and electric current was along the c-axis.

dc-susceptibility measurements were performed using a commercial rf-SQUID magnetometer (Quantum Design, MPMS-II).

3.3. Results and Discussion

Figure 3.2 shows a result of the TG measurement and its derivative (DTG) for poly-crystalline $CaVO_y$ (top), and that of the electric resistivity measurement with several heating and cooling processes starting at various temperatures (bottom). With increasing temperature, the sample is abruptly oxidized at $T^* = 415$ K for the polycrystal as seen in Fig. 3.2, and at ~432 K for the single crystal. After this oxidation, y becomes almost equal to 3.0 in both samples. The electrical resistivity plunges around T^*, because the contribution to the resistivity of the additional scattering due to the oxygen off-stoichiometry is considered to be more significant in this material than the effect of increasing the number of carriers by electron doping.

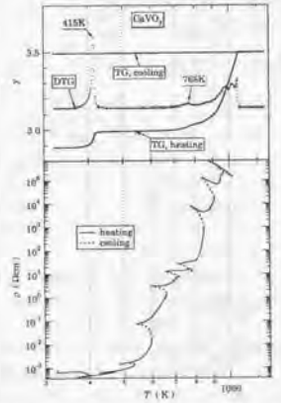

FIG. 3.2. The result of TG analysis and electrical resistivity obtained by heating the poly-crystalline $CaVO_{3-\delta}$ sample in air. Note that these measurements were not performed simultaneously. The vertical axis of the upper panel represents the oxygen content of $CaVO_y$. $y = 3.0$ corresponds to stoichiometric $CaVO_3$ and $y = 3.5$ corresponds to the final oxidation state $Ca_2V_2O_7$. The lower panel shows the temperature dependence of the electrical resistivity with several heating and cooling cycles starting at various temperatures.

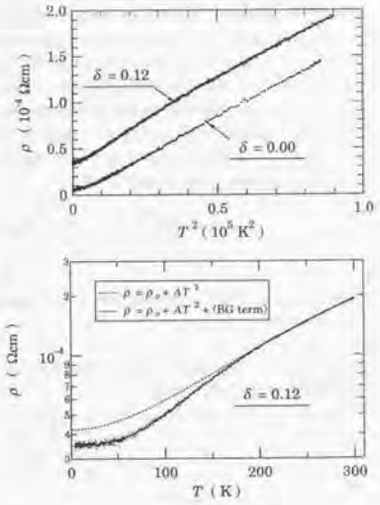

FIG. 3.3. Temperature (T) dependence of electrical resistivity (ρ) in $CaVO_{3-\delta}$ for $\delta = 0.00$and0.12. Top: ρ is plotted against T^2. Bottom: results of fitting to ρ of $\delta = 0.12$. The broken line represents $\rho = \rho_o + AT^2$, and solid line represents $\rho = \rho_o + AT^2$ with a Bloch-Grüneisen term due to the electron-phonon scattering.

The temperature dependence of ρ below room temperature also depends on the oxygen stoichiometry as seen in Fig. 3.3. No hysteresis between cooling and heating process was observed in this case. Both samples show fairly small residual resistivity ρ_o compared with the other TM oxides in the literature. The temperature dependence seems to be characterized by the relation $\rho = \rho_o + AT^2$,

which is believed to originate from electron-electron scattering, as seen in the upper panel of Fig. 3.3. However, we cannot fit the data in the whole temperature range with a unique value of the coefficient A as demonstrated in the lower panel of Fig. 3.3; we have to add the Bloch-Grüneisen term due to the electron-phonon scattering for a better fit:

$$\rho = \rho_o + AT^2 + \frac{4\kappa T^5}{\Theta^6}\int_0^{\Theta/T}\frac{e^z z^5 dz}{(e^z-1)^2} \tag{3.1}$$

The obtained fitting parameters are displayed in Table 3.II. Even though we find out that the electron-phonon scattering is not negligible, the contribution of the electron-electron scattering, assuming the AT^2 term comes only from this source, still dominates at least up to room temperature. By introducing the oxygen defects $\delta = 0.12$, the coefficient A increases a little. Detailed discussion on the origin of the T^2 term, and the relation between the value of A and the effective mass m^*/m_b are given in Chap. 4.

TABLE 3.II. Parameters in the formula 3.1 obtained by the least-squares fit to the electric resistivities of $CaVO_{2.88}$ and $CaVO_{3.00}$.

	$\rho_o(\Omega\mathrm{cm})$	$A(\Omega\mathrm{cmK}^{-2})$	$\kappa(\Omega\mathrm{cmK})$	$\Theta(\mathrm{K})$
$CaVO_{2.88}$	3.49×10^{-5}	8.99×10^{-10}	0.307	885
$CaVO_{3.00}$	5.59×10^{-6}	7.67×10^{-10}	0.126	628

It is also interesting to note that the stoichiometric samples are further oxidized to $y \cong 3.05$ at very high temperatures $T_{MI} \cong 770\,\mathrm{K}$. In other words, the stoichiometric sample is extremely stable to further oxidation. This is obvious, because the perovskite-type ABO_3 structure has no room in which extra oxygen can intervene. In the case of $CaVO_3$, this slight oxidation has a significant effect on the transport properties: the derivative of the resistivity becomes negative above T_{MI}.

Then, the question arises; what is the insulating state? In $LaTiO_y$, the metallic sample ($y > 3$) remains orthorhombic and single phase up to $y = 3.2$ [$(y > 3)$ means the deficiency of both the La and Ti sites.] Then, the sample becomes insulating at $y \cong 3.3$ due to the inter-growth of an insulating $La_5Ti_5O_{17}$ phase.[37] On the other hand, metallic $CaVO_3$ becomes insulating by very slight oxidation. Electron microscopy indicates the existence of 5-fold and 3-fold superstructures,[41] though we have not yet detected any traces of inter-growth of other phases in insulating $CaVO_{3.05}$ by the XRD measurements. Superstructures might modify the Brillouin zone and possibly open a gap at the Fermi level; however, this needs further investigation.

The dc-magnetic susceptibility χ (defined as magnetization M divided by applied field H) at 0.1 T is shown in Fig. 3.4. The stoichiometric sample shows temperature independent paramagnetic behavior, while the off-stoichiometric sample shows strong temperature dependence, though no sign of a magnetic transition was seen between 5 and 300 K. The difference in the magnetic susceptibilities of the two samples obeys the Curie-Weiss law:

$$\chi(T) = \frac{C}{T-\Theta}.$$

The deduced Curie constant C is $0.11\,\mathrm{emu\,K\,mol^{-1}} \equiv 0.11\,\mathrm{erg\,K\,Oe^{-2}\,mol^{-1}}$. Here, we assume the local moment originates

from the localized V^{3+} ions. Since the Curie constant is expressed as

$$C = \frac{N\mu_{eff}^2}{3k_B},$$

where $N\,\mathrm{mol^{-1}}$ is the number of local moments per one mole, $\mu_{eff} = g_J\sqrt{J(J+1)}\mu_B$, $\mu_B = 9.274\times10^{-21}\,\mathrm{erg\,Oe^{-1}}$, and $k_B = 1.3807\times10^{-16}\,\mathrm{erg\,K^{-1}}$, we can easily deduce $N = 0.11N_A\,\mathrm{mol^{-1}}$ by assuming that $J = S = 1$ for a V^{3+} ion and $g_J = g \cong 2$, where $N_A = 6.022\times10^{23}\,\mathrm{mol^{-1}}$. This means that $\sim$11% of the V ions are considered to be the localized V^{3+} ions. On the other hand, the oxygen off-stoichiometry $\delta = 0.12$ corresponds to a doping level of 0.24 electrons per one V site. The nominal valency of the V ion is 3.76+, and $V^{4+} : V^{3+} = 0.76 : 0.24$. Therefore, at least $0.11/0.24 = 45.8\,\%$ of the V^{3+} ions should be localized; i.e. V^{4+}(itinerant) : V^{3+} (itinerant) : V^{3+} (localized) $= 0.76 : 0.13 : 0.11$, where "itinerant" means that the electron is neither localized nor contributes to the local magnetic moment. The number of "itinerant" carriers per V site is $1\times0.76+2\times0.13 = 1.02$; accordingly, we find that in this $CaVO_{3-\delta}$ system the doped electrons, introduced by the oxygen off-stoichiometry, do not change the number of conduction electrons, but introduce instead some V^{3+} ions with a local magnetic moment.

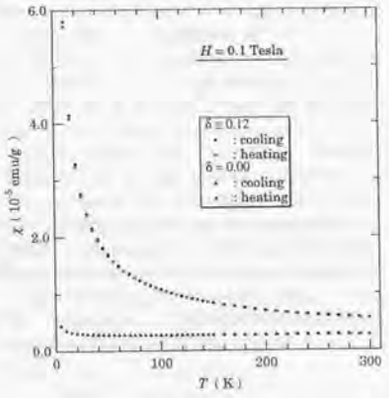

FIG. 3.4. Temperature dependence of magnetic susceptibility χ of $CaVO_{3-\delta}$ ($\delta = 0.00$ and 0.12) at 0.1 T.

Shirakawa *et al.*[40] have studied this issue in further detail and deduced that, by fitting the magnetization data by a Brillouin function, either 4 % of the V ions have $S = 3/2$ or 6 % of the V ions have $S = 1$. (The former one gives a better fit to their data.) Moreover, they have found that a V ion, deprived of at least two nearest-neighbor oxygen ions, produces a local magnetic moment; this is well explained by the lack of a conduction path through the V-O-V network.

The magnetoresistance

$$\frac{\rho(H)-\rho(0)}{\rho(0)}$$

changes drastically when oxygen off-stoichiometry is introduced. As shown in Fig. 3.5, the stoichiometric sample shows a positive magnetoresistance which depends quadratically on the applied magnetic field (H^2), while the off-stoichiometric sample shows negative magnetoresistance which is rather a quartic function of the applied magnetic field. The negative magnetoresistance was observed below $\sim$ 20 K and becomes weaker as the temperature is raised. It is surprising that such a small amount of oxygen off-stoichiometry induces a complete change in the magnetoresistance behaviors; furthermore, both the positive and negative magnetoresistance do not saturate up to 12.5 T. The full-potential linear-augmented-plane-wave (FLAPW) energy-band calculation within LDA indicates that $CaVO_3$ has three Fermi surfaces, two of which are almost spherical but the third one has an open orbit along the (110) direction.[42] The existence of

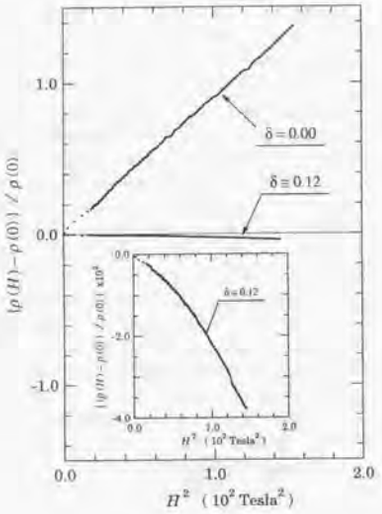

FIG. 3.5. Magnetoresistance of $CaVO_{3-\delta}$ (δ = 0.00 and 0.12) at 4.2 K plotted against the square of the applied magnetic field H. Inset shows the blow-up (100 times larger) of the negative magnetoresistance.

the open orbit may account for the absence of saturation of the positive magnetoresistance; nevertheless, this is not applicable in the case of negative magnetoresistance.

In general, the magnetoresistance is expressed as a sum of a positive term and a negative contribution due to, *e.g.*, a skew scattering by magnetic impurities; thereby, whenever a negative magnetoresistance is present at low magnetic fields, it is soon obscured by the relatively large positive magnetoresistance, as observed in the dilute-Kondo system,[43] in spin disorder scattering,[44] and in others.[45]

As Shirakawa *et al.* pointed out in Ref. 40, the negative magnetoresistance does not depend on the angle between the measuring current and the applied magnetic field. This indicates that no positive contribution to the magnetoresistance exists, since the positive (normal) magnetoresistance is generally anisotropic.

The complete disappearance of the positive term has been also confirmed;[40] it is well reproduced by consistently using the same Brillouin function which fits well to both the Hall coefficient and the magnetic moment, *i.e.*, the whole contribution to the negative term is due to the V^{3+} local moments, which is the same as that of the extraordinary Hall effect and the Curie-Weiss term.

Then, we are confronted by two difficulties. The first is the question of why the positive term never contributes to the magnetoresistance. The second is that, if all these effects are caused by the dilute magnetic impurities, it is expected that the Kondo effect is observed. At present, we do not have any explanation for these issues. However these problems have lead us to recognize that the $CaVO_3$ matrix is not a conventional metal, and to consider that a comprehension of the nature of the electron correlation in this system gives us a cue to clarify the unusual properties originating in the oxygen off-stoichiometry. Thus, we left the matter open for the further investigation and in the following chapters, we try to understand the effect of the electron correlation in $CaVO_3$ and other related materials.

Chapter 4

Evolution of the Electronic Properties of $Ca_{1-x}Sr_xVO_3$: Systematic Bandwidth Control

Part of this chapter has been published as Ref. 46 and Ref. 47.

4.1. Introduction

Despite extensive investigations on 3*d* transition-metal (TM) oxides,[16] there remain many more mysteries still to unravel. The metal-to-insulator transitions (MIT's) in 3*d* TM oxides with a partially filled 3*d* band, for example, have given us great incentive to re-examine several previous studies of the electronic states in these TM oxides.

The most important feature of this kind of 3*d* TM oxides is that simple one-electron band theory is no longer sufficient to give a good account of the electronic states, since the electron correlations are much larger than expected for the one-electron bandwidth.[5] Mott first introduced the concept of MIT caused by a strong Coulomb repulsion of electrons.[1] Although the description of the MIT (Mott transition) is still debated from various points of view,[48] a more challenging problem lies in the metallic phase near the Mott transition, where the system is known to show *anomalous* metallic properties, and substantial enhancement of the fluctuations of spin, charge and orbital correlations is observed. This problem has been investigated with renewed vigor since the discovery of high-T_c cuprate superconductors and although a number of enlightening works have been done so far, still we cannot grasp a comprehensive view of the physics.

In this chapter, we focus on one of the open questions namely the problem of the effective mass in the perovskite-type $3d^1$ correlated metal $Ca_{1-x}Sr_xVO_3$. An important manifestation of the mass enhancement in the perovskite-type light-3*d* TM oxides has been given by Tokura *et al*[49] as shown in Fig. 4.1. They reported filling-dependent electronic properties in the $Sr_{1-x}La_xTiO_3$ system near the MI transition around $x = 1$. The $LaTiO_3$ ($x = 1$) material behaves as an insulator below 300 K and antiferromagnetic ordering of Ti $S = 1/2$ spins occurs at $T_N = 120 \sim 150$ K.[37] They also reported that Fermi-liquid-like behavior was observed even in the immediate vicinity of the MI phase boundary, with a critical increase of m^*/m_b arising from the effect of the enhanced electron correlations. Within the framework of Fermi-liquid theory, the only way to approach MIT continuously is to realize the divergence of the single-quasi-particle mass m^*/m_b at the MIT point.[10] The critical behaviors observed in the $Sr_{1-x}La_xTiO_3$ system are fairly systematic, thus provoking intense theoretical study; however there is still room for arguments, es-

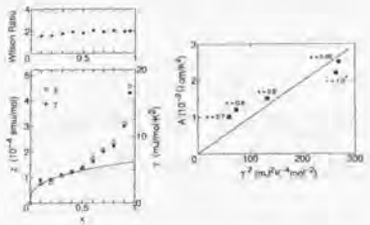

FIG. 4.1. Electronic properties of $Sr_{1-x}La_xTiO_3$ reported by Tokura et al.[49] **Left**: The filling dependence of the electronic specific heat coefficient (γ, closed circles), Pauli paramagnetic susceptibility at 300 K (χ, open circles), and the Wilson ratio χ/γ normalized to $3\mu_B^2/\pi^2 k_B$. **Right**: T^2 coefficient of resistivity A vs. γ^2 near the MI boundary.

pecially in the following points

1. Tokura *et al.* compared the effective mass m^*/m_b to the free electron mass m_0. However, the x dependence of the "band mass" m_b should also be taken into account. Compared with the value of m_b for the similar system $CaVO_3$, the mass enhancement of the $Sr_{1-x}La_xTiO_3$ system is not so large, except for the region $x > \sim 0.8$. (N. B., the x in Fig. 4.2 (left) represents the Sr content.)

2. The critical increase of the value of m^*/m_b in the $Sr_{1-x}La_xTiO_3$ system is only seen in the region very close to the MI transition boundary[50] [Fig.4.2 (left)]. However, in this region, it is not obvious whether Fermi-liquid theory is still valid. In fact, in the region of significant mass enhancement ($x > 0.92$), the number of carriers seems to be depleted[50] ($\delta < 0.08$ in the right panel of Fig.4.2). This is thought to be due to the antiferromagnetic fluctuation, so we ought to discuss the behavior of m^*/m_b only in the paramagnetic region $0.08 < \delta (= 1 - x) < 0.2$.

3. Another filling-dependent MI transition is observed in the $Y_{1-x}Ca_xTiO_3$ system.[51,52] However, the MIT occurs around $x = 0.4$ which is relatively far from integral filling. Nevertheless, the effective mass shows a conspicuous enhancement in the vicinity of MIT similar to that seen in the $Sr_{1-x}La_xTiO_3$ system (Fig.4.2). Thus, it seems reasonable to suppose that this kind of mass enhancement, observed in those "filling-control" systems close to MIT, might be induced by fluctuations or inhomogeneity of the insulating phase near the boundary of MIT.

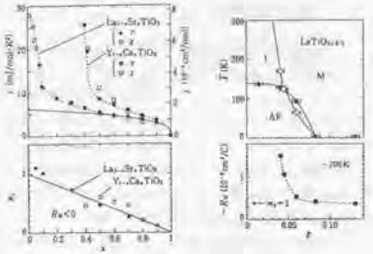

FIG. 4.2. Recent data of electronic properties of $La_{1-x}Sr_xTiO_3$ and $Y_{1-x}Ca_xTiO_3$ reported by T. Katsufuji and Y. Tokura.[50] **Left**: The filling dependence of the electronic specific heat coefficient γ, Pauli paramagnetic susceptibility at 300 K χ, and the number of carriers n_c deduced from the Hall coefficient at 300 K. **Right**: Phase diagram of the filling control system $LaTiO_{3+\delta/2}$, and the Hall coefficient.

The above problems can be due to the fact that the critical behaviors depend on the path along which a system approaches the boundary of MIT. In the $Sr_{1-x}La_xTiO_3$ system, the band filling is dominantly controlled instead of the bandwidth.

The question then arises: how does the effective mass in the metallic state actually change as we change solely the electron correlation strength without changing the band filling? In order to elucidate this issue, another type of systematic experiment is required; *i.e.*, we need to control only the $3d$ bandwidth W in a particular system while keeping the band filling fixed.

Representative examples are the pressure-induced MIT reported in V_2O_3,[8] where hydrostatic pressure modifies W. However, for a quantitative discussion, we need to know the change of the lattice constants under pressure. Moreover, in general, the anisotropic compressibility due to the anisotropy of the lattice structure affects W in a complex manner. Other examples are found in nickel-based compounds: the perovskite-type $RNiO_3$ with R of the trivalent rare-earth ions (La to Lu),[53] and the pyrite-type chalcogenide system $NiS_{2-x}Se_x$.[54] The insulating state of these nickel compounds is classified as a charge-transfer insulator rather than a Mott-Hubbard insulator in the so-called Zaanen-Sawatzky-Allen classification scheme of TM compounds.[55,56] Therefore, MIT occurs as a closing of the charge-transfer gap with an increase of the p-d hybridization. Thus, it is inevitable that MIT is not described by the simple model of the Mott transition and the metallic state is more complicated.

Based on these considerations, we have synthesized a solid solution of the perovskite-type metallic vanadates, $CaVO_3$ and $SrVO_3$, in order to investigate the metallic state near the Mott transition more simply with a systematic bandwidth control. We have succeeded in obtaining single crystals of the homogeneous metallic alloy system $Ca_{1-x}Sr_xVO_3$ with nominally one $3d$ electron per vanadium ion. In the $Ca_{1-x}Sr_xVO_3$ system, as we isovalently substitute a Ca^{2+} ion for a Sr^{2+} ion, a lattice distortion occurs. This is governed by the so-called tolerance factor f of the perovskite-type compounds ABO_3 defined as

$$f = \frac{R_A + R_O}{\sqrt{2}\,(R_B + R_O)},$$

where R_A, R_O, and R_B are the ionic radii of the A ion, the O ion (oxygen), and the B ion, respectively. When the value of f is almost 1, the system is cubic; while for $f < 1$, the lattice structure changes to rhombohedral and then to the orthorhombic $GdFeO_3$ type. In the $GdFeO_3$ structure, it is known that the B-O-B bond angle decreases continuously with decreasing f almost irrespective of the set of A and B.[14] According to the literature,[57] the ionic radii of Ca^{2+}, Sr^{2+}, V^{4+}, and O^{2-} ions are 1.34, 1.44, 0.58, and 1.40 Å, respectively. Thus we obtain a value of f of 1.014 for $SrVO_3$, and 0.979 for $CaVO_3$, corresponding to a V-O-V bond angle of $\sim 180°$ for $SrVO_3$ and $\sim 160°$ for $CaVO_3$. The buckling of the V-O-V bond angle reduces the one-electron $3d$-bandwidth W, since the effective $3d$-electron transfer interaction between the neighboring V sites is governed by the supertransfer process via the O $2p$ state.

Accordingly, the ratio of the electron-electron Coulomb repulsion energy U normalized to W (U is considered to be kept almost constant by the substitution) can be systematically controlled in $Ca_{1-x}Sr_xVO_3$ without varying the nominal carrier concentration. The V-O-V bond angle of $CaVO_3$ ($\sim 160°$) is almost equal to insulating $LaTiO_3$, so that, in a naive sense, $CaVO_3$ is not far from MIT boundary, although we should consider the difference of Ti^{3+} and V^{4+}.

From this point of view, $Ca_{1-x}Sr_xVO_3$ is an ideal system to investigate the variation of the metallic state near the Mott transition.[58] In fact, as we discussed in Chapter 3, $CaVO_3$ shows several interesting properties due to a small amount of oxygen defects, which is considered to be related to the strong electron correlation in this system. Furthermore, as we show in Chapter 5 in detail and also in the Ap-

pendix, the $Ca_{1-x}Sr_xVO_3$ system shows some spectroscopic manifestation of the strong electron correlation (we have reported a part of this study already,[59-61] and similar work has been reported by others[62]), showing that there is significant spectral weight redistribution in the $Ca_{1-x}Sr_xVO_3$ system. Therefore, the effective mass of this system, especially at the $x = 0$ end ($CaVO_3$), is expected to be enhanced as discussed for $Sr_{1-x}La_xTiO_3$ near the insulating composition $LaTiO_3$.

Nevertheless, the $Ca_{1-x}Sr_xVO_3$ system does *not* show such a significant enhancement of the effective mass as we shall show below. The goal of this paper is to reveal intriguing behavior in the evolution of the effective mass, as we control the U/W ratio in this system. Details of the experiments, especially the method of preparing single crystals of this new vanadate system, are described in Sec. 4.2. We discuss the cubic-orthorhombic lattice distortion in Sec. 4.3.1. The results from magnetic susceptibility measurements and the obtained effective mass m^*/m_b are shown in Sec. 4.3.2, and compared to m^*/m_b deduced from the electronic specific heat coefficient in Sec. 4.3.3. The Sommerfeld-Wilson ratio is found to be almost equal to 2, which is strong evidence of the large electron correlation. The electrical resistivity data are analyzed by a model incorporating the electron-electron interaction (T^2 term) as well as the electron-phonon interaction (Bloch-Grüneisen term) in Sec. 4.3.4. It is noted that the Kadowaki-Woods ratio lies in the same region as the heavy Fermion compounds. Finally, we discuss the effect of nonlocal electron correlations, *i.e.*, the momentum-dependent self-energy, which can be significant near the Mott transition, in order to explain consistently both the strong electron correlations seem in the spectroscopic data and the missing enhancement of the effective mass.

4.2. Experiment

We prepared poly-crystalline $Ca_{1-x}Sr_xVO_3$ by solid state reaction, and single crystals were grown by the floating-zone method according to the prescription described in Chap. 2. Here we show the rod obtained after the FZ method (Fig. 4.3 and Fig. 4.4).

FIG. 4.3. Sample rod of $Ca_{0.3}Sr_{0.7}VO_3$.

The most important point here is to control the reduction atmosphere delicately, depending on the amount of the Sr content x, and also on the oxygen stoichiometry of the feed rod. As we increase the value of x, it is necessary to add <0.1 % hydrogen to the flowing argon.

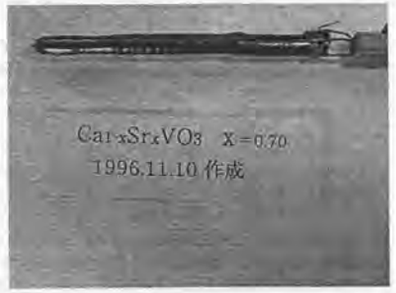

FIG. 4.4. Sample rod of $Ca_{0.3}Sr_{0.7}VO_3$ prepared by the FZ method. Except for the both ends, almost all the parts of the rod consist of several single crystals with the typical grain size is $7 \times 7 \times 10\,mm^3$.

As soon as this small amount of hydrogen is added, however, the melting temperature rises drastically, and the molten zone shrinks unless we increase the lamp power once more. On the other hand, if the amount of hydrogen gas is not sufficient, the liquid phase in the molten zone loses viscosity and spills by degrees along the rod. Furthermore, a different phase, which might be a peroxidized phase, appears in the molten zone and precipitates on the surface of the zone to form an "antler." Thus, a delicate feedback control of the amount of hydrogen gas and the power of the halogen lamp is necessary to obtain a single crystal with sufficient quality. Typical dimensions of a single-crystalline grain in the resultant rods are $\sim 2 \times 1 \times 1\,mm^3$.

Each crystal was examined by powder XRD and by Laue photography to check for homogeneity. Results are summarized in the next section.

The oxygen off-stoichiometry in $Ca_{1-x}Sr_xVO_3$ was determined using a Perkin-Elmer TGA-7 thermogravimetric (TG) analyzer from the weight gain on heating the sample to around 1300 K in flowing air and assuming that the final oxidation state of a vanadium ion was +5. Neither weight gain due to peroxidation, nor weight loss due to desorption of the oxygen was observed, once the highest-oxidized material $(Ca_{1-x}Sr_x)_2V_2O_7$, which is an insulator with the pylochlore structure, was obtained.

As-prepared samples contain a certain amount of oxygen defects. The result of the TG measurements indicated that, with increasing temperature, the samples are abruptly oxidized at around 420 K.[19] Moreover, after this oxidation, the oxygen concentration of the samples becomes stoichiometric and no further oxidation occurs until the temperature reaches around 700 K. Therefore, we were able to prepare samples without any oxygen off-stoichiometry by annealing the samples in air at $\sim$200°C for around 24 h.

The stoichiometry of the ratio Ca : Sr : V = $1 - x : x : 1$ was confirmed by an inductively coupled plasma atomic emission spectrometer (SEICO, SPS7000). The amount of off-stoichiometry in the single-crystalline samples was below the detectability limit, *i.e.*, less than 1%.

In order to perform the dc-electrical resistivity measurement, the single crystalline samples were cut and shaped into rectangular parallelepipeds without particular attention to the alignment of the crystal axes. A typical example of the dimension of the parallelepiped was $2 \times 0.5 \times 0.3\,mm^3$. We also prepared samples with two different alignments: for one set of samples, the longest-edge, along which the measuring current flows, is parallel to the [100] axis of the pseudocubic perovskite, and for the other set, the current flows along the [110] axis. Some of these samples showed clear dependence on the alignment. However, this was not due to any features in the electronic structure as discussed in the following section. All the electrical resistivity measurements were done with a standard dc four-probe method. Four copper leads (50 μm diameter) were attached with silver paste (Du Pont 4922). The measuring current was typically ± 15 mA supplied by a constant current source. Since the $x = 1$ sample was much smaller than the other ones, we measured its resistivity using the Van der Pauw technique in which one places the contacts on the corners and rotates the current and voltage configuration. The data were collected on both heating and cooling cycles.

dc-susceptibility measurements were performed using a commercial rf-SQUID magnetometer (Quantum Design, MPMS-II) without particular attention to the alignment of the crystal axes. The measuring field was calibrated up to 5 T with a Pd standard.

Specific heat data were obtained both on poly-crystalline and single-crystalline samples between $\sim$0.5 and $\sim$20 K using a semiadia-

batic heat-pulse method.[20]

4.3. Results and discussion

4.3.1. Lattice constants

The XRD patterns of $Ca_{1-x}Sr_xVO_3$ for varying Sr content are displayed in Fig. 4.5 and the deduced lattice parameters are shown in Table 4.I and Fig. 4.6. The lattice parameters change systematically from the orthorhombic $CaVO_3$ to $SrVO_3$ which is simple cubic within the error bar ($\sim \pm 0.2\,\%$). According to the four-axes XRD measurement,[18] the lattice constants of $CaVO_3$ are $a = 0.53185(8)$ nm, $b = 0.7543(2)$ nm, and $c = 0.53433(8)$ nm.

TABLE 4.I. Lattice parameters of single-crystalline $Ca_{1-x}Sr_xVO_3$ at room temperature.

x	a (Å)	b (Å)	c (Å)
0.00	5.3411	7.5280	5.3281
0.20	5.3539	7.5766	5.3467
0.25	5.3608	7.5874	5.3606
0.30	5.3736	7.5993	5.3731
0.40	5.3774	7.6099	5.3778
0.50	5.3993	7.6314	5.3920
0.70	5.4140	7.6578	5.4094
0.75	5.4162	7.6604	5.4158
0.80	5.4238	7.6687	5.4190
1.00	5.4358	7.6869	5.4285

The V-O-V bond angle is 154.(3)° for V ions on the ac plane [V-O bond length is 0.1891(6) nm] and 171.(0)° for V ions along the b axis [V-O bond lengths are 0.190(0) nm and 0.196(5) nm].[18] This large buckling of the V-O-V bond angle ($\sim 160°$ in average) is considered to make the one-electron $3d$ bandwidth W of this system smaller than that of $SrVO_3$, where the V-O-V bond angle is almost exactly 180°.

Using the atomic coordinates data, we can simulate the Laue pattern with the "laueX" interactive program,[17] given that the space group of $SrVO_3$ could be orthorhombic P_{nma} but with the unique lattice parameter ($a/\sqrt{2} = b/2 = c/\sqrt{2} = 3.842$Å) (Fig. 4.7). The direction of the x-ray is parallel to the cubic ⟨111⟩-axis of the sample, and the cubic ⟨111⟩-axis is perpendicular to the screen.

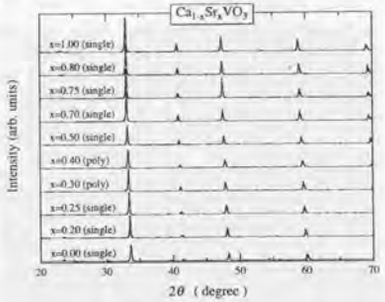

FIG. 4.5. X-ray powder diffraction patterns of single-crystalline $Ca_{1-x}Sr_xVO_3$ at room temperature. $x = 0.3$ and $x = 0.4$ samples are polycrystals.

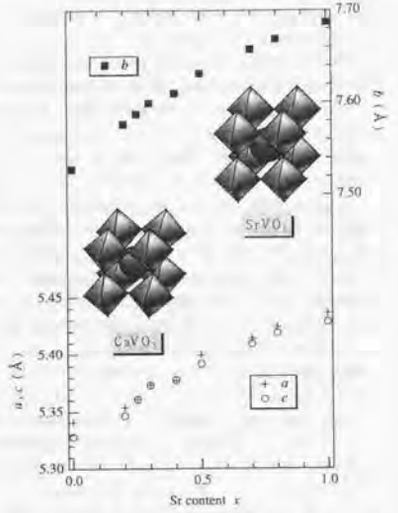

FIG. 4.6. The lattice parameters a, b, and c of $Ca_{1-x}Sr_xVO_3$ at room temperature, estimated from the XRD patterns. The data are plotted against Sr content x. Note that each deduced lattice parameter contains approximately $\pm 0.2\,\%$ error. Thus it is not appropriate to discuss the exact crystal symmetry based only on this plot.

The index and intensity of each Laue spot in Fig. 4.7 have been evaluated by the program; each index denotes the name of the reciprocal lattice point for the orthorhombic notation, and the spot-size is proportional to their intensity. The calculated result is compared to the observed Laue photographs (Fig. 4.8). In Fig. 4.8, the direction of the x-ray is parallel to the cubic ⟨111⟩-axis, and perpendicular to the screen. All the spots are well simulated by the calculation. We determined the crystal axes geometry by this method. (See Chap. 2 for details.)

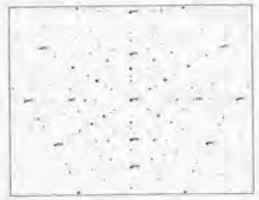

FIG. 4.7. Calculated Laue diagrams of $SrVO_3$ by the "laueX" interactive program.[17] See text for details.

FIG. 4.8. Laue photographs of the single-crystalline $SrVO_3$ at room temperature. See text for details.

4.3.2. Magnetization

Figure 4.9 shows the temperature dependence of the magnetic susceptibilities χ of $Ca_{1-x}Sr_xVO_3$ at $5\,\mathrm{T} \equiv 50000$ Oe. Since none of the samples showed any significant hysteresis between the heating and cooling cycles, we have plotted data for the heating process only.

The field dependence of the magnetization M of $SrVO_3$ is plotted in Fig. 4.10. We measured M up to 5 T while increasing and decreasing the applied field H at both 5 K and 300 K. At 300 K, the magnetization curve shows no hysteresis and M depends linearly on H. This means that only paramagnetic moments contribute to the total magnetization. When we decrease the temperature to 5 K, the

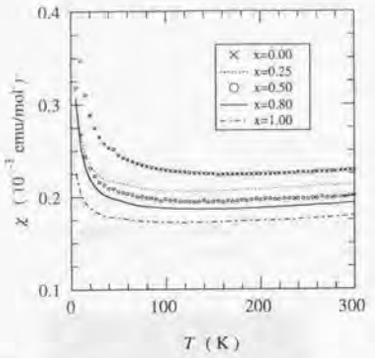

FIG. 4.9. Magnetic susceptibilities χ of single-crystalline $Ca_{1-x}Sr_xVO_3$ for $x = 0.00, 0.25, 0.50, 0.80$, and 1.00 measured at 5 T≡50000 Oe plotted against temperature T. Samples were cooled to 4 K with no applied field and then warmed up to 300 K in 5 T. No significant hysteresis was observed during the heating and cooling cycles.

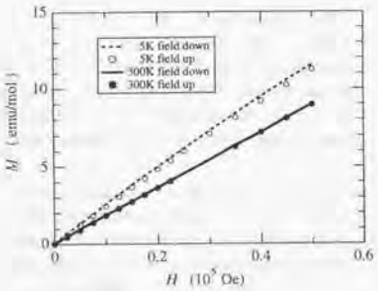

FIG. 4.10. Magnetization M of $SrVO_3$ plotted against the applied field H. The data were collected while increasing and decreasing the applied field between 0 and 5 T at both 5 K and 300 K.

magnetization curves become hysteretic and also show a slight upturn.

Here we note that in perovskite-type oxides with the formula ABO_3, oxygen and A/B stoichiometries are fairly unstable. The off-stoichiometry is not rare but characteristic of these compounds. Even though one tries to obtain sufficiently stoichiometric compounds in ABO_3 materials for the purposes of the experiment, the off-stoichiometry is still present intrinsically and such inevitable defects are called "native defects" to indicate that their properties are reproducible.[39] We have so far reported the effects of the (unavoidable) oxygen off-stoichiometry in $CaVO_3$ by intentionally introducing the oxygen defects in varying degrees.[19,36,40] In this study, although we tried to prepare oxygen-stoichiometric samples using a delicate annealing procedure, there still exists a very small but irreducible amount of inevitable oxygen defects.

Local moments due to these oxygen defects contribute to M as a spontaneous magnetization or in this case a sublattice magnetization, because the Weiss temperature is negative. The value of M is very small compared with that observed in $CaVO_{2.8}$ (Ref. 40) and is consistent with the number of local moments deduced from the Curie constants (*vide infra*).

All the magnetic susceptibility data χ are well reproduced by the following formula:

$$\chi = \chi_{\rm P} + \chi_{\rm dia} + \chi_{\rm core} + \chi_{\rm orb} + \frac{C}{T-\vartheta} + \alpha T^2 , \quad (4.1)$$

where $\chi_{\rm P}$ is the Pauli paramagnetic term, $\chi_{\rm dia}$ is the Landau diamagnetism, $\chi_{\rm core}$ comes from the diamagnetic contribution of the core levels, and $\chi_{\rm orb}$ is due to the orbital Van Vleck paramagnetism. The Curie-Weiss term is attributed to impurities such as the native oxygen defects. The last term is considered to originate from the higher-order temperature-dependent term in the Pauli paramagnetism, that is neglected in the zeroth-order approxi-

mation, and reflects the shape of the density of states (DOS) at the Fermi energy $E_{\rm F}$.

Here we define our terminology of the effective mass, which we call the "thermal effective mass" and is defined as

$$\frac{m^*}{m_{\rm b}} \equiv \frac{\gamma}{\gamma^{\rm LDA}} = \frac{D(E_{\rm F})}{D^{\rm LDA}(E_{\rm F})} , \quad (4.2)$$

where $D^{\rm LDA}(E_{\rm F})$ is the density of states at the Fermi energy obtained by the local-density approximation (LDA) band calculation,[42,63] and $D(E_{\rm F})$ is the corresponding experimental value. (We thus employ $m_{\rm b}$ deduced from the LDA band calculation, rather than $m_{\rm b}$ of the noninteracting Bloch electrons.) We shall discuss this definition in more detail below (see Eq. 4.6).

Using the above definition, the first two terms of Eq. 4.1 are rewritten:

$$\begin{aligned} \chi_{\rm spin} &= \chi_{\rm P} + \chi_{\rm dia} \\ &= \left(\frac{m^*}{m_{\rm b}} - \frac{m_{\rm b}}{3m^*} \right) \chi_{\rm P}^{\rm LDA} , \end{aligned} \quad (4.3)$$

where $\chi_{\rm P}^{\rm LDA}$ stands for the Pauli paramagnetic term deduced from the LDA band calculation:

$$\begin{aligned} \chi_{\rm P}^{\rm LDA} \ [{\rm emu/mol} \equiv {\rm erg\,Oe^{-2}\,mol^{-1}}] &= N\mu_B^2 D^{\rm LDA}(E_{\rm F}) \\ &= 2.376 \times 10^{-6} \times D^{\rm LDA}(E_{\rm F}) , \end{aligned}$$

where N mol^{-1} is the number of itinerant electrons per mole of unit formula, $\mu_B = 9.274 \times 10^{-21}$ erg Oe^{-1}, and $D^{\rm LDA}(E_{\rm F})$ in in the unit of states/Ry/f.u. (Note that the expression for the Landau diamagnetism term is exact only for a free-electron band. The real diamagnetism term is actually proportional to $(m^*/m_{\rm b})^{-2}$ independent of the shape of the Fermi surface; however, the deviation from this expression is not very significant for this system.)

For the third term $\chi_{\rm core}$, we have used the values given in the literature,[64] as summarized in Table 4.II.

TABLE 4.II. Core diamagnetism of the constituent ions in $Ca_{1-x}Sr_xVO_3$ (Ref. 64).

ion	$\chi_{\rm dia}$ emu/mol
Ca^{2+}	-13.3×10^{-6}
Sr^{2+}	-28.0×10^{-6}
V^{5+}	-7.7×10^{-6}
O^{2-}	-12.6×10^{-6}

The fourth term is

$$\begin{aligned} \chi_{\rm orb} &= -\sum_{\vec{k},n} \left. \frac{\partial^2 \varepsilon_n(\vec{k})}{\partial H^2} \right|_{H=0} \theta(E_{\rm F} - \varepsilon_n(\vec{k})) \\ &= 2\mu_B^2 \sum_{n,n'} \sum_{\mu} \int \frac{d\vec{k}}{(2\pi)^3} \frac{\left| \langle n\vec{k} | l_{\mu z} | n'\vec{k} \rangle \right|^2}{\varepsilon_{n'}(\vec{k}) - \varepsilon_n(\vec{k})} \times (f(\varepsilon_n) - f(\varepsilon_{n'})) , \end{aligned}$$

where $l_{\mu z}$ is the z-component of the orbital angular moment $\vec{l}_\mu$ ($\mu = 1, \cdots, 5$) for the d-orbital, and $f(x)$ is the Fermi-Dirac distribution function. This term corresponds to the

Van Vleck paramagnetism in insulating materials, and becomes large when the "quenching" of the orbital angular moment is not sufficient. Moreover, it has been suggested that this term can also be enhanced by the electron correlation, since electron correlations change the electron configuration as well as the crystal field, and the Van Vleck term cannot be treated by a one-body approximation.[65] This is still a difficult question; for this system, we used an x-independent value [66] of $\chi_{\rm orb} = 6.5 \times 10^{-5}$ emu/mol estimated in another $3d^1$ metallic vanadate system VO_2.[67] Hence, we can fit Eq. 4.1 to the observed data.

The obtained values of the Curie-Weiss term C are as small as 0.5–2.2×10^{-3} emu K/mol, and the Weiss temperatures $\theta = -6.0$–1.6 K, indicating very weak antiferromagnetic interaction among the local moments. These small values of the Curie-Weiss term are considered to be due to the V^{3+} ($S = 1$) local impurity moment that arises from the "native oxygen defects." From the value of $C = 2.2186 \times 10^{-3}$ emu K/mol for $CaVO_3$, we can evaluate that only 0.22 % of the V sites have the $S = 1$ local moment; this amount of local impurities is inevitable in ABO_3 materials, but irrelevant for our discussion of the metallic properties, such as the value of the effective mass. The obtained values of the coefficient α of the last term in Eq. 4.1 are also very small (0.5–2.5×10^{-10} emu $K^{-2}mol^{-1}$), implying that the deviation from a temperature-independent Pauli paramagnetism is negligible in the temperature range we measured. Only when we need to estimate the value of m^*/m_b from χ_P much more accurately will it be necessary to perform the measurement up to higher temperatures.

The obtained ratio of the effective mass m^*/m_b to the LDA band mass m_b, is summarized in Table 4.III and also displayed in Fig. 4.11.

TABLE 4.III. The effective mass deduced from the fit to the magnetic susceptibility data with Eq. 4.1 and Eq. 4.3, where $\chi_{\rm core}$ and $\chi_{\rm orb}$ are fixed to the values in the literature (Refs. 64 and 67). $\chi_P^{\rm LDA}$ are calculated from $D(E_F)$ obtained by the LDA band calculation (Refs. 42 and 63).

x	$\chi_{\rm spin}$ (emu/mol)	$\chi_P^{\rm LDA}$ (emu/mol)	m^*/m_b
0.00	2.008×10^{-4}	6.651×10^{-5}	3.126
0.20	1.905×10^{-4}	6.454×10^{-5}	3.060
0.25	1.904×10^{-4}	6.405×10^{-5}	3.081
0.50	1.788×10^{-4}	6.159×10^{-5}	3.013
0.70	1.678×10^{-4}	5.963×10^{-5}	2.928
0.80	1.678×10^{-4}	5.865×10^{-5}	2.973
1.00	1.606×10^{-4}	5.668×10^{-5}	2.946

The value of m^*/m_b is approximately 3 though increases gradually and systematically as we decrease the Sr content x.

As already described, the large buckling of the V-O-V bond angle in going from $SrVO_3$ to $CaVO_3$ (in $CaVO_3$ $\angle$V-O-V $\sim 160°$, which is almost equal to the insulating $3d^1$ system $LaTiO_3$) can lead this system closer to the boundary of the MI transition. Actually, a significant spectral weight redistribution, which is a manifestation of a strong electron correlation, has been observed already in this system.[59–61] Nevertheless, no significant amount of mass enhancement can be deduced from this magnetic measurement. This surprising result motivates us to reconsider whether this system may indeed be a correlated metallic system. However, as well as the spectral weight redistribution which we show in Chap. 5, the measurement of the electronic specific heat and electrical resistivity described below give us further evidence for strong correlations in this system.

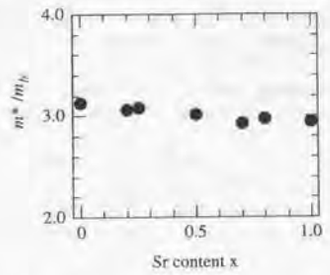

FIG. 4.11. Effective mass m^*/m_b compared with the LDA band mass m_b plotted against Sr content x. m^*/m_b increases systematically in going from $SrVO_3$ to $CaVO_3$. The values are not as large as expected.

4.3.3. Electronic specific-heat coefficient

An alternative method to evaluate m^*/m_b is to measure the electronic contribution to the specific heat, γT, which reflects DOS at E_F. γ is called the electronic specific-heat coefficient. Using $D^{\rm LDA}(E_F)$ states/Ry/f.u. obtained by the LDA band calculation,[63] we can deduce the value of the electronic specific-heat coefficient in the noninteracting limit $\gamma^{\rm LDA}$:

$$\gamma^{\rm LDA} = \frac{\pi^2}{3} k_B^2 N D^{\rm LDA}(E_F) ,$$

where N is the number of itinerant electrons per mole in the unit formula. Then,

$$\gamma^{\rm LDA}\ [\text{mJ mol}^{-1}\ \text{K}^{-2}] = 0.173238 \times D^{\rm LDA}(E_F) .$$

The ratio of the effective mass to the band mass (m^*/m_b) is deduced from the ratio of the observed γ to the calculated $\gamma^{\rm LDA}$.

Sufficiently below the Debye temperature Θ, the constant volume specific heat C_v/T can be plotted against T^2, *i.e.*,

$$C_v/T = \gamma + \beta T^2 \qquad (4.4)$$

in order to separate out the contribution of the ionic degrees of freedom (βT^3) dominant at high temperatures. The coefficient β is related to Θ as follows:

$$\beta = \frac{9Nk_B}{\Theta^3} \int_0^{\Theta/T} \frac{e^z z^4 dz}{(e^z-1)^2} \simeq \frac{12\pi^4 Nk_B}{5\Theta^3} \ (T \ll \Theta) .$$

Here we note that experiments measure the specific heat at constant pressure, C_p, but we normally compare this result to C_v, since these two are almost identical in a solid. This is understood most naively by the thermodynamical identity:

$$\frac{C_p}{C_v} = \frac{\left(\frac{\partial P}{\partial V}\right)_S}{\left(\frac{\partial P}{\partial V}\right)_T} ,$$

i.e., the difference of these two specific heats is that between the work necessary to compress a system which is thermally isolated (adiabatic) and the work that is necessary to compress a system which is in contact with a heat bath (isothermal). As for the lattice contribution, since the internal energy of a lattice is almost dominated by its equilibrium value, such thermal considerations are of little consequence in determining the compressibility. For the electronic contribution, one can deduce from the above expression $C_p/C_v = 1 + O(k_BT/E_F)^2$ for the metallic free electron gas; thereby, at low temperatures where the electronic contribution to the specific heat becomes dominant, the two specific heats differ by a negligible amount.

The measured constant pressure specific heats C_p of $Ca_{1-x}Sr_xVO_3$ below ~ 10 K are shown in Fig. 4.12. In the temperature range displayed in Fig. 4.12, the data do not behave simply as Eq. 4.4. Therefore, we have tried to fit the observed specific heat $C_p \simeq C_v$ by the formula:[47]

$$C_v = \gamma T + \beta T^3 + k_B \sum_{i=1,2} \frac{N_i\, {x_i}^2\, e^{x_i}}{(1+e^{x_i})^2}\,, \tag{4.5}$$

($x_i \equiv \Delta E_i/(k_B T)$) where the last term corresponds to the Schottky contributions of N_i ($i = 1, 2$) "impurities" per mole with the excitation energies ΔE_i. As shown in Fig. 4.12 (right), we can fit the data sufficiently by Eq. 4.5. The two bumps around 3 K and 1 K can be attributed to the two Schottky terms, except for the upturn below $\sim$1 K. The excitation energies ΔE_i are $\sim$0.2 and $\sim$0.8 meV, which are almost independent of samples and Sr contents x.

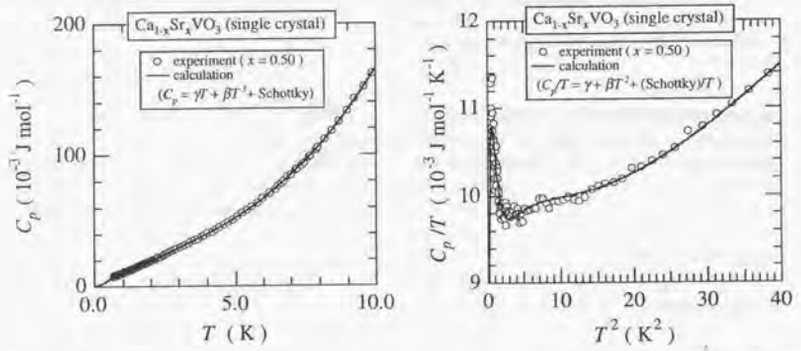

FIG. 4.12. **Left**: $C_p \simeq C_v$ of $Ca_{1-x}Sr_xVO_3$ ($x = 0.5$) plotted against T. **Right**: C_p/T plotted against T^2. In both figures, open circles stands for measured data and solid lines are the result of fitting using Eq. 4.5.

Typical amounts of the Schottky impurities per V ion are $N_1 \sim 0.1$ and $N_2 \sim 0.2$ %; these values are comparable to that of local moments estimated by the Curie-Weiss term (see Sec. 4.3.2). The obtained Debye temperatures Θ's vary according to the Sr content as shown in Fig. 4.13 (right). The values of Θ are comparable to $\Theta \sim 300$ K deduced from the temperature of the phonon-drag peak of the Seebeck coefficient of $CaVO_3$,[68] substantiating the result of our least-square fit to the specific heat data.

All results of the least-squares fits are summarized in Table 4.IV. We find that the value of γ, even in $CaVO_3$ ($x = 0$), is still not so enhanced as we discuss below ($m^*/m_b \simeq 1.5$), though these values are comparable to the $La_{1-x}Sr_xTiO_3$ system in the La rich phase, except for $x < 0.08$. (The γ values in the $Ca_{1-x}Sr_xVO_3$ system are much larger than that of the less correlated sodium metal $\sim$ 1 mJ mol^{-1}K^{-2}.)

TABLE 4.IV. Fitted parameters for the specific heat and deduced effective mass m^*/m_b of $Ca_{1-x}Sr_xVO_3$. γ^{LDA} has been calculated from $D(E_F)$ obtained by the LDA band calculation (Refs. 42 and 63). m^*/m_b is defined as the ratio between γ and γ^{LDA}.

x	Θ (K)	γ (mJ mol^{-1}K^{-2})	γ^{LDA} (mJ mol^{-1}K^{-2})	m^*/m_b
0.00	335.6	7.304	4.849	1.506
0.20	326.3	6.558	4.706	1.394
0.40	316.8	6.761	4.563	1.482
0.50	276.3	7.169	4.491	1.596
0.75	282.2	7.027	4.312	1.626
0.80	280.3	6.593	4.276	1.542
1.00	300.0	6.409	4.133	1.551

x	N_1 (%)	ΔE_1 (meV)	N_2 (%)	ΔE_2 (meV)
0.00	0.239	0.371	0.229	1.243
0.20	0.081	0.175	0.129	0.696
0.40	0.046	0.157	0.066	0.651
0.50	0.084	0.209	0.145	0.774
0.75	0.096	0.209	0.168	0.801
0.80	0.106	0.213	0.174	0.898
1.00	0.131	0.241	0.259	0.861

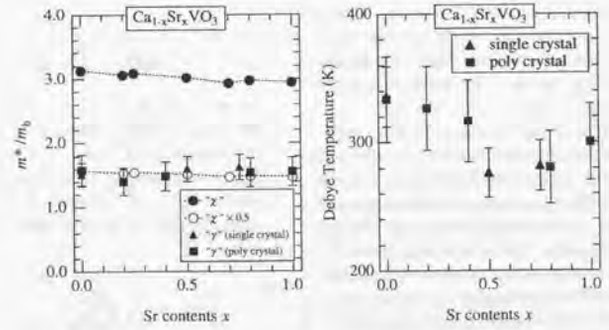

FIG. 4.13. **Left**: m^*/m_b obtained by comparing the observed γ with the calculated one (filled squares, denoted by "γ"). "χ" stands for m^*/m_b deduced from χ_{spin} (filled circles, denoted by "χ") and the half values of "χ" (open circles) also plotted for comparison. **Right**: Debye temperatures plotted against x.

The effective masses compared to the band masses m^*/m_b are defined as the ratios of the observed γ to the γ^{LDA}. We plot the values of m^*/m_b against x with those deduced from the magnetic susceptibilities for comparison (Fig. 4.13). From Fig. 4.13, we can also es-

timate the Sommerfeld-Wilson ratio R_W:[69]

$$R_W \equiv \frac{\gamma^{LDA}}{\chi_P^{LDA}} \frac{\chi_P}{\gamma} = \frac{\left(\frac{m^*}{m_b}\right)_\chi}{\left(\frac{m^*}{m_b}\right)_\gamma}$$

It is worthwhile emphasizing that R_W is of order unity, implying that the electronic specific-heat coefficient γ is similarly enhanced to the Pauli paramagnetic susceptibility χ_P. Furthermore, this means it is appropriate to assume a one-to-one correspondence between the quasi-particle excitations of this system and those of a free-electron gas.

For a noninteracting Bloch-electron system, $R_W = 1$. One of the possible reasons for $R_W \neq 1$ is a ferromagnetic fluctuation, which enters in χ_P as $\chi_P/\chi_P^0 = (m^*/m_o)S$, where $S = (1 + F_o^a)^{-1}$ is called the Stoner enhancement factor including the zeroth asymmetric Landau parameter F_o^a. (For an isotropic free-electron system, R_W becomes unity, because $F_o^a = 0$.) In exchange-enhanced metals, *i.e.*, a system with ferromagnetic fluctuations, S plays an important role and R_W becomes fairly large. However, this is not the case for the $Ca_{1-x}Sr_xVO_3$ system, since we have not observed any traces of ferromagnetic fluctuations.

The value of R_W for $Ca_{1-x}Sr_xVO_3$ deduced from our experiments is 1.7–2, as illustrated in Fig. 4.13, where the half-values of m^*/m_b deduced from the magnetic measurements are plotted for comparison. In strongly correlated electron systems, it has been argued that the value of R_W becomes equal to 2 at $U/W = \infty$.[69,70] Although there is a small deviation, $R_W \approx 2$ clearly indicates the importance of electron correlations in this system.

The deviation from $R_W = 2$ can be ascribed to the contribution of the electron-phonon interaction. It is known that this interaction contributes a factor $(1 + \lambda)$ to γ, but not to χ_P. Hence, R_W is modified to become $R_W(1 + \lambda)^{-1}$. From Fig. 4.13, we can approximately estimate $\lambda <\sim 0.3$, so that the electron-phonon interaction in this system is fairly small. Furthermore, it should be noted that, for the higher orbital degeneracies, R_W decreases towards unity in the limit of large orbital degeneracy.[71] Since the degeneracies of the t_{2g} orbitals of the vanadium $3d$ electrons are not completely released in this $Ca_{1-x}Sr_xVO_3$ system, R_W is not necessarily equal to 2. However, there are experimental error bars for the estimation of γ values, and the above argument needs to be investigated further.

Thus, we can conclude that $R_W \sim 2$ implies that electron correlations are strong in this system. Then, the question arises: why is the enhancement of the effective mass so moderate, despite the presence of such large electron correlations?

Before considering this question, it is worth while mentioning the definition of our terminology of the effective mass. The effective mass here is the so-called "thermal effective mass" defined as

$$\frac{m^*}{m_b} \equiv \frac{\gamma}{\gamma^{LDA}} = \frac{D(E_F)}{D^{LDA}(E_F)} , \tag{4.6}$$

where $D^{LDA}(E_F)$ is the density of states at the Fermi energy obtained by the LDA band calculation, and $D(E_F)$ is the value deduced from the thermodynamic and magnetic experiments. This is different from the effective mass (tensor) of the DC electrical conductivity:

$$\frac{1}{m^*}\delta_{ij} = \frac{1}{\hbar^2}\frac{\partial^2 \varepsilon_k}{\partial k_i \partial k_j}\bigg|_{\vec{k}=\vec{k}_F} ,$$

where ε_k is the quasiparticle energy. Eq. 4.6 leads to the relation

$$\frac{m^*}{m_b} = \left| \frac{\frac{d\varepsilon_k^{LDA}}{d\vec{k}}\Big|_{\vec{k}=\vec{k}_F}}{\frac{d\varepsilon_k}{d\vec{k}}\Big|_{\vec{k}=\vec{k}_F}} \right| , \tag{4.7}$$

because of the definition of the density of states:

$$\left|\frac{d\varepsilon_k}{d\vec{k}}\Big|_{\vec{k}=\vec{k}_F}\right| \equiv D(E_F)^{-1} ,$$

and

$$\left|\frac{d\varepsilon_k^{LDA}}{d\vec{k}}\Big|_{\vec{k}=\vec{k}_F}\right| \equiv D^{LDA}(E_F)^{-1} .$$

The quasiparticle energy ε_k is given as a solution $\omega = \varepsilon_k$ of the equation

$$\omega = \varepsilon_k^{LDA} + \mathrm{Re}\Sigma(\vec{k},\omega) , \tag{4.8}$$

where $\Sigma(\vec{k},\omega)$ is the self-energy of the system in which all of the interaction effects are contained. ε_k^{LDA} corresponds to the energy dispersion of a single-electron band obtained by the LDA band calculation. In this study, we use ε_k^{LDA} instead of ε_k^0 which is the energy of a noninteracting Bloch electron. Using Eqs. 4.7 and 4.8, we deduce that the effective mass is given by the following expression:

$$\begin{aligned} \frac{m^*}{m_b} &= \left(1 - \frac{\partial \mathrm{Re}\Sigma(\vec{k},\omega)}{\partial\omega}\Big|_{\omega=E_F}\right) \\ &\times \left| \frac{\frac{d\varepsilon_k^{LDA}}{d\vec{k}}\Big|_{\vec{k}=\vec{k}_F}}{\frac{d\varepsilon_k^{LDA}}{d\vec{k}}\Big|_{\vec{k}=\vec{k}_F} + \frac{\partial \mathrm{Re}\Sigma(\vec{k},\omega)}{\partial\vec{k}}\Big|_{\vec{k}=\vec{k}_F}} \right| \\ &\equiv \frac{m_\omega}{m_b} \times \frac{m_k}{m_b} . \end{aligned} \tag{4.9}$$

This is the general expression of the "thermal effective mass"; in this expression, m_ω is called the "ω mass" and m_k is called the "k mass."[35] The ω mass is equal to the reciprocal quasiparticle weight Z^{-1}.

If we consider only the on-site Coulomb interaction as the origin of the electron correlation and average out the fluctuation of the neighboring sites as a mean field, the self-energy depends only on the quasiparticle energy ω, *i.e.*, $\Sigma(\vec{k},\omega) \equiv \Sigma(\omega)$. Then, the effective mass becomes (since $m_k/m_b = 1$)

$$\frac{m^*}{m_b} = \left(1 - \frac{\partial \mathrm{Re}\Sigma(\omega)}{\partial\omega}\Big|_{\omega=E_F}\right) \equiv Z^{-1} .$$

Therefore, the vanishing of the quasiparticle weight Z at the MIT point corresponds to a critical enhancement of the effective mass.

However, in general, since the electron correlation is not necessarily confined to each atomic site, we may need to take into account the effect of the nonlocal exchange and/or correlation,[72] *i.e.*, the momentum derivative of the self-energy $\partial\Sigma(\vec{k}_F, E_F)/\partial\vec{k}$ is considerably different from zero.[62] The screening of the Coulomb potential can reduce $\partial\Sigma(\vec{k}_F, E_F)/\partial\vec{k}$, because in well-screened systems such as conventional metals, the Coulomb potential is no longer long range and the nonlocality of the exchange interaction is small. However, in most of the perovskite-type TM oxides, the carrier density is fairly small, and this effect will be more significant especially in the vicinity of the MIT point.

We consider that, near the MIT point, the ω mass increases significantly, reflecting $Z \to 0$; on the other hand, the contribution of the momentum-dependent self-energy becomes significant due to poor screening, which results in a decrease of the k mass. Thus, the critical enhancement of the effective mass, which is a product of the ω mass and the k mass, can be suppressed under some conditions. This is not only a plausible idea of explaining the behavior of the effective mass but also a model, as we describe in Chap. 5, that provides a desirable picture of the reduction of the spectral intensity at the Fermi energy observed in the photoemission and inverse-photoemission spectroscopies.[59,62,73]

Nevertheless, it is rather a challenging problem to evaluate the "intrinsic" effect of the

long range Coulomb interaction only from the value of the k mass, because the value of the k mass depends strongly on what kind of band calculation we use instead of the non-interacting Bloch electron ε_k^o in Eq. 4.8. (ω mass is considered not to depend on the definition of ε_k as much as the k mass does.) In this study, we have used the band calculation with LDA. In the LDA calculation, the exchange potential is approximated by a local potential, which underestimates the bandwidth,[74] and thus overestimates $D^{\mathrm{LDA}}(E_\mathrm{F})$. Therefore,the value of m^*/m_b is somewhat reduced; this may lead us to derive larger $\partial\Sigma(\vec{k}_\mathrm{F}, E_\mathrm{F})/\partial\vec{k}$ than the intrinsic value.

We discuss this issue again in Chapter 5.

4.3.4. Electrical resistivity

The electrical resistivities collected on both heating and cooling cycles between 350 K and 4 K show no difference within the experimental accuracy. In some cases, the resistivity shows clear dependence on the crystallographic direction; *i.e.*, when the measuring current flows parallel to the [100] axis of the pseudocubic perovskite, the resistivity is different from that when the current flows along the [110] axis. This anisotropy, however, is not temperature dependent. Whenever we observe such anisotropy, we normalize each data set to the residual resistivity ρ_o, and the resulting curves fit each other completely.

The scaling factor $c \equiv \rho^{[110]}(T)/\rho^{[100]}(T)$, varies from ~ 1.1 to ~ 1.5. However, there seems to be neither a systematic relation between c and the Sr content x, nor consistency among the different sets of the measurements for the samples with the same value of x.

Thus, we consider that the observed anisotropy is not due to any particular feature of the electronic structure of the system. Similar behavior has been reported in the resistivity of the single-crystal $CoSi_2$ with cubic C1 structure,[75] and also high-purity cubic aluminum single crystal.[76] In the former material, it was pointed out that the anisotropy can be attributed to an extrinsic origin, *e.g.*, point defects and/or dislocations that appeared during crystal growth, though no trace of such defects has yet been observed.[75] It has been argued that, in the case of the Al single crystal, a model calculation for ⟨211⟩ dislocations predicts an anisotropy of electrical resistivity compatible with experiment.[77] Therefore, we suggest that the anisotropy in our resistivity measurements may also be caused by the presence of a small amount of defects and/or dislocations.[78] Despite this undesirable artifact, if we make the size of the rectangular parallelepiped as small as $2 \times 0.5 \times 0.3\,\mathrm{mm}^3$, the absolute values of the electrical resistivity data can be reproduced within the ±15 % error bar (the temperature dependence is completely reproducible as mentioned above) irrespective of the direction of the measuring current. With all these considerations, the data were collected as shown in Fig. 4.14.

At first sight, all of the data seem to be well expressed by the relation $\rho = \rho_o + AT^2$ for the measured temperature range. However, when we try to fit the observed resistivity using this expression, we cannot fit the data over the entire temperature range from 4 K to 350 K using a single value of the coefficient A. Therefore we assume that the resistivity is expressed by $\rho_o + AT^2$ plus an *additional term*.

First, we consider here that the AT^2 term is due to electron-phonon scattering. It has been suggested, especially in strongly-coupled superconductors, that the AT^2 term is due to the breakdown of the momentum-conservation law in the electron-phonon scattering process.[79] Here the coefficient A is shown to be related to both the residual resistivity ρ_o and the Debye temperature Θ:

$$A = \alpha \times \frac{\rho_o}{\Theta^2} \tag{4.10}$$

with α varying from ~ 0.01 to ~ 0.1. However, the A values in the $Ca_{1-x}Sr_xVO_3$ system, which are roughly estimated as $\sim 1 \times 10^{-9}\,\Omega\mathrm{cm/K}^2$, are three orders larger than

$$\alpha \times \frac{\rho_o}{\Theta^2} = \alpha \times \frac{\sim 1 \times 10^{-5}\,(\Omega\mathrm{cm})}{(\sim 5 \times 10^2)^2\,(\mathrm{K}^2)} = \sim 4 \times 10^{-12}\,(\Omega\mathrm{cm/K}^2)\,,$$

even if we assume the largest value of $\alpha \sim 0.1$. (Here we used the Debye temperature estimated from the specific-heat measurement.) Furthermore, Gurvitch has discussed that a strong electron-phonon interaction is insufficient for the T^2 law; the simultaneous presence of strong coupling and disorder is also necessary.[80] He has also pointed out that, in some cases, Eq. 4.10 is not applicable; *i.e.*, there is an empirical condition for the appearance of the T^2 law:

$$(\lambda - 0.7) \times \rho_o > \sim 13\,(\mu\Omega\mathrm{cm})\,,$$

where λ is the electron-phonon coupling constant. In the $Ca_{1-x}Sr_xVO_3$ system, however, λ is at largest ~ 0.3 as discussed in Sec. 4.3.3, and ρ_o is $\sim 1 \times 10^{-5}\,\Omega$cm. Hence, the last formula is not satisfied. (In the first place, even the value of λ is smaller than 0.7.) Following these arguments, it appears unlikely that the T^2-dependent resistivity in $Ca_{1-x}Sr_xVO_3$ arises from electron-phonon scattering. However, this kind of contribution to the T^2 term is not completely neglected and will be discussed again below.

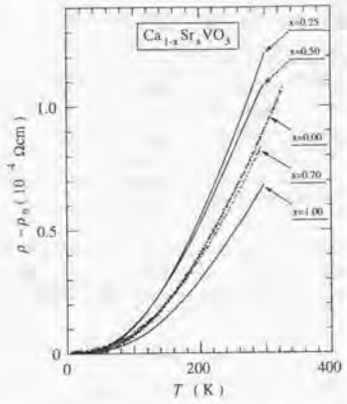

FIG. 4.14. Electrical resistivities of the $Ca_{1-x}Sr_xVO_3$ single crystals for $x = 0.00$, 0.25, 0.50, 0.70, 1.00. For each data set, the lowest resistivity at ~4 K has been subtracted as the residual resistivity ρ_o.

An alternative and more likely origin of the T^2 term is electron-electron scattering in the presence of the umklapp process. Let us consider here the resistivity as modeled by a three-component expression of the form

$$\rho = \rho_o + \rho_{e\text{-}e}(T) + \rho_{e\text{-}ph}(T)\,,$$

where ρ_o is a temperature-independent background contribution due to static disorder, $\rho_{e\text{-}e}(T) \equiv AT^2$ is the electron-electron scattering. By a line-shape analysis such as is shown in Fig. 4.15, we found that the third term $\rho_{e\text{-}ph}(T)$ is well represented by the classical Bloch-Grüneisen formula for electron-phonon scattering with $n = 5$, developed for an isotropic Fermi surface and a simple phonon spectrum:

$$\rho = \rho_o + AT^2 + \frac{4\kappa T^n}{\Theta^6} \int_0^{\Theta/T} \frac{e^z z^n dz}{(e^z - 1)^2} \quad (n = 5) \tag{4.11}$$

We have done a least-squared-error fit to all the data using Eq. 4.11 and the obtained parameters are summarized in Table 4.V and also in Fig. 4.16. If we accept $\sim \pm 15$ % error bar, we can conclude that each of the fitted parameters shows systematic behavior as a function of Sr content x.

ρ_o shows a maximum at $x = 0.5$. This reflects that the system has the maximum amount of randomness at that composition.

We note that our effective transport Debye temperature $\Theta \sim 700$ K does not sound

TABLE 4.V. Fitted parameters for the electrical resistivity of $Ca_{1-x}Sr_xVO_3$ with Eq. 4.11.

x	$\rho_o\,(\Omega\mathrm{cm})$	$A\,(\Omega\mathrm{cm/K^2})$	$\kappa\,(\Omega\mathrm{cm\,K})$	Θ (K)
0.00	8.668×10^{-6}	5.911×10^{-10}	0.114	793.5
0.25	1.319×10^{-5}	9.118×10^{-10}	9.476×10^{-2}	722.2
0.50	1.827×10^{-5}	7.900×10^{-10}	7.441×10^{-2}	647.3
0.70	8.656×10^{-6}	6.796×10^{-10}	8.073×10^{-2}	811.5
1.00	6.205×10^{-6}	4.208×10^{-10}	0.121	866.3

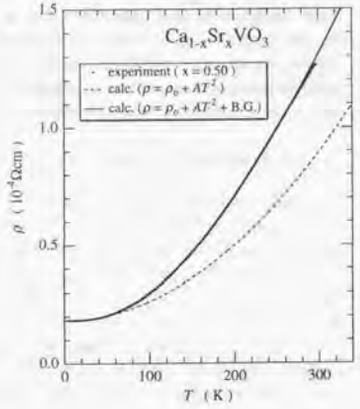

FIG. 4.15. Electrical resistivity of $Ca_{0.5}Sr_{0.5}VO_3$ against temperature T (dots). The solid line represents Eq. 4.11, while the broken line represents Eq. 4.11 without the Bloch-Grüneisen term.

physical. However, it is not necessary for the transport Θ to be equal to the thermodynamic value $\Theta \sim 350\,\mathrm{K}$ obtained from the specific heat measurements. This is because our transport Debye temperatures were derived by assuming that all the phonons which interact with electrons might contribute as the acoustic modes (the third term of Eq. 4.11), whereas the thermodynamic Debye temperatures were derived by considering all types of phonons more adequately.[81]

The values of κ and Θ show a minimum at $x = 0.5$, indicating that the lattice becomes softest at this composition. The electron-phonon coupling constant λ is related to both κ and Θ as follows:

$$\lambda \propto \frac{\omega_p^2}{\Theta^2}\kappa\,,$$

where ω_p is the plasma frequency of the conduction electrons. Makino *et al.* reported[61] that the variation of ω_p in going from $SrVO_3$ to $CaVO_3$ is systematic but very small, and the variation of λ inferred from the Sommerfeld-Wilson ratio R_W is also small. Thus we can roughly estimate that $\kappa \sim \Theta^2$. This is consistent with the behaviors shown in Fig. 4.16.

It is surprising that the contribution of the electron-electron scattering, which is in general dominant at very low temperature, is significantly large even at room temperature. In $Ca_{0.5}Sr_{0.5}VO_3$,

$$\rho_{e\text{-}e}(300\,\mathrm{K}) : \rho_{e\text{-}ph}(300\,\mathrm{K}) \sim 2:1\,.$$

This is further evidence that the electron correlations are significantly large in this system. The coefficient A should, then, reflect the enhancement of the effective mass of the quasi-particles due to this electron correlation. The resistivity due to electron-electron (*i.e.*, quasiparticle – quasiparticle) scattering can be crudely but quantitatively expressed as follows:

$$\rho_{e\text{-}e}(T) = \frac{m_b}{ne^2\tau}$$

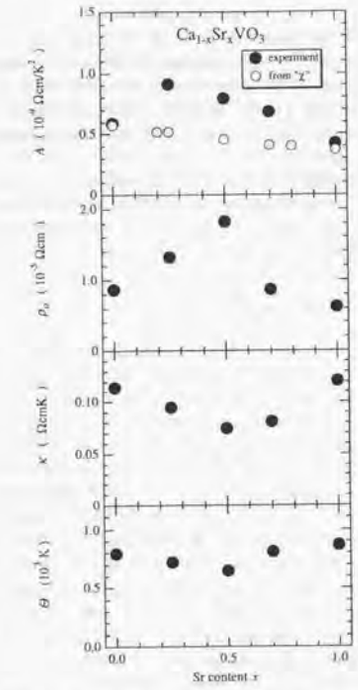

FIG. 4.16. Fitted parameters for the electrical resistivity: A, ρ_o, and κ, against Sr content x. The A values deduced from the Pauli paramagnetic susceptibility under the assumption of $R_W = 2$ and the Kadowaki-Woods ratio is $1.0\times10^{-5}\,\mu\Omega\,\mathrm{cm\,mol^2\,K^2\,(mJ)^{-2}}$ are also plotted for comparison (top).

$$= \frac{m^* v_F}{e^2 n^{2/3}}\left(\frac{k_B T}{E_F}\right)^2$$
$$= \frac{4k_B^2\, m^{*2}}{\hbar^3 e^2 n^{2/3} k_F^3} T^2$$
$$\equiv AT^2\,,$$

where

$$v_F = \hbar k_F / m^*$$
$$E_F = \hbar^2 k_F^2/(2m^*)\,,$$

and we have assumed the scattering time τ is equal to the life time of the thermally activated quasiparticle,[82] *i.e.*,

$$\tau^{-1} = v_F n^{1/3} E_F^{-1} Z^{-1} \mathrm{Im}\Sigma$$
$$\simeq v_F n^{1/3}(m^*/m_b)(k_B T/E_F)^2\,.$$

Hence, the coefficient A is proportional to the quadratic of the effective mass m^*. The obtained value of A increases systematically in going from $x = 1$ to $x = 0.25$; this may correspond to the increase of m^*/m_b. However there seems to be a rapid decrease between $x = 0.25$ and $x = 0$ which is not consistent with the behavior of m^*/m_b. This cannot be explained by the considerably large error arising from the quality of the sample ($\sim\pm15\,\%$).

In Fig.4.16 (top), we also plot the value of A deduced from the Pauli paramagnetic susceptibility χ_P under a few reasonable assumptions: we use a Sommerfeld-Wilson ratio $R_W = 2$ to estimate the electronic specific heat γ from χ_P, since R_W is almost equal to 2 in this system. The obtained γ corresponds to the electronic specific heat which is not affected by the electron-phonon interaction. Then we use the Kadowaki-Woods ratio A/γ^2, which is a measure of the electron correlation, with the same value as that of the heavy fermion systems,[83] *i.e.*, $A/\gamma^2 = 1.0\times10^{-5}\,\mu\Omega\,\mathrm{cm\,mol^2\,K^2\,(mJ)^{-2}}$, and from this deduce a value of A for $Ca_{1-x}Sr_xVO_3$. The resulting A values are compared to the experimentally observed values (Fig. 4.16, top).

Since the above assumptions for the Sommerfeld-Wilson ratio and the Kadowaki-Woods ratio in this system seem to be fairly appropriate, we can safely say that the AT^2 term in the resistivity of the end members $CaVO_3$ ($x = 0$) and $SrVO_3$ ($x = 1$) can be

attributed solely to the electron-electron scattering. For the other solid solutions ($0 < x < 1$), there must be other contributions to the AT^2 term. The most probable candidate of this additional contribution of the T^2 term is the interference between the elastic electron scattering by disorder and the electron-phonon scattering, which has been recently investigated by Ptitsina *et al.*[84] This effect must be proportional to the residual resistivity, and our data seems to support the scenario.

On the other hand, we know that the Kadowaki-Woods ratio is not necessarily equal to the above value. Then, there are several other possible explanations for the observed x dependence of A. Firstly, we must consider a possible contribution from the modification of the Fermi surface. Since A is not only proportional to m^{*2} but also to ${k_F}^{-3}$, a variation of the shape of the Fermi surface due to the orthorhombic distortion may lead to significant changes in A. As we apply pressure to $CaVO_3$, the value of A tends to decrease,[68,85] though it has not yet been determined how the lattice constants change under pressure. We should also remark that samples around $x = 0.25$ have a tendency to show the smallest spectral weight at the Fermi energy as we show in Sec. 5.3.4 from the results of the photoemission spectroscopy; this has also been manifest in the inverse photoemission spectroscopy of the $Ca_{1-x}Sr_xVO_3$ single crystals.[86] Such behaviours may be related to the hybridization between the V $3d$ t_{2g} orbitals and the O $2p$ σ orbitals. Okimoto *et al.* calculated a distortion-induced admixture between those orbitals,[87] and Lombardo *et al.* discussed a possible scenario involving spectral weight transfer in the $Ca_{1-x}Sr_xVO_3$ system due to charge transfer.[88] This distortion-induced charge transfer may explain the strange revival of the quasiparticle weight in the region close to $CaVO_3$, and this hybridization may also explain the x dependence of the value of A, although this should also be consistent with the monotonic increase of the effective mass toward $CaVO_3$ as estimated from the Pauli paramagnetism. Finally, the contribution of the momentum dependence of the self-energy, which becomes significant in the region closer to $CaVO_3$,[59,62] is also an intriguing candidate to explain the behavior of A. Apparently, with a large momentum dependence of the self-energy, it is no longer necessary that A is proportional to m^{*2}. These issues will be clarified by further investigations.

4.4. Summary

We have succeeded in preparing single crystals of the metallic alloy system $Ca_{1-x}Sr_xVO_3$ for the first time, as far as we are aware of. The system has nominally one $3d$ electron per vanadium ion; as we substitute a Ca^{2+} ion for a Sr^{2+} ion, the bandwidth W decreases due to the buckling of the V-O-V bond angle from $\sim 180°$ for $SrVO_3$ to $\sim 160°$ for $CaVO_3$, which is almost equal to that of the $LaTiO_3$. As we described in Chap. 3, $CaVO_3$ matrix shows several peculiar transport properties under the oxygen off-stoichiometry. As well as the issue, the crystal distortion of $CaVO_3$ is the same as that of the analogous $3d^1$ insulator $LaTiO_3$; thereby, it is rather reasonable to consider that $CaVO_3$ is close to the boundary of MIT, though we have to consider the difference of Ti^{3+} and V^{4+}. The Sommerfeld-Wilson ratio $R_W \simeq 2$, the Kadowaki-Woods ratio A/γ^2 lies in the same region as the heavy Fermion compounds, and there is a large contribution from electron-electron scattering to the resistivity even at room temperature. These features are considered to provide strong evidence of the large electron correlations in this system. However, the effective masses obtained by the thermodynamic (γ) and magnetic (χ_P) measurements show only a moderate increase in going from $SrVO_3$ to $CaVO_3$, instead of the diverging behaviors expected from the Brinkmann-Rice picture.

The elaborate bandwidth control in $Ca_{1-x}Sr_xVO_3$ has demonstrated that the mass enhancement due to the reduction of the bandwidth is not so large, even though the system shows some fingerprints of strong electron correlations. Accordingly, we suggest that these seemingly contradicting metallic properties observed in this system can be explained by considering the effect of nonlocal electron correlations, *i.e.*, the momentum-dependent self-energy.

Chapter 5

Systematic Spectral Weight Redistribution in the Quasi-Particle Spectra of $Ca_{1-x}Sr_xVO_3$.

Part of this chapter has been published as Ref. 59, Ref. 60, Ref. 89, and Ref. 90.

5.1. Introduction

One of the most challenging problems in condensed matter science is the whole understanding of the spectral weight redistribution[55] that occurs, especially, in correlated electron systems. From various viewpoints, challenges have been made to describe how the single-particle spectral density $\rho(\omega)$ behaves in a system close to a Mott transition. In the original treatment by Hubbard,[6] the Mott transition, or, alternatively the Mott-Hubbard transition, is controlled by the relative magnitudes of the on-site Coulomb energy U and the one-electron band width W. If the number of electrons per atomic site is an integer, the splitting between the lower and upper Hubbard bands (LHB and UHB) gradually increases with increasing U/W and the MIT occurs at $U/W \sim 1$, where a Mott-Hubbard gap opens. This treatment provides a reasonable picture for $\rho(\omega)$ in the insulating region, whereas it does not properly treat low energy excitations and the Fermi-liquid properties in the metallic region. On the contrary, a Fermi-liquid description has been given by Brinkman and Rice[10] in their Gutzwiller treatment[11] of the Hubbard model, but high-energy excitations are missing there. These two traditional approaches are schematically shown in Fig. 5.1.

The most suitable tool that provides information on $\rho(\omega)$ is high-energy spectroscopy. Fujimori et al. reported the ultraviolet photoemission spectroscopy (UPS) spectra of several Ti^{3+} and V^{4+} compounds and indicated that $\rho(\omega)$ consists of a band of quasi-particle excitations near the Fermi energy (E_F) and a high energy satellite signaling the formation of the LHB.[91] They also suggested that the spectral weight is transferred from the quasi-particle band to the precursor of the LHB with increasing U/W.

Recent theoretical predictions of the Hubbard model treated within the Local Impurity Self-consistent Approximation (LISA)[92] which is exact in the limit of large lattice connectivity, or equivalently, large dimensionality, have given similar illustrations of $\rho(\omega)$ by simultaneously treating the atomic aspect and the itinerant aspect of on-site quantum fluctuations.[92–94] As observed in the experiment, we see in this theoretical prediction that $\rho(\omega)$ splits into a characteristic three-peak structure, when the transition is approached by increasing U/W. There is a central quasi-particle peak at the Fermi energy of width

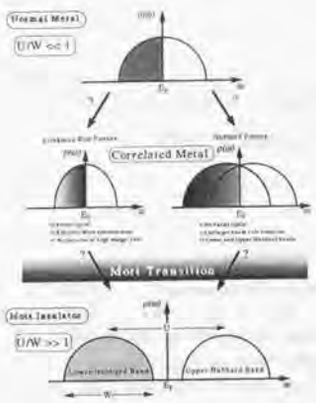

FIG. 5.1. Schematic picture of the spectral weight transfer as we control U/W ratio from $U/W \ll 1$ (normal metal) to $U/W \gg 1$ (Mott insulator) described by the two traditional approaches: Hubbard scenario[6] and Brinkmann-Rice scenario.[10] In the "correlated" metallic state near the Mott transition, *i.e.*, $U/W \sim 1$, the Brinkmann-Rice picture can describe the Fermi-liquid properties, however, it fails to predict high-energy satellites. Alternatively, the Hubbard picture can describe the appearance of the high-energy features, whereas it violates the Luttinger's sum rule, and thus fails to satisfy the Fermi liquid argument

ε_F^*, where ε_F^* is the renormalized Fermi energy, which decreases as the transition is approached. This indicates the enhancement of the effective mass. The quasiparticle peak is accompanied by the incoherent lower and upper Hubbard bands that emerge at energies of the order of $\pm\frac{U}{2}$. These features also acquire the spectral weight which is transferred from around E_F as the central peak narrows.

In this study, we investigate more systematically how $\rho(\omega)$ actually changes as we control U/W within a single Mott-Hubbard system $Ca_{1-x}Sr_xVO_3$. As we have shown in Chap. 4, both $CaVO_3$ and $SrVO_3$ are metallic perovskite-type V^{4+} oxides, which have nominally $3d^1$ configuration. $CaVO_3$ is near an MI transition because the V-O-V bond angle is $\sim 160°$ which is almost equal to that of a $3d^1$ Mott insulator $LaTiO_3$, whereas $SrVO_3$ (V-O-V bond angle is $\sim 180°$) is considered to be less correlated. This is because the buckling of the V-O-V bond angle reduces the overlap between neighboring $3d$ orbitals mediated by oxygen $2p$ orbitals, leading to a decrease in W by a factor of $\cos(\angle\text{V-O-V})$. Therefore, as one changes the Sr concentration (x) in $Ca_{1-x}Sr_xVO_3$, one can control the U/W ratio. We note that since the average number of $3d$ electrons is always one per V atom, one can study the change of the electronic properties as functions of only the U/W ratio.

With this point in mind, the electronic structure of $Ca_{1-x}Sr_xVO_3$ was probed for several values of x using photoelectron spectroscopy, part of which has already been published and has invoked stimulating discussion.[59,62,90] The photoemission spectra reported so far were very different from the density of state (DOS) obtained by the band calculation with the local density approximation (LDA). This indicates a presence of strong electron correlation in this system. These results are reviewed and discussed anew in Sec. 5.3.4.

On the other hand, it was questioned that the electronic structure of $Ca_{1-x}Sr_xVO_3$ at the surface might be different from that in the bulk. Then, we tried to perform a novel way of photoemission spectroscopy described in Sec. 5.3.5 to separate out the surface and bulk contributions from the total spectrum for any given composition. Surprisingly, this technique has revealed a novel MI transition, which has never been observed in any materials. The MI transition is only realized at the surface of this $Ca_{1-x}Sr_xVO_3$ system with the change of x, while the bulk remains metallic. Furthermore, we have found an interesting property that this MI transition is caused by the charge disproportionation at the surface. These issues are discussed in Sec. 5.3.5.

We hope that the latter newborn method will be more mature and be regarded as the standard of the photoemission experiment in the near future, however, it is at present still preliminary as due to an insufficient resolution, naive hypotheses, and arbitrariness for choosing parameters. Therefore, it is the most preferable attitude at this stage to recognize that the *valid argument* can only be done on the common results extracted from both the ordinary and the brand-new experiments.

5.2. Experiments

All the single-crystalline $Ca_{1-x}Sr_xVO_3$ samples were prepared and characterized as described in the previous chapters. For all the samples studied here, oxygen contents were carefully controlled to become 3.00 ± 0.01.

The measurements reported here were performed in three places: Electrotechnical Laboratory (ETL), Photon Factory (PF), and Indian Institute of Science (IISc).

For the experiments in ETL, we used two light-sources (an ultra-violet light source and an x-ray source) and an energy-analyzer (VG Microtech, CLAM-II) followed by an electron detector. These are fitted to a UHV chamber ($\sim 2\times10^{-8}$ Pa), which is made of "Mu-metal" with low residual magnetic field in the chamber (typically < 5 mG). We cleaned the surfaces of the samples thoroughly by *in-situ* scraping in this ultra-high vacuum spectrometer using a diamond file with particular care against possible surface degradation effects. The samples were cooled down to ~ 15 K using a closed-cycle He-gas refrigerator, and this temperature was maintained during both the scraping procedures and measurements to avoid desorption of oxygens from the surfaces. By *in-situ* scraping of the surfaces, the large spectral intensity in a characteristic region (the binding energy of $9 \sim 12$ eV) below E_F, is eliminated drastically. Corresponding changes are also observed in Mg Kα x-ray photoemission spectra of the oxygen 1*s* core-level. The significant satellite peaks at a larger binding energy region disappear by scraping. Photoemission spectra obtained after *in-situ* scraping are well reproducible. Additional features observed before the surface cleaning are considered to originate from surface degradation; therefore we checked the O 1*s* spectrum after each scraping. As a reference of E_F and the instrumental resolution, we measured the spectrum of Fermi cutoff of Au evaporated on the sample. The total energy resolutions were 35 meV for UPS and 0.7 eV for XPS. We also measured the relative intensity and the energy position of the weak satellite line of the He discharge lamp from this Au spectrum; which are subtracted from all the UPS spectra shown here.

The complementary XPS and UPS measurements were carried out in IISc at liquid nitrogen temperature ($\sim$80 K) in a vacuum of 4×10^{-10} mbar with total energy resolutions of 0.8 eV for XPS and 80 meV for UPS. The cleanliness of the sample surface was maintained by periodical in-situ scraping with an alumina file. Reproducibility of the spectra with repeated scrapings was confirmed for each composition.

We did other experiments using synchrotron light-sources in PF. We measured, in BL-11D, some poly-crystalline $Ca_{1-x}Sr_xVO_3$ samples at liquid nitrogen temperature using photon energies corresponding to the V 3*p* core-level threshold: *i.e.*, 45 eV for off-resonance and 50 eV for on-resonance. XAS experiments were performed at the undulator beamline BL-2B in PF using a 10 m grazing incidence monochromator.[95] The experiment was carried out for poly-crystalline samples at room temperature in the ultrahigh vacuum chamber (7.5×10^{-10} Torr). The x-ray absorp-

tion spectra were indirectly measured by the total electron-yield mode by assuming that the absorption cross section should be proportional to the number of the decay products of the core excitation, and this should be reflected to the total photocurrent. The energy resolution of this measurement was about 0.18 eV. For both measurements, we did *in-situ* surface scraping using a diamond file.

5.3. Results and discussion

5.3.1. Surface degradation effect in the XPS spectrum

The Mg Kα ($\hbar\omega$ = 1253.6 eV) XPS spectra of the V $2p_{3/2}$ ($\sim$ 521 eV), $2p_{1/2}$ ($\sim$ 528 eV), and O 1*s* ($\sim$ 534 eV) core levels of $Ca_{1-x}Sr_xVO_3$ measured at $\sim$ 14 K are plotted in Fig. 5.2. The spectra were taken just after *in-situ* surface scraping and 24 hours later. We recognize the appearance of the tail on the O 1*s* peak around $\sim$537 eV 24 hours after the *in-situ* surface scraping. The other part of the spectrum does not change so much, although both the O 1*s* peak and V $2p_{3/2}$ peak apparently consist of a few components, which could be considered to be due to the surface degradation effects. However, except for this high energy tail of the O 1*s* peak, the whole spectrum is sufficiently reproducible, so that we consider the components of the peaks are intrinsic.

On the other hand, the Ca $2p_{3/2}$ ($\sim$351 eV) and $2p_{1/2}$ ($\sim$ 355 eV) core levels at $\sim$ 14 K (Fig. 5.3) do not show any differences in this 24 hours. This is also true for the Sr 3*d* core-level spectrum. It is possible the *A* site cations are always absent at the surface by desorption, because the ionic *A* site cations can leave the surface rather easily, compared with the more covalent O and V ions. In this case, on the surface layer, the electronic states should be considerably different from those of the bulk. This is always an important problem for the photoemission spectroscopy; we try to discuss this issue further in Sec. 5.3.5.

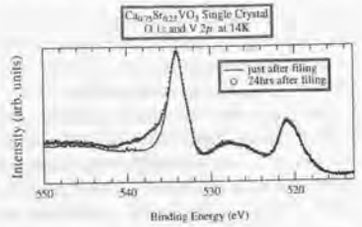

FIG. 5.2. XPS spectra of the V $2p_{3/2}$ ($\sim$521 eV), $2p_{1/2}$ ($\sim$528 eV), and O 1*s* ($\sim$534 eV) core levels of $Ca_{1-x}Sr_xVO_3$ measured at $\sim$ 14 K. The spectra were taken just after *in-situ* surface scraping (solid line), and 24 hours later (open circles).

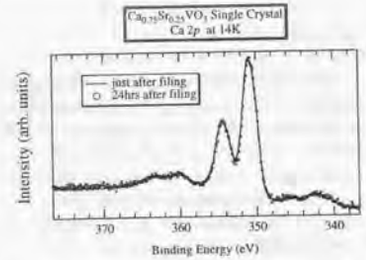

FIG. 5.3. XPS spectra of the Ca $2p_{3/2}$ ($\sim$351 eV) and $2p_{1/2}$ ($\sim$355 eV) core levels of $Ca_{1-x}Sr_xVO_3$ measured at $\sim$ 14 K. The spectra are taken just after *in-situ* surface scraping (solid line), and 24 hours later (open circles).

5.3.2. X-ray photoemission spectroscopy

In Fig. 5.4, V 2*p* and O 1*s* core level XPS spectra of the $Ca_{1-x}Sr_xVO_3$ single crystals (x = 0.00, 0.25, 0.50, 0.75, and 1.00) taken at 14 K in ETL are plotted with an appropriate correction for the transmission characteristics of the CRAM-II analyzer and with the subtraction of the Mg K$\alpha_{3,4}$ satellites. Although

all the spectra were obtained just after the *in-situ* surface scraping and we have confirmed that the shape of each spectrum was highly reproducible, it is apparent that neither of the peaks have a single peak structure, even for $CaVO_3$ and $SrVO_3$, as can be expected from a homogeneous single-phase V^{4+} compound. This shape is highly reproducible; upon scraping, only the intensity around 533 eV, ascribed to the surface deterioration, is reduced drastically, while the other parts remain almost unchanged. Almost the same spectral shape has been corroborated by Morikawa,[96] and by our own independent measurements in IISc. In particular, the V $2p_{3/2}$ peak is extremely broad and seems to be composed of three different features, as first pointed out by Morikawa.[96] This is a very peculiar observation, because in this system, there is no reason to consider three distinctively different electronic states for the V ion in the bulk.

Therefore, we have tried to decompose the V 2*p* spectrum as well as the O 1*s* spectrum into three independent components by a least-squares line-shape analysis method.

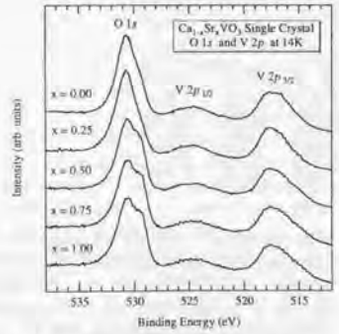

FIG. 5.4. V 2*p* and O 1*s* core level XPS spectra of the $Ca_{1-x}Sr_xVO_3$ single crystals with x = 0.00, 0.25, 0.50, 0.75, and 1.00 at 14 K, just after the *in-situ* surface scraping. The spectra were measured in ETL and we confirmed the shape of each spectrum were highly reproducible.

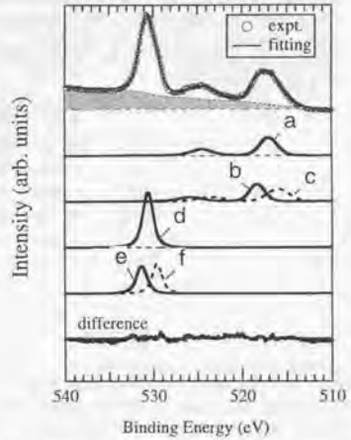

FIG. 5.5. Line-shape analysis of the V 2*p* and O 1*s* spectrum of $Ca_{1-x}Sr_xVO_3$ with x = 0.00. The spectrum is fitted by a superposition of three independent components for the V 2*p* peak (denoted by "a", "b", and "c" in the figure) and the other three independent components for the O 1*s* peak (denoted by "d", "e", and "f" in the figure). The secondary electron spectrum (shaded area) has been subtracted from the measured spectrum (open circles), assuming the ordinary Shirley background.[97] Curves a, b, and c correspond to the components of the V 2*p* peak, and curves d, e, and f of the O 1*s* peak. The calculated curve fits rather well to the experimental data.

First, we have subtracted the secondary electron spectrum, which represents the inelastic events after the photoexcited electron has left the site of the excitation process. The formula of the secondary electron spectrum function has been discussed intensively by Tougaard *et al.*;[98] however, we used here the simple Shirley background[97] (shaded area in Fig. 5.5). In the line-shape analysis, each peak was assumed to be a Lorenzian with the

TABLE 5.I. Fitted parameters for the line-shape analysis of the V $2p$ core-level XPS spectra of $Ca_{1-x}Sr_xVO_3$ with $x = 0.00$, 0.25, 0.50, 0.75, and 1.00. Each spectrum has been decomposed into three components, called "b", "a" and "c" from the higher binding energy to the lower one (See Fig. 5.5). The Lorenzian width of the V $2p_{3/2}$ peak is 0.316 eV independent of the components, and those of the V $2p_{1/2}$ peak are 1.218 eV ("b"), 0.838 eV ("a"), and 0.868 eV ("c"). In this table, Δ stands for the full width at half maximum (eV) for the Gaussian. E_B (eV) is the binding energy, and I (arbitrary units) is the intensity of the peak.

x	0.00	0.25	0.50	0.75	1.00
E_B^b	518.25	518.18	518.16	518.25	518.26
Δ^b	0.981	1.023	1.142	1.211	1.261
I^b/I^a	0.858	0.873	0.993	0.840	0.844
E_B^a	516.96	517.18	517.01	517.02	517.02
Δ^a	1.148	1.185	1.227	1.244	1.258
E_B^c	515.91	516.02	515.88	515.30	515.31
Δ^c	1.552	1.573	1.634	1.639	1.636
I^c/I^a	0.862	0.972	1.016	0.878	0.901

TABLE 5.II. Fitted parameters for the line-shape analysis of the O $1s$ core-level XPS spectra of $Ca_{1-x}Sr_xVO_3$ with $x = 0.00$, 0.25, 0.50, 0.75, and 1.00. Each spectrum has been decomposed into three components, called "e", "d" and "f" from the higher binding energy to the lower one (See Fig. 5.5). The Lorenzian width of the O $1s$ peak is 0.438 eV independent of the components. In this table, Δ stands for the full width at half maximum (eV) for the Gaussian. E_B (eV) is the binding energy, and I (arbitrary units) is the intensity of the peak.

x	0.00	0.25	0.50	0.75	1.00
E_B^e	531.32	531.71	531.18	531.25	531.26
Δ^e	0.539	0.571	0.627	0.697	0.750
I^e/I^d	0.508	0.514	0.894	0.849	0.848
E_B^d	530.60	530.69	530.45	530.45	530.45
Δ^d	0.504	0.492	0.471	0.472	0.488
E_B^f	529.58	529.62	529.44	529.38	529.33
Δ^f	0.483	0.455	0.411	0.388	0.387
I^f/I^d	0.529	0.491	0.946	0.908	0.936

natural widths[99] of the V $2p$ and O $1s$ core levels plus the Mg Kα radiation, and then convoluted with a Gaussian. The Gaussian width represents the total instrumental resolution and, in general, several other broadening effects, such as the phonon contribution, mixing with the ligand, multiplets, and so on.[100]

The resulting best fit of the least-squares line-shape analysis and the components are shown in Fig. 5.5, and the fitting parameters are listed in Tables 5.I and 5.II. Each spectrum can be decomposed into six components, which are called "b", "a" and "c" for the V $2p$ peak and "e", "d" and "f" for the O $1s$ peak from the higher binding energy component to the lower one (Fig. 5.5). The Lorenzian width of the O $1s$ peak is 0.438 eV and that of the V $2p_{3/2}$ peak 0.316 eV, both of which are independent of the components, while those of the V $2p_{1/2}$ peak are 1.218 eV

("b"), 0.838 eV ("a"), and 0.868 eV ("c"). The Lorenzian width should only reflect the natural width plus that of the Mg K$\alpha_{1,2}$ source;[99] however, we need to consider some additional effect, which makes the natural width larger, especially for the $2p_{1/2}$ peak, in order to obtain the best fit. This effect is due to the $L_2L_3M_{4,5}(2p_{1/2} - 2p_{3/2} - 3d)$ Coster-Kronig transitions.

The calculated spectrum agrees with the experimental data considerably, and this holds true for all $Ca_{1-x}Sr_xVO_3$ samples measured. The binding energies of these components remain essentially the same across the series. On the other hand, the gaussian widths and the relative intensities show a clear dependence on the value of x. The Gaussian widths show systematic changes on going from $CaVO_3$ to $SrVO_3$: for all the components of V $2p$ peak, the Gaussian widths increase, while, for the components of O $1s$ peak, Δ_e increases but Δ_d and Δ_f decrease.

The intensity ratios, however, do not change monotonically and the question whether this behavior is intrinsic or not needs to be clarified by further elaborate studies. Nevertheless, we can find an interesting feature in the result of the analysis: although the intensity ratio to the central components ("a" and "d") does not seem to behave systematically, the ratio of "b" and "c" components, as well as that of "e" and "f" components are approximately equal to 1, independent of the value of x, within the possible errors due to the the ambiguity of the secondary electron background shape, overlapped plasmon peaks, and so on. Morikawa,[96] as well as Maiti *et al.*[28] provoked independently a similar idea that the peaks "b", "a" and "c" arise from V^{3+}, V^{4+} and V^{5+} entities, and the V^{3+} and V^{5+} components are coming from the surface electronic state. A fraction of the V^{4+} ions spontaneously disproportionate according to the reaction $2V^{4+} \rightarrow V^{3+} + V^{5+}$, maintaining the charge balance. Maiti *et al.*[28] also reported that by changing the photon energy between Mg Kα (1253.6 eV) and Al Kα (1486.6 eV), thereby modestly changing the surface sensitivity of the technique, they find that the V^{3+} and V^{5+} signal intensities increase with increasing surface sensitivity. If this assumption is true, it is rather surprising that even in the XPS spectrum the surface contribution is almost twice as large as that of the bulk, although the XPS measurements is considered to be rather bulk sensitive. The attempt to separate the surface and bulk component of the UPS spectra based on this assumption by following the idea of Maiti, Mahadevan and Sarma[28] is discussed in Sec. 5.3.5.

5.3.3. X-ray absorption spectroscopy

As shown in Fig. 5.4, O $1s$ XPS spectrum also consists of three components and shows considerable x-dependence, which is sufficiently reproducible and has been corroborated by several independent experiments. These intriguing features seem to be comparable to the O $1s$ XAS spectrum, which explores the unoccupied density of states above E_F mixed with the O p character.

Figure 5.6 shows the O $1s$ XAS spectrum of poly-crystalline $Ca_{1-x}Sr_xVO_3$ samples with $x = 0.10$, 0.40, 0.50, 0.80, and 1.00 measured at room temperature. The two peaks ($\sim$529.5 eV and $\sim$531.5 eV) near the absorption edge are generally attributed to the V $3d$ unoccupied states mixed with the O $2p$ character. The peaks at higher energy ($\sim$537 eV and $\sim$544 eV) are thought to originate from the Sr $4d$ (Ca $3d$), and V $4s/4p$ unoccupied states, respectively.

In Fig. 5.7, the O $1s$ XAS spectra of poly-crystalline $Ca_{1-x}Sr_xVO_3$ with $x = 0.10$ and 1.00 are compared to the O $1s$ XPS spectra of the single-crystalline $Ca_{1-x}Sr_xVO_3$ samples with $x = 0.00$ and 1.00. The components "e" and "f" in the figure correspond to two of the three components assumed to fit the O $1s$ XPS

spectra in Sec. 5.3.2 (see Fig. 5.5). The x-dependences of the intensities of "e" and "f" peaks look quite similar to those for the two peaks in the XAS spectra near the O 1s absorption threshold. In order to consider this issue further, it is necessary to show, at first, to what extent the observed spectra can be explained by theoretical calculations.

H. Pen has calculated the corresponding XAS spectra of $CaVO_3$ by cluster model calculations.[101] According to Pen, the near-edge two peaks can be explained by assuming the ionic crystal-field splitting $10Dq \neq 0$ and the 2p-3d hybridization $(pd\sigma) = 1.8\,\mathrm{eV}$. However, these values are much smaller than those expected from the LDA band calculation, which deduces $10Dq = 2.4\,\mathrm{eV}$ and $(pd\sigma) = 2.3\,\mathrm{eV}$. Then, by using the latter parameters deduced from LDA, the cluster model calculation was modified, giving the spectrum as shown in the middle of Fig. 5.8. In this figure, we shifted the calculated spectrum by 2.04 eV from the original calculation

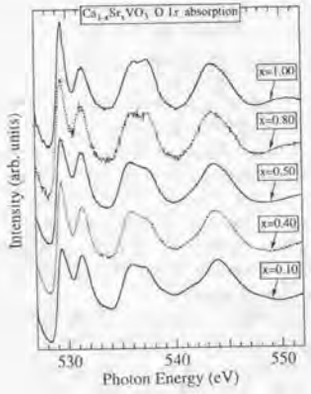

FIG. 5.6. O 1s XAS spectra of $Ca_{1-x}Sr_xVO_3$ poly crystals with $x = 0.10$, 0.40,0.50,0.80, and 1.00 taken at room temperature.

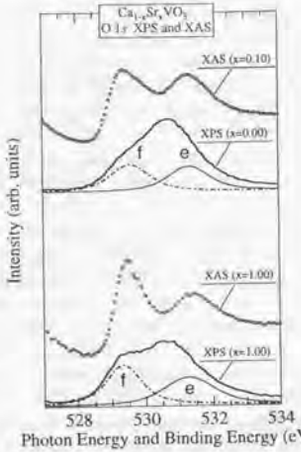

FIG. 5.7. O 1s XAS spectra of $Ca_{1-x}Sr_xVO_3$ poly crystals with $x = 0.10$ and 1.00 compared to the O 1s XPS spectra of $Ca_{1-x}Sr_xVO_3$ single crystals with $x = 0.00$ and 1.00, respectively. The components "e" and "f" correspond to those defined in Fig. 5.5. The x-dependences of the intensities of "e" and "f" peaks look quite similar to those for the two peaks in the XAS spectra near the O 1s absorption threshold.

to match the lowest energy peak of the calculation to the second peak of the experiment. On the other hand, according to the band calculation with LDA, the O p projected unoccupied DOS[101] becomes rather smooth, as shown in the bottom of Fig. 5.8. The calculated LDA spectrum is shifted by 1.88 eV toward the larger photon energy. In both calculations, the lowest-energy peak corresponds to the unoccupied V 3d t_{2g} band (orbitals), while the broad feature from $\sim$532 eV to $\sim$ 536 eV corresponds to the unoccupied V 3d e_g band (orbitals). For the LDA calculation, the e_g band is strongly overlapped by the Ca 3d (or Sr 4d for $x \neq 0$ compounds) band from $\sim$534 eV to $\sim$ 537 eV. Except for the lowest-energy peak in the experiment, the above calculations seem to explain the observed spectrum to some extent.

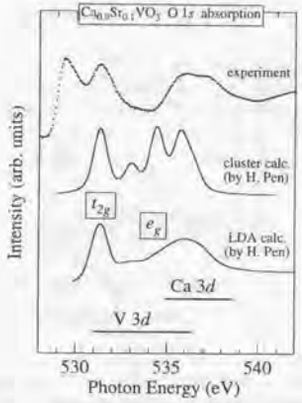

FIG. 5.8. O 1s XAS spectra of $Ca_{0.90}Sr_{0.10}VO_3$ poly crystal (dots) compared to the theoretical XAS spectra of $CaVO_3$ calculated by H. Pen.[101] The cluster calculation result with parameters $10Dq = 2.4\,\mathrm{eV}$ and $(pd\sigma) = 2.3\,\mathrm{eV}$ has been shifted by 2.04 eV toward the larger photon energy from the original result by Pen. The LDA band calculation result has also been shifted by 1.88 eV toward the larger photon energy. The horizontal bars with the notes of V 3d and Ca 3d indicate the region of each character in the spectrum derived from the LDA band calculation.

Now, we return to the deferred issue about the broad O 1s core level. The two near-edge peaks in the XAS spectrum may correspond to absorptions to the t_{2g} band from the different O 1s core levels: one is the XPS peak at the binding energy of $\sim$529.6 eV (f) and the other is at $\sim$ 531.3 eV (e). Actually, it is difficult to explain the two peaks by t_{2g} and e_g band, because the energy of the observed splitting is too small.[102] Moreover, the LDA band calculation predicts the e_g band becomes considerably broader in $SrVO_3$ compared with $CaVO_3$, but this can not be reflected in the measured spectrum if the second peak from the absorption edge was the e_g band. However, if we consider the novel idea of the two-threshold model, the following questions arise: (1) what is, in the first place, the origin of each component of the O 1s peak? (2) why does the central peak in the O 1s XPS spectrum not contribute to the XAS spectrum?

A possible answer for this question may lie in the surface effect. As reported by Abbate *et al.*,[103] the mean probing depth of the XAS measurement with the total electron-yield mode is about 19 Å; this corresponds to only about 2.5 unit cells of $CaVO_3$ along the b axis. Then, if the surface electronic state is significantly different from that of the bulk, the XAS spectrum reflects the surface electronic state predominantly rather than the bulk electronic structure. In Sec. 5.3.2, we have shown the idea of the spontaneous disproportionation of the V^{4+} ion at the surface as $2V^{4+} \rightarrow V^{3+} + V^{5+}$. In this case, the O 1$s$ spectrum is also expected to consists of two parts (*i.e.*, surface and bulk parts), one of which (the surface part) is further decomposed into two peaks, attributed to the site coordinating to V^{3+}, and the site coordinating to V^{5+}. If we follow the scenario, we need to consider that components (e) and (f) are coming from the sites coordinating to V^{3+} and V^{5+}, respectively. Correspondingly, the lowest-energy peak of the O 1s XAS spectrum is assigned to the transition to the t^1_{2g} final state and the second lowest-energy peak is assigned to the transition to the t^3_{2g} final state. The bulk contribution, *i.e.*, the transition from the "d" components of the O 1s peak, should overlap with the surface spectrum, however, the bulk is more metallic so that the spectrum is considered to be much broader.

On the contrary, if we leave the issue of the broad O 1s peak, another possible explanation is to consider a transition to the

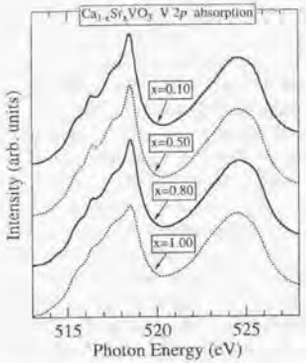

FIG. 5.9. V $2p$ XAS spectra of $Ca_{1-x}Sr_xVO_3$ poly crystals with $x = 0.10$, 0.50,0.80, and 1.00 taken at room temperature.

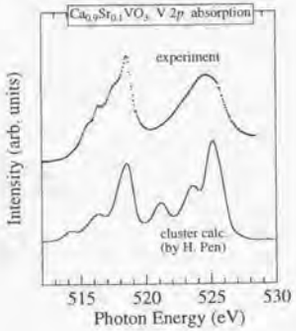

FIG. 5.10. V $2p$ XAS spectra of $Ca_{0.90}Sr_{0.10}VO_3$ poly crystal (dots) compared to the theoretical XAS spectrum of $CaVO_3$ calculated by H. Pen.[101] The cluster calculation result with parameters $10Dq = 1.5\,\text{eV}$ and $(pd\sigma) = 1.21\,\text{eV}$ has been shifted by 0.87 eV toward the larger photon energy from the original result by Pen. See text for details.

upper Hubbard band (UHB). Morikawa *et al.* measured the unoccupied DOS of $SrVO_3$ and $CaVO_3$ by the Bremsstrahlung Isochromat Spectroscopy, and observed the upper Hubbard band at $\sim 3\,\text{eV}$ above E_F. Thereby, we can assign the lowest-energy peak of the O $1s$ XAS spectrum to the transition to the coherent band at E_F, while the second peak is assigned to the O $1s \rightarrow$ V $3d$ UHB transition.

Nevertheless, the above two explanations need to be reconsidered based on other experiments; in particular, the XAS measurement of the fluorescence mode, whose mean probing depth is $\sim 1000\,\text{Å}$, should provide more definitive evidence.

Figure 5.9 shows the V $2p$ XAS spectrum of poly-crystalline $Ca_{1-x}Sr_xVO_3$ samples with $x = 0.10$, 0.50, 0.80, and 1.00 measured at room temperature. The two main features ($\sim 519\,\text{eV}$ and $\sim 525\,\text{eV}$) are attributed to the transition to the V $3d$ band from the V $2p_{3/2}$ and $2p_{1/2}$ core levels, respectively.

Using the parameter $10Dq = 1.5\,\text{eV}$, H. Pen obtained the XAS spectrum by the cluster model calculation[101] as shown in Fig. 5.10. The calculated spectrum is shifted by 0.87 eV toward the larger photon energy from the original calculation. This shift toward the larger photon energy may indicate the existence of the d^0 (V^{5+}) initial state. Furthermore, as we go from $CaVO_3$ to $SrVO_3$, the spectrum becomes broader reflecting the larger valence fluctuation.

In this way, the XAS spectra of $Ca_{1-x}Sr_xVO_3$ have provided us with many interesting problems to be unraveled. One of the questions posed here brings us to another significant issue discussed in the next section, *i.e.*, the spectral weight redistribution in the UPS spectrum, while another question is reexamined in the last section, where we try to decompose the UPS spectra into surface and bulk components.

5.3.4. Ultraviolet photoemission spectroscopy

Figure 5.11 (top) shows the UPS spectra of single-crystalline $Ca_{1-x}Sr_xVO_3$ samples with $x = 0.00$, 0.25, 0.50, 0.75, 1.00 taken at 14 K with the photon energy of $\hbar\omega = 21.22\,\text{eV}$ (top). For each spectrum,

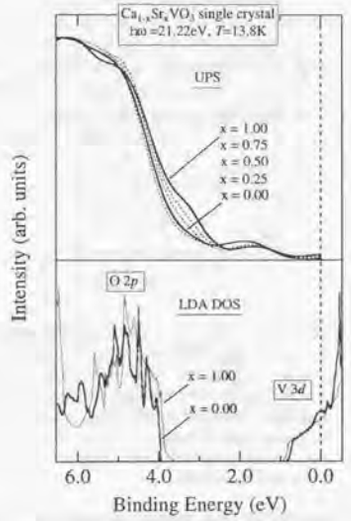

FIG. 5.11. **Top**: UPS spectra of single-crystalline $Ca_{1-x}Sr_xVO_3$ samples with $x = 0.00$, 0.25, 0.50, 0.75, 1.00 taken at 14 K with the photon energy of $\hbar\omega = 21.22\,\text{eV}$. **Bottom**: LDA DOS of $CaVO_3$ and $SrVO_3$.

the transmission property of the electron energy analyzer was corrected and the overlapped ghost structures due to the weak satellite lines of the He discharge lamp were subtracted. Figure 5.11 (bottom) shows the LDA DOS of $CaVO_3$ and $SrVO_3$ calculated by the full-potential linear-augmented-plane-wave (FLAPW) method. We have shifted the O $2p$ bands of both $CaVO_3$ and $SrVO_3$ by 1.95 eV to the larger binding energy in order to fit well to the observed O $2p$ bands, because the LDA calculation fails to predict, in general, the value of the energy gap between the O $2p$ band and V $3d$ band. The observed UPS spectra were normalized to the maximum intensity of the O $2p$ band around 6 eV.

The agreement between the band calculation and the UPS spectrum is poor especially in the region near E_F; we can see clearly the apparent discrepancy between the observed UPS spectra and the corresponding LDA DOS by enlarging Fig. 5.11 around E_F (Fig. 5.12). Two well-distinguished structures

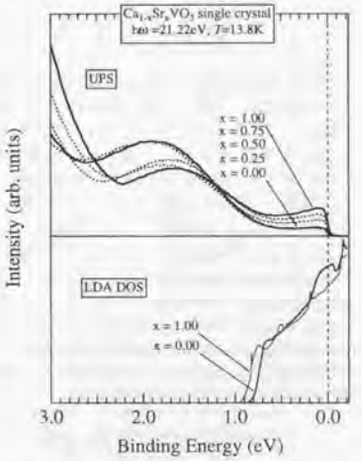

FIG. 5.12. **Top**: UPS spectra of single-crystalline $Ca_{1-x}Sr_xVO_3$ samples around E_F with $x = 0.00$, 0.25, 0.50, 0.75, 1.00 taken at 14 K with the photon energy of $\hbar\omega = 21.22\,\text{eV}$. **Bottom**: LDA DOS of $CaVO_3$ and $SrVO_3$ around E_F. UPS spectra show significant spectral weight redistribution from around E_F to $\sim 1.8\,\text{eV}$.

are seen in Fig. 5.12: one is near E_F, and the other is centered at a binding energy of

$\sim$1.7eV. This kind of spectral weight redistribution is generally ascribed to the formation of the Hubbard bands due to the strong electron correlations.[91] Furthermore, the spectral weight transfer from around E_F to the high-energy satellite is fairly systematic, as we go from $SrVO_3$ to $CaVO_3$ *i.e.*, increasing the U/W ratio. Therefore, we try to assign the spectra to the theoretical prediction given by the Hubbard model treated within the LISA method.[92]

The hamiltonian of the Hubbard model reads,

$$H = -\sum_{<i,j>}(t_{ij}+\mu)c^{\dagger}_{i\sigma}c_{j\sigma} + U\sum_i(n_{i\uparrow}-\frac{1}{2})(n_{i\downarrow}-\frac{1}{2}), \quad (5.1)$$

where summation over repeated spin indices is assumed. The LISA method is a dynamical mean field theory that is exact in the limit $q \to \infty$, where q is the connectivity of the lattice. Consequently, the hopping amplitude t_{ij} is rescaled as $t_{ij} \to \frac{t}{\sqrt{q}}$ to obtain a non-trivial model.[93] The lattice hamiltonian is then mapped onto an equivalent impurity problem which is supplemented by a self-consistency condition. The detailed derivation of the resulting mean-field equations is already given in great detail elsewhere.[92] Requiring that $G_{local}(\omega) = \Sigma_k G(k,\omega)$, the self-consistency condition becomes

$$G_0^{-1}(\omega) = \omega + E_F - t^2 G_{local}(\omega)\,. \quad (5.2)$$

We shall assume a semi-elliptical bare density of states

$$\rho^o(\omega) = \frac{8}{\pi W}\sqrt{1-\left(\frac{2\omega}{W}\right)^2}\,,$$

with $t = W/4$, which is realized in a Bethe lattice and on a fully connected fully frustrated version of the model. As there is only one $3d$-electron in the $Ca_{1-x}Sr_xVO_3$ system, we set $E_F = 0$ that renders the model half-filled. We use the second order iterated perturbation theory (IPT) calculation to solve the associated impurity problem.[92] Theoretical quasiparticle spectra at $T = 0$ and $W = 2\,eV$ for several values of U are plotted in Fig. 5.13. The spectra are obtained by the IPT approximation of the infinite dimension Hubbard model for $U = 0$, 2.4, 2.75, 2.9, and 3.2 eV. We recognize that the bare semi-elliptical DOS splits into the high-energy satellites and the quasiparticle peak at $E_F(\omega = 0)$, which becomes narrower as U increases. The narrow quasiparticle peak is the Abrikosov-Suhl (or Kondo) resonance in the impurity model language. It is important to note that $\rho(0)$ is pinned at its non-interacting value,

$$\rho(0) = \rho^o(0)\,,$$

as a result of the momentum-independent self-energy.[104] The two high-energy satellites at $\omega = \pm U/2$ are associated with the upper Hubbard band and the lower Hubbard band (empty and doubly occupied sites).

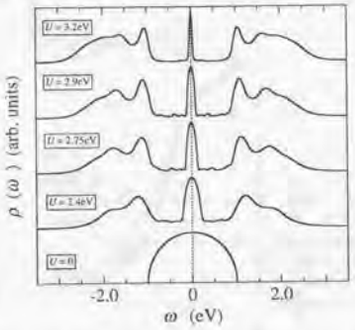

FIG. 5.13. Theoretical single-particle spectra at $T = 0$ and $W = 2\,eV$ for several values of U, *i.e.*, $U = 0$, 2.4, 2.75, 2.9, and 3.2 eV. The spectra are obtained by the IPT approximation of the infinite dimension Hubbard model. We recognize the bare semi-elliptical DOS splits into the Hubbard bands and the quasiparticle peak, which becomes narrower as U increases.

Let us now turn to the comparison between the experimental data and the theoretical predictions of the model Hamiltonian. Since this calculation was performed by M. Rozenberg at the early stage of our collaboration study,[60] the experimental photoemission data are those for polycrystalline samples with $x = 0$, 0.30, 0.40, 0.80, and 0.90 measured at $T = 80\,K$, which are reported in Ref. 59; however, there is no significant difference from the single-crystalline data except for the experimental resolution. The results are reproduced in Fig.5.14. Theoretical quasiparticle spectra of Fig. 5.14 (left) corresponds to the $\omega \le 0$ part of $\rho(\omega)$ in Fig. 5.13, *i.e.*, multiplied by the Fermi-Dirac function of 80 K and then convoluted with the total experimental resolution (a Gaussian function with the full width at the half maximum is 0.3 eV). We have subtracted a broad Gaussian function centered at $\sim 5\,eV$, that corresponds to the background contribution coming from the tail of the oxygen $2p$ band, because the description of this higher energy band is outside the scope of our present discussion.

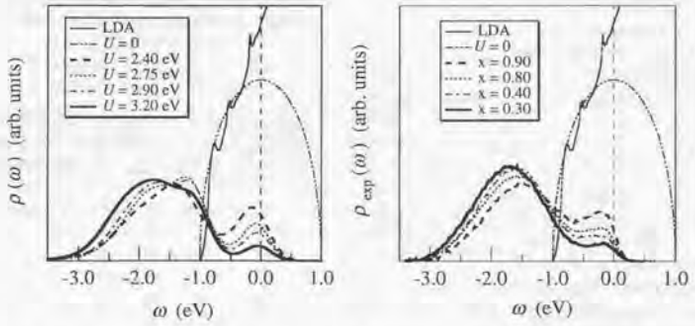

FIG. 5.14. **Left** Theoretical quasiparticle spectra at $T = 0$ and $W = 2\,eV$ for $U = 0$, 2.4, 2.75, 2.9, and 3.2 eV. The spectra are obtained by the IPT approximation of the infinite dimension Hubbard model. The data corresponds to the $\omega \le 0$ part of $\rho(\omega)$ in Fig. 5.13, *i.e.*, multiplied by the Fermi-Dirac function and then convoluted with the total experimental resolution. **Right** Experimental photoemission spectra of poly-crystalline $Ca_{1-x}Sr_xVO_3$ samples with $x = 0$, 0.30, 0.40, 0.80, and 0.90 measured at $T = 80\,K$. Background from the oxygen $2p$ band has been subtracted. In both figures, the DOS obtained by the LDA band calculation is plotted for comparison.

The lineshapes of the observed spectra are similar to those obtained from the large dimensional approach to the Hubbard model. Thus, we associate the higher frequency feature to the lower Hubbard band (LHB) and the feature at the Fermi level to the quasiparticle contribution. Moreover, as we change the value of x, *i.e.*, change the U/W ratio, we observe a systematic transfer of spectral weight, and this is apparently reproduced by the series of the theoretical spectra; we have corroborated that the observed systematic trans-

fer of the spectral weight is assigned to that between the LHB and the quasiparticle peak as a function of the interaction strength. Although we find that the basic features of the transfer of spectral weight are very well captured by the model, upon a more detailed comparison one notes that some discrepancies remain; especially, in regard of the shape of the narrow quasiparticle peak, and the lower energy edge of LHB. The latter may be due to a limitation of the IPT method to produce the exact lineshape of $\rho(\omega)$ close to the Mott-Hubbard point; this needs to be checked using a more accurate assumption for the bare (noninteracting) DOS. (This might be an intrinsic feature at the large-d limit, which, then, would be removed by the inclusion of $1/d$ corrections.) The discrepancy in the shape of the quasiparticle contribution is related to the important problem, *i.e.*, the renormalization of the value of $\rho(E_F)$. Although the intensity at E_F is well reproduced by the model calculation, this is due to the poor resolution of the experimental UPS spectra. As seen in Fig. 5.12, even in the high-resolution experiment, we cannot observe any traces of the sharp coherent peak. The peak seems to be much broader than the theoretical calculation, but the spectral weight (area of the peak) seems to be maintained as we found from the comparison in Fig. 5.14.

The ratio of the spectral weight between the LHB and the quasiparticle peak corresponds to the quasiparticle residue Z, which is the renormalization factor of the $3d$ band, while the spectral intensity at E_F ($\rho(E_F)$) multiplied by $1/Z$ is proportional to the effective mass m^*/m_b. Therefore, it is interesting to compare the effective mass deduced by this infinite-d Hubbard model calculation to that deduced from the thermodynamic or magnetic measurements which are reported in Chapter 4.

Of course, we should be note here that to explain both of the experiments consistently is a challenging problem, since the spectroscopic properties and the thermodynamical properties belong to vastly different energy scales: the former being a high energy ($0.1 \sim 1\,\mathrm{eV}$) probe, while the latter probes electrons typically within k_BT ($\sim 1\,\mathrm{meV}$) of E_F. That is like using a sledge-hammer to crack a nut. Thus, there is indeed *a-priori* no reason to believe that the same model physics will be valid in both the regimes. This is one of the most important problems in the physics of strongly correlated electron systems attracting a great deal of attention.[9,92] We hope this work can be a milestone of this attempt.

From the U/W values estimated by the comparison in Fig. 5.14, we can calculate the "thermal effective mass" (Eq. 4.6) defined as

$$\frac{m^*}{m_b} \equiv \frac{\gamma}{\gamma^{\mathrm{LDA}}} = \frac{D(E_F)}{D^{\mathrm{LDA}}(E_F)} ,$$

where $D^{\mathrm{LDA}}(E_F)$ is the density of states at E_F obtained by the LDA band calculation, and $D(E_F)$ is, in this case, defined as follows:

$$\begin{aligned} D(E_F) &= \frac{1}{Z}\rho(E_F) = \frac{1}{Z}\rho^{\circ}(E_F) \\ &= \frac{1}{Z}\left(\frac{8}{\pi W}\right) \\ &= \frac{1}{Z} \times 17.316\ (\mathrm{states/Ryd/f.u.}) . \end{aligned}$$

In this theoretical calculation, the quasiparticle residue Z is obtained as

$$Z = 0.9 \times \left(1 - \frac{1}{1.69} \times \frac{U}{W}\right) .$$

Thus, we calculate the value of m^*/m_b for each value of x. The results are listed in Table 5.III.

As described in Chapter 4, the observed m^*/m_b is around 1.5, whilst the value deduced from the large-d Hubbard model (Table 5.III) shows drastic enhancement as we decrease the value of x, *i.e.*, increase the value of U/W. We consider that the above extreme discrepancies of the effective mass may originate from

TABLE 5.III. Effective mass deduced from the comparison of the large-d Hubbard model to the measured UPS spectrum. See text in detail.

x	$D^{\mathrm{LDA}}(E_F)$ (states/Ryd/f.u.)	U (eV)	$1/Z$	m^*/m_b
0.30	26.75	3.20	20.86	13.5
0.40	26.34	2.90	7.82	5.1
0.80	24.68	2.75	5.96	4.2
0.90	24.27	2.40	3.83	2.7

the important feature that LISA is a dynamical "*mean-field*" approximation of the large-d Hubbard model.

However, here we had better lay special emphasis on the fact that **all the experimental data have been compared to those of the LDA band calculation**, as if the energy dispersion of the LDA band $\varepsilon_k^{\mathrm{LDA}}$ stood for ε_k°, which is the energy of an ideal *noninteracting* Bloch electron. Indeed the LDA band-structure calculations give a good reference for many weakly correlated materials, but the spurious self-interaction problem is actually inherent in the LDA potential as well as the problem that the exchange potential is approximated by a local "*mean-field*" potential in LDA. If we start from the LDA band calculation as a reference of the noninteracting limit, we need to compensate all the shortcomings of LDA by the so-called *self-energy correction*.

Therefore, we have drawn an inference that the apparent discrepancies shown above are **due to the ill-matched combination of LDA and LISA; both of which are kinds of mean-field approaches to the problem of electron correlations.** With respect to this corollary argument, we further propose the following assumption: **the self-energy for the proper correction to LDA should be nonlocal.** This means the self-energy, in which all the interactions are confined, should depend on the momentum $\vec{k}$. This can be satisfied to improve either LDA or LISA (as a self-energy correction to LDA); however, the improvement of either LDA or LISA is too challenging a subject to be treated here.

Although this is surely one of the most important problems in solid state physics at present, we need to keep it beyond the scope of the present discussion. However, in the following, we will introduce the $\vec{k}$-dependence phenomenologically in order to corroborate the above inference; this will eventually explain both the suppression of $\rho_{\mathrm{exp}}(E_F)$ and the pertinent value of m^*/m_b consistently.

First of all, we begin by defining a phenomenological expression of the $\vec{k}$-dependent Green's function. As described in Sec. 2.5.2, the $\vec{k}$-dependent Green's function can be generally expressed by the following continued fraction expansion (Eq. 2.7),

$$G(\omega,\vec{k}) = \frac{1}{\omega - \varepsilon_k^{\mathrm{LDA}} - \Sigma(\omega,\vec{k})} ,$$

where the self-energy of the system $\Sigma(\omega,\vec{k})$ reads

$$\Sigma(\omega,\vec{k}) = \omega_1 + \cfrac{{a_2}^2}{\omega - \omega_3 - \cfrac{{a_4}^2}{\omega - \cdots}} , \qquad (5.3)$$

and $\varepsilon_k^{\mathrm{LDA}}$ stands for the energy dispersion of a single-electron band obtained by the LDA band calculation. This expression is valid asymptotically at high energies,[32] so that this is applicable for the analysis of photoemission spectra.

The spectral DOS is obtained using the above Green's function following the relation-

ship given in the Section 2.5.1 (Eq. 2.6),

$$\rho(\omega) = -\frac{1}{\pi}\int_{-\infty}^{\infty} d\varepsilon_k^{\rm LDA} D(\varepsilon_k^{\rm LDA}) {\rm Im}G(\vec{k},\omega). \tag{5.4}$$

The calculated $\rho(\omega)$ is compared with the observed UPS spectrum $\rho_{\rm exp}(\omega)$.

On the other hand, the quasiparticle energy ε_k is given as a solution $\omega = \varepsilon_k$ of the equation

$$\omega = \varepsilon_k^{\rm LDA} + {\rm Re}\Sigma(\vec{k},\omega)\,. \tag{5.5}$$

Using the definition of DOS, *i.e.*,

$$\left|\frac{d\varepsilon_k}{d\vec{k}}\bigg|_{\vec{k}=\vec{k}_{\rm F}}\right| \equiv D(E_{\rm F})^{-1}\,,$$

and

$$\left|\frac{d\varepsilon_k^{\rm LDA}}{d\vec{k}}\bigg|_{\vec{k}=\vec{k}_{\rm F}}\right| \equiv D^{\rm LDA}(E_{\rm F})^{-1}\,,$$

the definition of the $m^*/m_{\rm b}$ (Eq. 5.3.4) is expressed as

$$\frac{m^*}{m_b} = \left|\frac{\left.\frac{d\varepsilon_k^{\rm LDA}}{d\vec{k}}\right|_{\vec{k}=\vec{k}_{\rm F}}}{\left.\frac{d\varepsilon_k}{d\vec{k}}\right|_{\vec{k}=\vec{k}_{\rm F}}}\right|\,, \tag{5.6}$$

Then, from the Eqs. 5.5 and 5.6, we deduce that the effective mass is given by the following expression:

$$\begin{aligned}\frac{m^*}{m_{\rm b}} &= \left(1 - \left.\frac{\partial {\rm Re}\Sigma(\vec{k},\omega)}{\partial\omega}\right|_{\omega=E_{\rm F}}\right) \\ &\times \left|\frac{\left.\frac{d\varepsilon_k^{\rm LDA}}{d\vec{k}}\right|_{\vec{k}=\vec{k}_{\rm F}}}{\left.\frac{d\varepsilon_k^{\rm LDA}}{d\vec{k}}\right|_{\vec{k}=\vec{k}_{\rm F}} + \left.\frac{\partial {\rm Re}\Sigma(\vec{k},\omega)}{\partial\vec{k}}\right|_{\vec{k}=\vec{k}_{\rm F}}}\right| \\ &\equiv \frac{m_\omega}{m_{\rm b}} \times \frac{m_{\rm k}}{m_{\rm b}}\,.\end{aligned} \tag{5.7}$$

This is the general expression of the "thermal effective mass"; in this expression, m_ω is called the "ω mass" and m_k is called the "k mass."[35] ω mass is equal to the reciprocal quasiparticle residue Z^{-1}. ($m_\omega/m_{\rm b}$ describes the mass enhancement at $E_{\rm F}$ due to the dynamical effects of on-site electron correlation, electron-phonon interaction, etc. $m_{\rm k}/m_{\rm b} < 1$ causes the suppression of $\rho(E_{\rm F})$ through the $\vec{k}$-dependence of the self-energy.) Thus, we deduce the spectral DOS $\rho(\omega)$ (Eq. 5.4) and the effective mass $m^*/m_{\rm b}$ (Eq. 5.7) by assuming a phenomenological self-energy (Eq. 5.3).

For simplicity, we truncate the above continued fraction expansion of $\Sigma(\omega,\vec{k})$ (Eq. 5.3) at the "modified Padé-level" $L = 3$ (see, Sec. 2.5.2 for details), *i.e.*, up to s_4, and ω_5. Under the general requirements of the self-energy near $\omega = 0$ and $\vec{k} = \vec{k}_{\rm F}$, together with the Fermi-liquid conditions, we write

$$\begin{aligned}\omega_1 &= (\alpha-1)\varepsilon_k^{\rm LDA} \\ s_2 &= \sqrt{g\Delta\Gamma} \\ \omega_3 &= -i(\Delta+\Gamma) \\ s_4 &= \sqrt{\Delta\Gamma} \\ \omega_5 &= 0\,,\end{aligned}$$

where α, g, Δ, and Γ are adjustable parameters, all of which are real and positive. We add $\vec{k}$-dependence on ω_1, leaving the other parameters $\vec{k}$-independent. The expression of ω_1 means the uniform widening of the energy bands for $\alpha > 1$. Then, we obtain

$$\begin{aligned}\Sigma(\omega,\vec{k}) &= (\alpha-1)\varepsilon_k^{\rm LDA} \\ &+ g\omega\frac{\Delta}{\omega+i\Delta}\frac{\Gamma}{\omega+i\Gamma}\,.\end{aligned} \tag{5.8}$$

Using this self-energy with four controlling parameters, we have calculated the quasiparticle spectrum $\rho(\omega)$, and compared it with the observed UPS spectra $\rho_{\rm exp}(\omega)$ of the polycrystalline $Ca_{1-x}Sr_xVO_3$ samples measured at 80 K for various values of x. The least-squares fits were performed in the quasi-particle excitation (coherent) regime ($0.5\,{\rm eV} < \omega < 0$). Adjustable parameters, α, g, Δ, and Γ in Eq. 5.8 were varied to obtain the best fit.

The parameters may be related to U and W according to the second-order perturbation

in U.[105] In $Ca_{1-x}Sr_xVO_3$, however, we have observed such a large incoherent band that we should interpret U and W as the renormalized ones $U_{\rm eff}$ and $W_{\rm eff}$: in this case,

$$\sqrt{\Delta\Gamma} \sim W_{\rm eff}$$

and

$$\frac{g\Delta\Gamma}{\Delta+\Gamma} \sim -{\rm Im}\Sigma(-W_{\rm eff},\vec{k}=\vec{k}_{\rm F})\,,$$

and g reflects $U_{\rm eff}$, since $m_\omega/m_{\rm b}$ is equal to $1+g$. The shift of the precursor of the LHB as we change the value of x will correspond to changes in $U_{\rm eff}$. The precursor of the LHB (*i.e.*, the incoherent band) cannot be reproduced by the present form of $\Sigma(\omega,\vec{k})$. However, we take into account the evolution of the incoherent band through the normalization of the spectra; *i.e.*, the relative magnitudes of the intensity of the incoherent band $I_{\rm incoh}$ to that of the coherent band $I_{\rm coh}$ is related to the ω-mass as[106]

$$\frac{m_\omega}{m_{\rm b}} \sim \frac{I_{\rm incoh}}{I_{\rm coh}} + 1\,.$$

Figure 5.15 shows the results of the analysis for $SrVO_3$ and $CaVO_3$. Open circles in the figure correspond to the 'UPS spectrum of the poly-crystalline samples measured at 80 K. The best fits of the calculated $\rho(\omega)$'s to the experimental spectra $\rho_{\rm exp}(\omega)$'s within the energy range of $0.5\,{\rm eV} < \omega < 0.3\,{\rm eV}$ are shown in Fig. 5.15 for $SrVO_3$ [curve (a3)] and $CaVO_3$ [curve (c)]. Adjustable parameters for the best fits are listed in Table 5.IV with the effective mass, ω-mass, and $\vec{k}$-mass deduced from the parameters. The deduced values of $m^*/m_{\rm b}$ are in fairly good agreement to those observed by the specific heat measurements,[46,47] magnetic susceptibilities,[46] and optical conductivities.[61]

Before we discuss the results in more detail, it is worthwhile to see how $\rho(\omega)$ depends on each parameters. First, we try to ignore the $\vec{k}$-dependence of the self-energy; *i.e.*, we put $\alpha =$

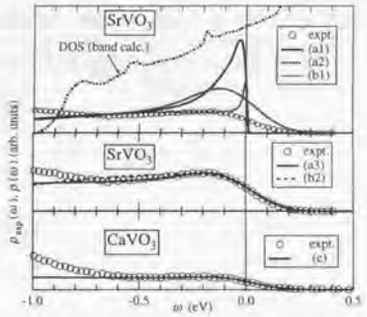

FIG. 5.15. Comparison between the LDA DOS $D(\omega)$ (dash-dotted line) for $SrVO_3$, the calculated spectral DOS $\rho(\omega)$, and the UPS spectrum (open circles) $\rho_{\rm exp}(\omega)$ for poly-crystalline $SrVO_3$ and $CaVO_3$ samples measured at 80 K. For curves (a1), (a2), and (a3), $m_\omega/m_{\rm b} \cong 4.1$ and the spectra have been multiplied by a Fermi distribution function at $T = 80$ K. See text for details.

1, which means $m_{\rm k}/m_{\rm b} = 1$. Curve (a1) shows $\rho(\omega)$ for $m_{\rm k}/m_{\rm b} = 1$ and $m^*/m_{\rm b} = m_\omega/m_{\rm b} =$ 4.1. However, (a1) is, though multiplied by a Fermi distribution function, not convoluted by a Gaussian. Then, in curve (a2), we take into account the instrumental resolution (the Gaussian is convoluted). From the curves (a1) and (a2), it is clear that a sharp coherent band in $\rho(\omega)$ due to a mass enhancement of $m_\omega/m_{\rm b} = 4.1$ can not be suppressed sufficiently by the instrumental broadening, so that we can not fit the experimental spectrum.

Therefore, we switch on the $\vec{k}$-dependence of the self-energy. we take $m_{\rm k}/m_{\rm b} =$ 0.32, which reduces the effective mass from $m^*/m_{\rm b} = m_\omega/m_{\rm b} = 4.1$ to $m^*/m_{\rm b} = 1.3$, and the calculated $\rho(\omega)$ fits well to the experimental spectrum [curve (a3)].

As we demonstrated by comparison with the large-d Hubbard model, we can obtain an alternative fit without introducing the $\vec{k}$-dependence of the self-energy, as depicted by

TABLE 5.IV. Adjustable parameters for the best fits of the calculated $\rho(\omega)$'s to the experimental spectra $\rho_{exp}(\omega)$'s within the energy range of $0.5\,eV < \omega < 0.3\,eV$. The $\rho(\omega)$'s obtained using these parameters are shown in Fig. 5.15 [curve (a3) for $SrVO_3$ and curve (c) for $CaVO_3$]. Deduced effective mass, ω-mass, and $\vec{k}$-mass are also listed.

	α	g	Δ (eV)	Γ (eV)	m_k/m_b	m_ω/m_b	m^*/m_b
$SrVO_3$ (a3)	3.2	3.1	12	0.31	0.30	4.1	1.3
$CaVO_3$ (c)	7.1	19	8.0	0.08	0.13	19	2.6

curves (b1) and (b2) for $SrVO_3$ in Fig. 5.15. However, we need to assume a large ω-mass to obtain a sufficient fit. For curves (b1) and (b2), $m_k/m_b = 1$, $m^*/m_b = m_\omega/m_b = 45$. The extremely sharp peak at E_F is obscured by the instrumental broadening. Although the result of this fit seems to be acceptable, it is difficult to explain the strong discrepancy between the value of $m^*/m_b = 45$ in this fit and $m^*/m_b \sim 1.5$ deduced from the other experiments. Thus we have corroborated again that $\vec{k}$-dependence of the self-energy is necessary both to fit the observed spectral DOS and to explain the value of the effective mass consistently.

Let us now estimate the U/W values using the parameters for the best fits. $U/2$ corresponds to the energy of the incoherent peak ($\sim$1.6 eV for $SrVO_3$ and $\sim$1.7 eV for $CaVO_3$). The half band width

$$\frac{W}{2} \sim \frac{m^*}{m_b}\frac{W_{eff}}{2}$$

is $\sim$1.3 eV for $SrVO_3$ and $\sim$1.0 eV for $CaVO_3$, which are comparable to those of the LDA calculation. Accordingly, the U/W value becomes[107]

$$U/W = \begin{cases} \sim 1.2 & \text{for } SrVO_3 \\ \sim 1.7 & \text{for } CaVO_3 \end{cases}.$$

In Fig. 5.16, curves (a) and (c) show $\Sigma(\omega) \equiv \Sigma(\omega, \vec{k} = \vec{k}_F)$ for $SrVO_3$ [corresponding to (a1), (a2) and (a3) in Fig. 5.15] and $CaVO_3$ [(c) in Fig. 5.15], respectively, plotted against

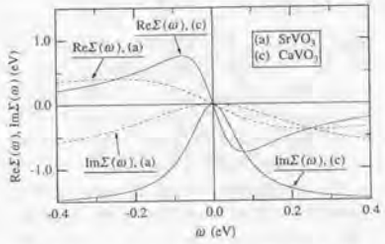

FIG. 5.16. Self-energies at the Fermi surface $\Sigma(\omega) \equiv \Sigma(\omega, \vec{k} = \vec{k}_F)$ as a function of the quasiparticle excitation energy ω. The self-energy (a) for $SrVO_3$ is used to reproduce (a1), (a2) and (a3) in Fig. 5.15, and the self-energy (c) is for $CaVO_3$.

the quasiparticle excitation energy ω. It is obvious from the figure that $\Sigma(\omega)$ behaves as $\Sigma(\omega) \sim -a\omega - ib\omega^2$ in the region near E_F. This region becomes narrower in going from $SrVO_3$ to $CaVO_3$ representing the narrowing of the coherent band with increasing U/W.

Let us now attempt to extend the above trial for $CaVO_3$ and $SrVO_3$ to the other UPS spectra of the poly-crystalline $Ca_{1-x}Sr_xVO_3$ samples with various x. The results are summarized in Fig 5.17. The figure shows that as x decreases, m_ω/m_b increases almost monotonically up to $\sim$ 20. This corresponds to the large spectral weight redistribution as the value of U/W increases. Nevertheless, the effective mass m^*/m_b is not so much enhanced, because of the decrease in m_k/m_b with decreasing the value of x. In $CaVO_3$ the effective mass m^*/m_b is thus not so large, although

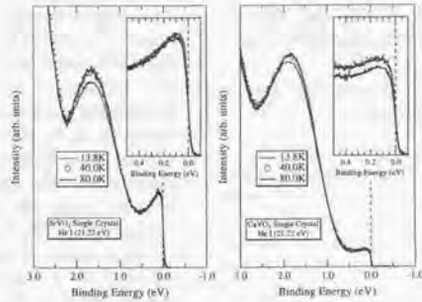

FIG. 5.18. UPS spectra of single-crystalline $SrVO_3$ (left) and $CaVO_3$ (right) measured at T = 13.8, 40.0, and 80.0 K.

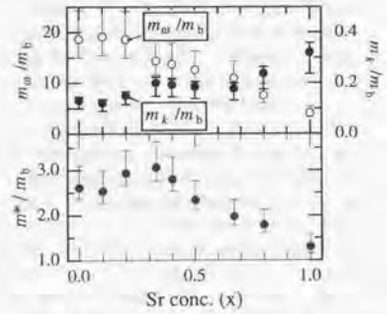

FIG. 5.17. Effective masses deduced from the UPS spectra of $Ca_{1-x}Sr_xVO_3$. As x decreases, m_ω/m_b shows a fairly large enhancement (top). Nevertheless, the effective mass m^*/m_b is not as enhanced as m_ω/m_b (bottom), because of the decrease in m_k/m_b.

the spectral weight redistribution is very large.

Viewed in this light, we have now been able to corroborate the significant inference made on page 69; *i.e.*, **$\vec{k}$-dependence of the self-energy is necessary for the proper correction to LDA**. The $\vec{k}$-dependence of the self-energy may work to compensate the self-interaction problem inherent in the LDA potential. Moreover, we consider the exchange potential, which is approximated by the local "*mean-field*" potential in LDA, is also compensated in this $\vec{k}$-dependence of the self-energy. This strong $\vec{k}$-dependence is not necessary to be considered in conventional metals. Therefore, it seems reasonable to advocate that, in the vicinity of a Mott transition, nonlocal interactions, which are not treated sufficiently in LDA as well as LISA, become fairly important. The long-range interaction includes electron-optical-phonon interaction, spin fluctuations, and electron-electron interaction through the long-range Coulomb and exchange interaction. The microscopic nature of the nonlocal interaction remains to be clarified in future experimental and theoretical studies.

It may be worth pointing out, in passing, that the coherent part of the observed UPS spectrum does not show any significant temperature dependences. Figure 5.18 shows the UPS spectra of single-crystalline $SrVO_3$ and $CaVO_3$ measured at T = 13.8, 40.0, and 80.0 K. If the coherent peak is so sharp as to be merely smeared out by the experimental resolution, it must show a large temperature dependence. However, such a large tempera-

ture dependence was not observed, thus confirming the validity of the discussion above.

5.3.5. New attempt to decompose the surface and bulk contributions

With all the consistent discussion in the previous sections, it has been questioned that the electronic structure of $Ca_{1-x}Sr_xVO_3$ at the surface might be different from that in the bulk, and this might be a reason for the large peak at ~ 1.7 eV. From this point of view, K. Maiti and D.D. Sarma in IISc proposed a reexamination of the photoemission spectra of $Ca_{1-x}Sr_xVO_3$ system along with their state-of-the-art analysis method of photoemission spectroscopy,[28] *i.e.*, the decomposition of the surface contribution and bulk contribution. This study was thus performed as a collaboration between ETL and IIS.

We describe here the preliminary data, which eventually corroborated the basic argument in Sec. 5.3.4, though the parameters used previously need to be modified somehow.

In order to separate the surface and bulk contributions, we first note that the total spectrum $\rho(\omega)$ at any given photon energy is given[28] in terms of the surface spectrum, $\rho^s(\omega)$ and the bulk spectrum, $\rho^b(\omega)$, by

$$\rho(\omega) = (1 - e^{-d/\omega})\rho^s(\omega) + e^{-d/\omega}\rho^b(\omega)\,, \tag{5.9}$$

where d is the thickness of the surface layer with the altered electronic structure compared to the bulk and λ is the penetration depth of electrons. Thus, the intensity ratio of the surface and the bulk contributions in any spectrum is $(1 - e^{-d/\lambda})/e^{-d/\lambda} = e^{d/\lambda} - 1$.

The intensity contributions from the surface and the bulk is determined from the V $2p_{3/2}$ spectrum, assuming that the peaks "b", "a" and "c" in Fig. 5.5 in Sec. 5.3.2 arise from V^{3+}, V^{4+} and V^{5+} entities, and the V^{3+} and V^{5+} components are coming from the surface electronic state. This yields a value of (d/λ) for V $2p$ electrons with a kinetic energy of about 950 eV. (Note that, in the experiment at IISc, we used Al Kα radiation, by which a photoelectron from E_F has kinetic energy of ~ 1480 eV, instead of Mg Kα radiation.) Since, λ is known[29] to be proportional to the square root of the photoelectron kinetic energy in the higher energy limit, we can estimate the corresponding d/λ for the valence band (VB) electrons by multiplying the d/λ obtained for the V $2p$ electrons with $\sqrt{950/1480}$ in the case of each composition. Thus, we obtain d/λ for the VB spectrum with Al $K\alpha$ radiation to be 0.49, 0.53, 0.57 and 0.47 for $x = 0.0$, 0.2, 0.7 and 1.0 respectively in $Ca_{1-x}Sr_xVO_3$ series.

We also need to estimate the same quantity for the VB spectrum excited with He I radiation, $d/\lambda_{\mathrm{He\,I}}$. Unfortunately there is no universally accepted dependence of λ on kinetic energy in the lower energy limit, unlike the higher energy limit. In view of this, we assume that the $\lambda_{\mathrm{XPS}}/\lambda_{\mathrm{He\,I}}$ in $Ca_{1-x}Sr_xVO_3$ is the same as in the closely related series $Ca_{1-x}La_xVO_3$, where it was experimentally estimated[28]

$$\lambda_{\mathrm{XPS}}/\lambda_{\mathrm{He\,I}} = 3.4\,.$$

Therefore, we obtain $d/\lambda_{\mathrm{He\,I}}$ to be 1.67, 1.81, 1.95 and 1.61 for $x = 0.0$, 0.2, 0.7 and 1.0 respectively.

Then, Eq. 5.9 becomes two simultaneous equations for each energy point ω,

$$\begin{aligned}
\rho_{\mathrm{XPS}}(\omega) &= (1 - e^{-d/\lambda_{\mathrm{XPS}}})\rho^s(\omega) + e^{-d/\lambda_{\mathrm{XPS}}}\rho^b(\omega) \\
\rho_{\mathrm{He\,I}}(\omega) &= (1 - e^{-d/\lambda_{\mathrm{He\,I}}})\rho^s(\omega) + e^{-d/\lambda_{\mathrm{He\,I}}}\rho^b(\omega)\,.
\end{aligned}$$

Since we measure $\rho_{\mathrm{XPS}}(\omega)$ and $\rho_{\mathrm{He\,I}}(\omega)$ at every energy point ω, the above two equations can be solved exactly for the two unknowns $\rho^s(\omega)$ and $\rho^b(\omega)$.

In this procedure, the most uncertain step has been to transfer $\lambda_{\mathrm{XPS}}/\lambda_{\mathrm{He\,I}}$ value from the $Ca_{1-x}La_xVO_3$ series to the present case of $Ca_{1-x}Sr_xVO_3$, while all other quantities, $\rho_{\mathrm{XPS}}(\omega)$, $\rho_{\mathrm{He\,I}}(\omega)$, etc. are directly obtained from experimental results. Fortunately, the final results for ρ^b and ρ^s are not very sensitive to this particular choice of $\lambda_{\mathrm{XPS}}/\lambda_{\mathrm{He\,I}}$; we have checked this explicitly by extracting ρ^b and ρ^s for a wide range of $\lambda_{\mathrm{XPS}}/\lambda_{\mathrm{He\,I}}$ between 3.0 and 4.5. Outside this range of values, the extracted ρ^b and ρ^s develop negative intensities which are clearly unphysical. Therefore, this method of extracting the spectral functions for the bulk and the surface appears to provide stable and meaningful solutions with relatively small uncertainties.

It is clear that the approach here is general enough and therefore, can be applied to a wide range of cases allowing a reliable separation of the surface and bulk related electronic structures.

We show the surface and bulk contributions ($\rho^s(\omega)$ and $\rho^b(\omega)$, respectively) to the photoemission VB spectra for $CaVO_3$ in Fig. 5.19, and for $SrVO_3$ in Fig. 5.20. The surface spectra (filled circles in Figs. 5.19 and 5.20) are invariably dominated by the incoherent features. First we note that the surface of this series has essentially V^{3+} and V^{5+} like species arising from a charge disproportionation $2V^{4+} \rightarrow V^{3+} + V^{5+}$. V^{5+} has $3d^0$ electronic configuration and therefore does not contribute any photoemission signal over the energy range of Figs. 5.19 and 5.20. This means that the surface spectra shown in Figs. 5.19 and 5.20 arise entirely from V^{3+}-like species at the surface. Interestingly, the surface V^{3+} spectral function of $CaVO_3$ has virtually no intensity at E_F suggesting an insulating state, while the surface spectrum for $SrVO_3$ has a finite spec-

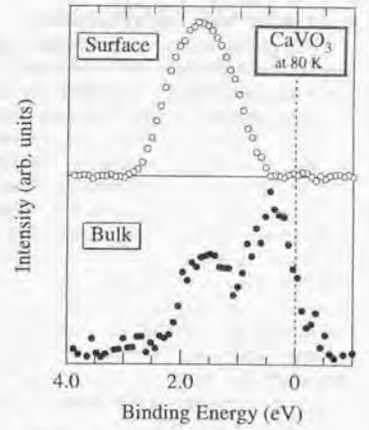

FIG. 5.19. Surface and bulk contributions to the photoemission VB spectra of single-crystalline $CaVO_3$ sample at 80.0 K. See text for details.

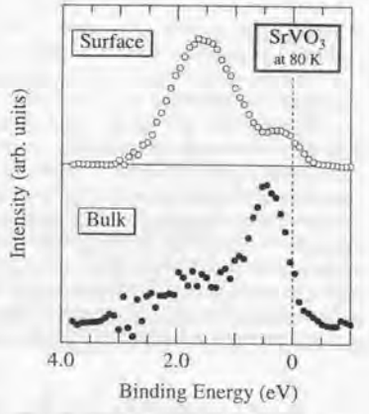

FIG. 5.20. Surface and bulk contributions to the photoemission VB spectra of single-crystalline $SrVO_3$ sample at 80.0 K. See text for details.

tral intensity at E_F signifying a metal.

Thus, we found that a metal-insulator transition occurs between $SrVO_3$ and $CaVO_3$ at the surface, while the bulk electronic structure remains metallic. The reduced atomic coordination number at the surface, along with the fact that half of the sites at the surface are V^{5+}, leads to a decrease of near-neighbor hoppings as well as to a decrease of the effective screening, giving rise a decrease in W and an increase in the strength of U compared to the bulk; consequently, there is a remarkable increase in the correlation strength, U/W, at the surface compared to the bulk. This, in spectroscopic terms, enhances the intensity of the incoherent feature; but more fundamentally, this enhanced correlation at the surface is the driving force for the charge disproportionation ($2V^{4+} \rightarrow V^{3+} + V^{5+}$) at the surface in contrast to the bulk. Systems with such charge disproportionation may be modeled with a "negative effective U" scenario. Such disproportionation, or more generally, a phase separation has indeed been suggested as a possibility for very strongly correlated systems. This is the first experimental realization of this phenomenon induced by the presence of extreme correlations that arise due to the reduced dimensionality at the surface.

Although this method is still preliminary as due to an insufficient resolution, naive hypotheses, and arbitrariness for choosing parameters, this measurement has cast a question that the discussion in the previous section might be completely wrong as influenced by the surface contribution. Since we know that it is the most preferable attitude at this stage to recognize that the *valid argument* can only be done on the common results extracted from both the ordinary and this brand-new experiments, in view of this, let us examine in this section the *bulk* spectrum in more detail and try to extract the common properties.

As clearly seen, a large proportion of the incoherent part might be due to the surface contribution, however, there still remains a significant amount of the incoherent contribution. Therefore, we try to assign the spectrum again to the theoretical prediction given by the Hubbard model treated within the LISA method.[92]

We have used a half-filled semi-elliptical DOS $D^{\rm se}(\omega)$ for the non-interacting limit ($U = 0$) of the calculation. In Fig. 5.21 (top), we have plotted LDA DOS, the semi-elliptical DOS with the band-width $W = 1.4\,\mathrm{eV}$, and the DOS of free-electrons with the band mass m_b of $1.54m_o$, where m_o is the bare electron mass. The free-electron DOS is expressed as

$$D(\omega) = \frac{3}{2\varepsilon_F}\sqrt{1+\frac{\omega}{\varepsilon_F}}\,,$$

and the Fermi energy ε_F is defined as

$$\varepsilon_F = \frac{1}{2}\left(\frac{\pi^2\hbar^3}{V}\frac{1}{d}\right)^{2/3}\frac{1}{m_b}\,,$$

where V is the volume of the unit formula of $CaVO_3$, and d is the number of the band degeneracy which is set to 3 in this case. This means that $D(0)$ is proportional to both m_b and $d^{2/3}$. The band mass $m_{\rm se}$ of the semi-elliptical DOS is defined as $m_{\rm se}$ as

$$\frac{m_{\rm se}}{m_o} \equiv \frac{D(0)\text{ of semi-elliptical DOS}}{D(0)\text{ of free-electron DOS with } m_b = m_o} = \frac{8\varepsilon_F}{3\pi D}\,.$$

As is apparent from Fig. 5.21 (top), the occupied part of LDA DOS looks similar to the DOS of the free-electron with $m_b = 1.54m_o$. This means, in a sense, that LDA can be an appropriate substitute for the "non-interacting DOS", to which we apply electron correlations by the self-energy correction. But, as we discussed above, this is not true, especially under the presence of the strong electron correlations.

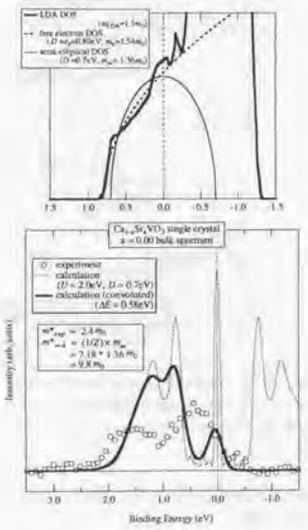

FIG. 5.21. **Top**: LDA DOS of $CaVO_3$ plotted with the semi-elliptical DOS with $W = 1.4\,\mathrm{eV}$, which is the $U = 0$ limit of the large-d Hubbard model calculation using the LISA method, and the DOS of the free-electron with $m_b = 1.54m_o$ for comparison. **Bottom**: Bulk contribution to the photoemission spectrum of $CaVO_3$ at 80 K (open circles), calculated spectral DOS for $U = 2.0\,\mathrm{eV}$ and $D = W/2 = 0.7\,\mathrm{eV}$ (solid line), which is obtained by multiplying the Fermi-Dirac function and a Gaussian convolution to the raw theoretical DOS (dashed line). The resolution (full-width at the half-maximum of the Gaussian) is 0.58 eV.

Meanwhile, the semi-elliptical DOS with $W = 1.4\,\mathrm{eV}$ captures the band-width of the occupied part and the intensity at $\omega = 0$. Given that this semi-elliptical DOS is a reasonable substitute for the $U = 0$ limit of this $CaVO_3$ system, M. J. Rozenberg has calculated, in collaboration, the spectral DOS by the large-d Hubbard model treated within the LISA method. The result is depicted in the bottom of Fig. 5.21; we cannot reproduce the experimental spectrum at all. This result indicates that it is impossible, without changing this small value of W, to fit the experimental data sufficiently. Moreover, the effective mass deduced from this calculation,

$$\frac{m^*_{\infty-d}}{m_o} \equiv \frac{1}{Z}\times\frac{m_{\rm se}}{m_o} \cong 9.8\,,$$

becomes extremely large, and is inconsistent with the value,

$$\frac{m^*_{\rm exp}}{m_o} \cong 2.4\,,$$

deduced from the Pauli paramagnetic susceptibility and the electronic specific heat coefficient.[46]

Then, we have varied both U and W as fitting parameters. Figure 5.22 shows a result of the fitting, in which U is taken to be 2.0 eV and W is 2.4 eV. This value of W is much larger than that of LDA DOS as clearly demonstrated in Figure 5.22 (top). The semi-elliptical DOS with $W = 2.4\,\mathrm{eV}$ is broader than LDA DOS and, thus, there is a significant depletion of the intensity at $\omega = 0$. Using these parameters, we can fit the bulk contribution fairly well. Moreover, the effective mass is

$$\frac{m^*}{m_o} = \frac{1}{Z}\times\frac{m_{\rm se}}{m_o} = 2.2\times 0.79 = 1.7\,,$$

which is not so different from the experiment value. The remaining discrepancy can be

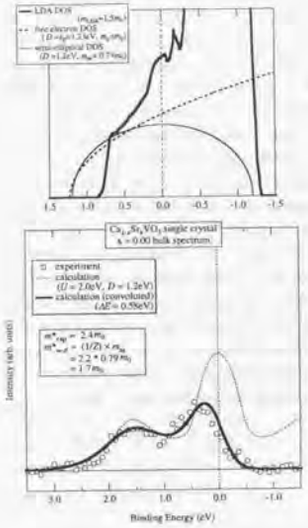

FIG. 5.22. **Top**: LDA DOS of $CaVO_3$ plotted with the semi-elliptical DOS with $W = 2.4\,\mathrm{eV}$, which is the $U = 0$ limit of the large-d Hubbard model calculation using the LISA method, and the DOS of the free-electron with $m_b = m_o$ for comparison. **Bottom**: Bulk contribution to the photoemission spectrum of $CaVO_3$ at 80 K (open circles), calculated spectral DOS for $U = 2.0\,\mathrm{eV}$ and $D = W/2 = 1.2\,\mathrm{eV}$ (solid line), which is obtained by multiplying the Fermi-Dirac function and a Gaussian convolution to the raw theoretical DOS (dashed line). The resolution (full-width at the half-maximum of the Gaussian) is 0.58 eV.

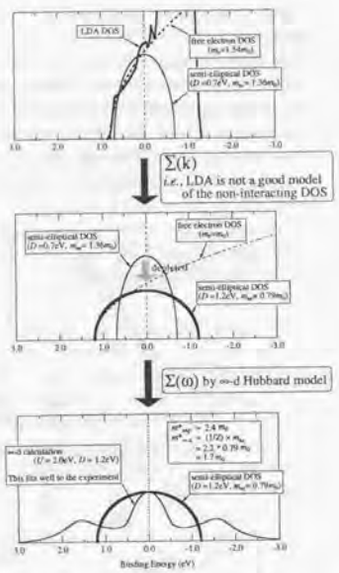

FIG. 5.23. Schematic picture describing how we can obtain appropriate theoretical $\rho(\omega)$ from LDA DOS by the self-energy correction.

somewhat explained by considering the band degeneracy d; $D(0) \propto d^{2/3} = 2.08$ for $d = 3$, and $d^{2/3} = 1.59$ for $d = 2$. (In $CaVO_3$, the t_{2g} band is not completely 3-fold degenerate.)

Thus, we have corroborated again that a large depletion of the intensity at $\omega = 0$ is necessary to explain both the shape of the spectrum and the value of the effective mass consistently. This is depicted schematically in Fig. 5.23.

For comparison, here we try to fit the bulk spectra by the self-energy correction of the LDA DOS with the k-dependent phenomenological self-energy of Eqn. 5.8. The least-squares fits were performed in the quasiparticle excitation (coherent) regime ($0.5\,\mathrm{eV} < \omega < 0$). Adjustable parameters, α, g, Δ, and Γ in Eq. 5.8 were varied to obtain the best fit.

Figure 5.24 and 5.25 shows the results of the analysis for $SrVO_3$ and $CaVO_3$, respectively. Adjustable parameters for the best fits are listed in Table 5.V with the effective mass, ω-mass, and $\vec{k}$-mass deduced from the

TABLE 5.V. Adjustable parameters for the best fits of the calculated $\rho(\omega)$'s to the bulk spectra of $SrVO_3$ and $CaVO_3$ within the energy range of $0.5\,\mathrm{eV} < \omega < 0.3\,\mathrm{eV}$. Deduced effective mass, ω-mass, and $\vec{k}$-mass are also listed. (SC stands for the self-energy correction.) The effective masses obtained by the large-d Hubbard model calculation using LISA are also listed for comparison. The $\vec{k}$-mass of the latter m_k/m_b corresponds to m_{ac}/m_b, where m_b is the LDA band mass.

	α	g	Δ (eV)	Γ (eV)	m_k/m_b	m_ω/m_b	m^*/m_b
$SrVO_3$ (SC)	1.87	1.52	65.4	0.038	0.54	2.5	1.4
$SrVO_3$ (LISA)					0.48	1.8	0.88
$CaVO_3$ (SC)	2.54	2.92	114.8	0.013	0.39	3.9	1.5
$CaVO_3$ (LISA)					0.52	2.2	1.1

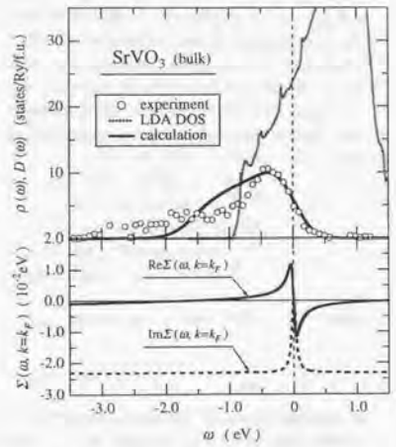

FIG. 5.24. **Top**: Comparison between the LDA DOS (dashed line), the calculated spectral DOS (solid line), and the bulk spectrum (open circles) for $SrVO_3$. For the calculation, $m_\omega/m_b \cong 1.35$ and the spectra have been multiplied by a Fermi distribution function at $T = 80\,\mathrm{K}$. **Bottom**: Self-energies at the Fermi surface $\Sigma(\omega) \equiv \Sigma(\omega, \vec{k} = \vec{k}_F)$ as a function of the quasiparticle excitation energy ω.

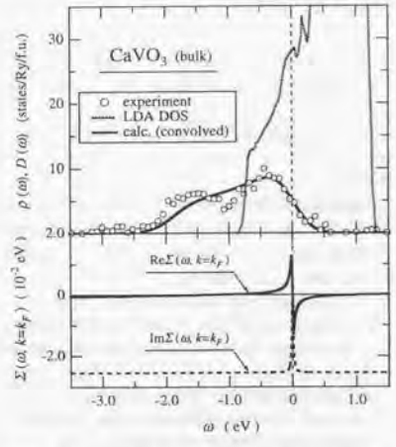

FIG. 5.25. **Top**: Comparison between the LDA DOS (dashed line), the calculated spectral DOS (solid line), and the bulk spectrum (open circles) for $CaVO_3$. For the calculation, $m_\omega/m_b \cong 1.54$ and the spectra have been multiplied by a Fermi distribution function at $T = 80\,\mathrm{K}$. **Bottom**: Self-energies at the Fermi surface $\Sigma(\omega) \equiv \Sigma(\omega, \vec{k} = \vec{k}_F)$ as a function of the quasiparticle excitation energy ω.

parameters. The effective masses obtained by the large-d Hubbard model calculation using LISA are also listed in the table for comparison. The $\vec{k}$-mass of the latter m_k/m_b corresponds to m_{sc}/m_b, where m_b is the LDA band mass.

We can estimate the U/W values using the parameters for the best fits. $U/2$ corresponds to the energy of the incoherent peak ($\sim$1.5 eV for both $SrVO_3$ and $CaVO_3$). The half band width

$$\frac{W}{2} \sim \frac{m^*}{m_b}\frac{W_{\rm eff}}{2}$$

is $\sim$1.6 eV for $SrVO_3$ and $\sim$1.4 eV for $CaVO_3$. Accordingly, the U/W value becomes[107]

$$U/W = \begin{cases} \sim 0.94 & \text{for } SrVO_3 \\ \sim 1.1 & \text{for } CaVO_3 \end{cases} .$$

For the bulk spectra of $SrVO_3$ and $CaVO_3$, the results of LISA with broad bare DOS and the k-dependent self-energy correction of LDA are not much different.

Thus, we have extracted the common property from both the ordinary UPS experiments described in the previous section, and the newborn method in this section. The important consensus is that LDA overestimates $D(E_F)$ as well as underestimates the bare bandwidth compared to LISA. This discrepancy between LDA DOS and bare DOS of DMFT in terms of the bandwidth and the $D(E_F)$ was indeed the basis for invoking the nonlocal self-energy. One obvious implication of our results is that the DOS obtained from LDA cannot be interpreted as the bare non-interacting DOS, required as an input to the *mean-field*-type many-body formalism.

As we have described repeatedly in this chapter, the necessity to consider the $\vec{k}$-dependence to the self-energy is attributed to the fact that neither LDA nor LISA can capture the nonlocal interaction properly, which may be significant near the Mott transition. Let us consider this issue more concretely. For the free-electron gas, the LDA calculation gives a band-structure which is almost identical to that of the non-interacting electrons

$$\varepsilon(k) = \frac{\hbar^2 k^2}{2m_o} .$$

However, in LDA, the exchange potential is approximated by a local potential, and, thus, k-dependence of the self-energy is forced to be substantially different from zero. On the other hand, the Hartree-Fock approximation (HFA), for example, can properly deal with the non-locality of the exchange interaction. Therefore, it gives us a good estimation how much significant the k-dependence is, as we compare HFA to LDA. For the free-electron gas, HFA gives a one-electron energy dispersion

$$\varepsilon(k) = \frac{\hbar^2 k^2}{2m_o} - \frac{2e^2}{\pi}k_F\left(\frac{1}{2} + \frac{1-x^2}{4x}\ln\left|\frac{1+x}{1-x}\right|\right) ,$$

where $x \equiv k/k_F$. Since LDA gives

$$\varepsilon(k) = \frac{\hbar^2 k^2}{2m_o} ,$$

if we start from LDA, the "occupied" bandwidth has to be increased by $\sim \frac{2e^2}{\pi}k_F$ due to the effect of the non-local exchange interaction.[62]

The screening effect, which is neglected in HFA, reduces this effect to some extent. We think when the system is close to a metal-to-insulator transition boundary, carriers can no more afford to screen long-range electron-electron Coulomb interaction sufficiently and the electric polarization of constituent ions becomes important. This can be realized in most of the transition metal oxides, because the density of carriers are significantly smaller in these metallic oxides than that of conventional metals. Morikawa *et al.*, has actually

calculated for $CaVO_3$ that, when the long-range Coulomb interaction is screened by the electric polarization of constituent ions ($\varepsilon_\infty \simeq 3 \sim 5$ eV), the band widening of the "occupied part" becomes $\sim$ 0.5 eV.[62] This seems to be fairly consistent with our result seen in Fig. 5.22 (top).

Furthermore, the spin/orbital fluctuations, from which the nonlocal self-energy may also originate, can be enhanced near the Mott transition boundary. These effect can, in some cases, induce the long range order concomitant with MIT.

In short, the k-dependence of the self-energy should be taken into account, **when we analyze photoemission spectra based on the LDA band structure.** However, it is difficult to estimate the "real" k-dependence of the self-energy, which cannot be measured by any other electronic measurements. This is because, by the name of "k-dependence", we have to compensate the self-interaction effect of the LDA potential, as well as the other shortcomings inherent to the model physics, such as the lack of degeneracy in the large-d Hubbard model.

5.3.6. Summary

In this chapter, we have shown several results of the high-energy spectroscopies, such as XPS, XAS, and UPS, for the perovskite-type $3d^1$ metallic system $Ca_{1-x}Sr_xVO_3$.

The core-level XPS has revealed that the V 2p and O 1s spectra consist of three peaks even in the end members $CaVO_3$ and $SrVO_3$. We believe that this can be attributed to the intrinsic surface electronic states, wherein charge disproportionation ($2V^{4+} \rightarrow V^{3+} + V^{5+}$) may occur.

Both the O 1s edge and V 2p edge XAS spectra cannot be explained by either the cluster model calculations or the LDA band calculations. The spectra may be understood by the overlapping surface contribution, or rather it might be explained by the formation of the Hubbard bands due to the strong correlations.

UPS spectra $\rho_{\rm exp}(\omega)$ were completely different from LDA DOS, showing a systematic spectral weight transfer as we change the value of x. $\rho_{\rm exp}(\omega)$ consists of two well-defined features: one is the coherent spectral weight at E_F corresponding to the quasiparticle excitations, and the other is the high energy excitations $\sim$1.7 eV signaling the formation of LHB. As we increase the magnitude of U/W, *i.e.*, increase the value of x, a large amount of the spectral weight is transferred from the coherent band to the precursor of LHB.

Complementarily, we have performed a state-of-the-art analysis of photoemission spectroscopy to separate out the surface and bulk contributions from the total spectrum. This has revealed a novel MI transition caused by charge disproportionation at the surface, which has never been observed in other materials. This MI transition is only realized at the surface with a change of x, while the bulk remains metallic.

We have compared the spectra of ordinary UPS experiments and the bulk spectra of the newborn measurement, and have tried to extract the common properties. We calculated a spectral DOS using the large-d Hubbard model within the LISA method, as well as a phenomenological introduction of the self-energy correction to the LDA DOS based on the Fermi-liquid picture. The suppression of $\rho(E_F)$, which was seen in both the ordinary UPS and the new bulk spectra, has indicated that some correction to the local single-particle self-energy is necessary to reproduce the observed UPS spectra; this means that the DOS obtained from LDA cannot be interpreted as the bare non-interacting DOS, required as an input to the mean-field many-body formalism. Thus, by tentatively squashing all the unknown interactions, which might be omitted in either LDA or LISA, into the $\vec{k}$-dependence of the self-energy phenomeno-

logically, we could obtain reasonable values of m^*/m_b as well as the reasonable fit to the experimental spectra.

It is difficult to estimate the intrinsic $\vec{k}$-dependent contribution to the self-energy, because the self-interaction effect of the LDA potential and the other shortcomings inherent to the model physics may compensate or enhance the apparent contribution of the $\vec{k}$-dependence. More elaborate experimental studies are expected to reveal the nature of the nonlocal interaction, which becomes significant near the Mott transition.

Chapter 6

Photoemission Study of the Layered 4*d*-Electron Superconductor Sr_2RuO_4

Part of this chapter has been published as Ref. 108, Ref. 109, and Ref. 110

6.1. Introduction

It has taken almost eight years after the discovery of the high T_c cuprate superconductor for another layered-perovskite superconductor to be found. Maeno *et al.* have discovered the superconductivity of the layered-perovskite Sr_2RuO_4 with the same crystal structure as that of $La_{2-x}Ba_xCuO_4$.[111] Sr_2RuO_4 exhibited superconductivity at $T_c = 0.93\,K$ [112] and recently $T_c = 1.50\,K$ was reported.[113]

As well as the origin of the interesting superconductivity, normal state electronic properties of Sr_2RuO_4 are particularly interesting to be investigated. Highly anisotropic, quasi-two-dimensional Fermi-liquid behavior at low temperature ($< 25\,K$), dominated by the network of RuO_2 planes, have been reported so far.[114–117] The out-of-plane resistivity is different by a factor of 850 from the in-plane resistivity;[114] both resistivities vary as T^2 with high accuracy below 25 K. The out-of-plane resistivity shows a maximum around 130 K, above which it becomes incoherent (semi-conducting), whilst the in-plane resistivity increases with a large linear component superimposed on the T^2 term. This crossover of the transport properties from 3-dimensional to quasi-2-dimensional at $\sim 130\,K$ is achieved once the thermal distribution of the quasiparticle energy due to the phonon scattering becomes comparable to the transfer integral (effective bandwidth) along the c-axis, making the out-of-plane transport diffusive.[114,115] The in-plane magnetoresistance is positive and large, and decreases as we increase the temperature.[118] The out-of-plane magnetoresistance depends on the magnetic field linearly and becomes negative above 75 K, while the in-plane magnetoresistance remains positive.[118] Furthermore, the temperature dependence of the Hall coefficient is intriguing. It is negative below 30 K, changes sign at that temperature, and again returns to a negative value above 130 K.[116,119]

It has been pointed out that Sr_2RuO_4 must be close to a ferromagnetic instability,[120,121] because the 3-dimensional analog of this material, $SrRuO_3$, is a ferromagnetic metal. Since ferromagnetic fluctuations eliminate the even-parity pairing channels for superconductivity, such as *s*-wave and *d*-wave pairing, it has been suggested that superconductivity in Sr_2RuO_4 should be accompanied by the triplet (*p*-wave) odd-parity pairing.[120,122–126] This scenario is supported by several experiments:

1. The lack of a Hebel-Slichter peak in $1/T_1$ in the nuclear quadrupole resonance (NQR) measurement,[127]
2. About half of the normal-state density

of states (DOS) remain in the superconducting phase, as observed by the specific heat[128] and NQR[127] measurements.

3. Nonmagnetic impurities destroy the superconductivity when the mean free path of carriers becomes smaller than the superconducting coherence length.[113]

4. The critical temperature T_c decreases drastically under pressure.[129]

5. The superconducting coherence length in the *ab*-plane is 26 times as large as that along the *c*-axis.[130]

6. Spontaneous appearance of an internal magnetic field below T_c was observed by muon spin-relaxation measurements; this means the superconducting state violates the time-reversal symmetry.[131]

In order to understand the nature of the superconductivity, as well as the interesting normal state properties, direct observations of the electronic states are prerequisite. The de Haas – van Alphen (dHvA) experiment has shown three Fermi surfaces with two-dimensional topology,[117] which agrees well with the band calculation with local-density approximation (LDA).[132–134] However, the angle-resolved photoemission (ARPES) experiments have shown topologically different Fermi surfaces.[135,136] Mazin and Singh has propounded an idea to explain this disagreement, namely the surface relaxation effect. The cleavage plane in Sr_2RuO_4 is associated with the rock salt layers, leaving SrO plane at the surface.[137] It has been reported that this SrO planes contains a lot of oxygen defects. The oxygen defects in SrO layer leave dangling bonds in the RuO_2 layer; the dangling bonds consist of Ru yz or zx orbitals mixed with O $2p\pi$ orbitals toward the SrO layer. These dangling bonds are contracted to modify strongly the transfer integral between the Ru yz or zx and O $2p\pi$ orbitals. Thus, the surface electronic state becomes different significantly from that of the bulk. The dHvA measurement probes bulk electronic structures, while the ARPES measurements with the photon energy of the vacuum ultra-violet region can merely probe a couple of layers from the surface. This issue should be settled by further experiments to observe the actual surface relaxation.

Nevertheless, it is necessary to study well-examined angle-integrated PES spectra of Sr_2RuO_4 to complement the above discussion on the ARPES spectra. We have confirmed with sufficient reproducibility the angle-integrated PES spectra by in-situ scraping the surfaces. Our data are rather different from those of other experiments,[138,139] in which the samples were cleaved and thus the data may not represent a complete angle-integrated spectra. Therefore, we hope that this study will trigger further theoretical and experimental projects to evaluate the validity of the photoemission results.

We describe the surface deterioration and concomitant change of the spectral shape in Sec. 6.3.1. Several results of resonance photoemission spectroscopy are shown in Sec. 6.3.2. Significant spectral weight redistribution of the Ru 4*d* band is shown in Sec. 6.3.3, and we discuss the mass renormalization factor, which is consistent with the value obtained by the specific heat measurement.[128]

6.2. Experiments

The UPS measurement was performed using a He discharge lamp in our laboratory setup (see Sec. 2.4.1), as well as using synchrotron light-source of the beamline BL-18A at the Photon Factory, High Energy Accelerator Research Organization.

The beamline BL-18A has been designed for experiments using vacuum-ultraviolet light and soft x-ray. The optical system of this beamline is illustrated schematically in

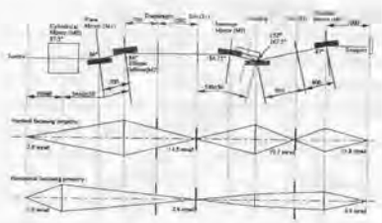

FIG. 6.1. Schematic picture of the constant deviation angle monochromator (CDM) of BL-18A. CDM consists of 5 mirrors, 2 slits, and 4 spherical gratings covering the output photon energy of 15 – 150 eV. The slit S1 moves together with the mirrors M1 and M2. This is concomitant with the rotation of the grating. Focusing properties are also plotted.

Fig. 6.1. The monochromator of this beam line is a constant deviation angle monochromator (CDM) with four gratings and five mirrors, which covers the energy range from 10 to 150 eV, and has the resolution of 2000. We can change *in situ* the four gratings [G_1, G_2, and G_3 (coated with gold), and G_4 (coated with aluminum)]; G_1 covers the photon energy range of 60 – 150 eV, G_2 covers 30 – 70 eV, G_3 covers 20 – 40 eV, and G_4 covers 10 – 25 eV. We used the grating G_2 for this experiment. The ultra-high vacuum chamber is equipped by the semi-spherical electron energy analyzer (VG, CLAM-I) with the total energy resolution of 56 meV. A liquid nitrogen cryostat is installed on the manipulator and we cool the sample at around 80 K.

For both experiments, we measured single-crystalline Sr_2RuO_4 samples of different batches, which were grown by a floating zone method.[112] We cleaned the surfaces of the samples thoroughly by *in-situ* scraping in an ultra-high vacuum spectrometer with a diamond file with particular care against possible surface degradation effects. During scraping and measurements, the sample temperature was maintained at ∼80 K to avoid desorption of oxygen from the surfaces.

By *in-situ* scraping of the surfaces, the large spectral intensity ∼5 eV below E_F, is eliminated drastically. Corresponding changes are also observed in Mg Kα x-ray photoemission spectra of the oxygen 1*s* core-level. The large satellite peak at a binding energy of ∼534 eV disappears by scraping as shown in Sec. 6.3.1.

Even at ∼ 80 K, the surfaces of the sample were considerably reactive, so that all the measurements were done within 20 minutes after scraping.

As a reference of E_F and the instrumental resolution, we measured the spectrum of Fermi cutoff of Au evaporated on the sample.

6.3. Results and Discussion

6.3.1. Surface degradation

The Mg Kα XPS spectra of the oxygen 1*s* core-level of Sr_2RuO_4 at ∼ 80 K with a photon energy of 1253.6 eV, which were taken before and after scraping, are plotted in Fig. 6.2. It is apparent that the large satellite peak at ∼ 534 eV disappears drastically by scraping the sample surfaces in situ. We also notice that the shoulder at lower binding energies disappears by scraping and the width of the main peak becomes narrower. Both features are considered to be due to surface degradation, because, as seen in the figure, the O 1*s* peak becomes much broader only after 6 hrs; therefore we checked the O 1*s* spectra in this way every time after scraping.

Since UPS measurement is more sensitive to the surface degradation, we should be careful enough to prevent the spectra from being affected by the surface degradation. Figure 6.2 also shows the UPS spectra of the valence band of Sr_2RuO_4 at ∼ 80 K. Corresponding to the change of the O 1*s* XPS spectra, before the in-situ scraping, there is almost no intensity below ∼ 3 eV, which increases drastically by scraping. The spectrum after scrap-

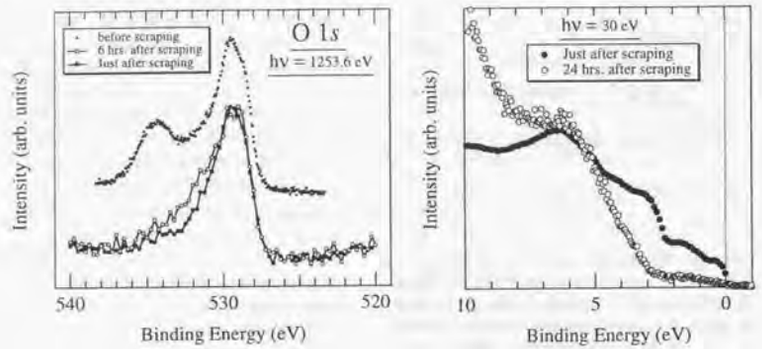

FIG. 6.2. **Left**: XPS spectra of O 1*s* core-level of Sr_2RuO_4 at $\sim$ 80 K. The large satellite peak at $\sim$ 534 eV due to a surface degradation disappears by scraping the surfaces in situ. **Right**: UPS spectra of the valence band of Sr_2RuO_4 at $\sim$ 80 K. A drastic change of the spectral intensity around the Fermi level was observed.

ing is well reproducible so that it is reasonable to consider that this spectrum is not affected by the experiment-dependent (irreproducible) surface degradation.

We regard, hereafter, the spectrum after in-situ scraping as an intrinsic quasi-particle spectrum $\rho_{\rm expt}(\omega)$ of the bulk of Sr_2RuO_4 and compare it with the non-interacting density of states (DOS) $D(\omega)$, although there may be an effect of the intrinsic (reproducible) surface state as discussed in the previous chapter.

6.3.2. Valence band resonance photoemission spectroscopy

The angle-integrated valence band UPS spectra were taken with the photon energies from 27.5 eV to 60.0 eV. A part of the spectra is displayed in Fig. 6.3. The intensity of each spectrum was normalized to the intensity of the incident photon-flux.

In order to study the photon-energy dependence of the UPS spectra more clearly, we have subtracted the overlapped secondary spectrum, *i.e.*, the so-called inelastic background, which represents the inelastic events after the photoexcited electron has left the site of the excitation process. The formula of the secondary spectrum function has been discussed by Tougaard *et al.* intensively,[98] however, we used here the more simple Shirley background[97] as shown in Fig. 6.4.

The cross-section of photoelectron excitation, *i.e.*, dipole transition probability, depends on both the angular momentum and the energy of the atomic orbital of the electron in the initial bound state. Fig. 6.5 shows the calculated photoexcitation cross-section for Ru 4*d* and O 2*p* atomic orbitals.

Actually, as seen in Fig. 6.3, the intensity of the different features of the UPS spectra changes as we change the photon energy; thereby, we have compared the observed photon-energy dependence to the calculated cross-section of photoelectron excitation. Although the photoexcitation cross-section of the band electrons in the bulk can be different from that for the atomic orbital, it is still valid for a qualitative discussion.

The observed UPS spectrum, after subtracting the secondary background, has been divided into five regions, each of which contains the prominent features of the UPS spectrum. We have examined the photon energy dependence of the four regions among them as defined in Fig. 6.6 (left).

The photon-energy dependences are plotted in Fig. 6.6 (right) against the incident photon energy. The region A, *i.e.*, the spectral DOS within $\sim$2 eV below $E_{\rm F}$ shows a resonance behavior around 46 – 54 eV, which we describe later, as well as showing the rapid increase as we decrease the photon energy from around 40 eV, followed by the maximum at around 32 eV. The latter behavior is comparable to that of Ru 4*d* in Fig. 6.5; this lulls us into considering the spectral DOS in this region has dominantly the Ru 4*d* character.

This is corroborated by the resonance behavior as discussed below. The region B, *i.e.*, the peak at $\sim$4 eV shows monotonous increase as we decrease the photon energy; no resonance type behaviors were seen within the experimental accuracy. This is comparable to that of O 2*p* in Fig. 6.5, implying that region B consists of mainly O 2*p* character. The regions C and D show similar behavior, and the photon-energy dependence is almost the average of Ru 4*d* and O 2*p*. This seems to suggest that this area consists of both Ru 4*d* and O 2*p* character. However, the intensity of this area is considerably affected by the shape of the secondary electron background, so that we are not able to confirm the character through this analysis alone.

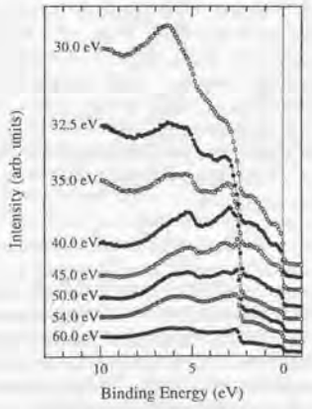

FIG. 6.3. Angle-integrated valence band UPS spectra of Sr_2RuO_4 taken by varying the photon energy from 30.0 eV to 60.0 eV.

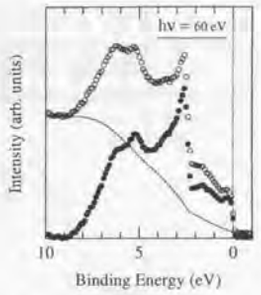

FIG. 6.4. Secondary electron spectrum has been subtracted from the UPS spectrum of Sr_2RuO_4, assuming the simple Shirley background[97] (dotted line).

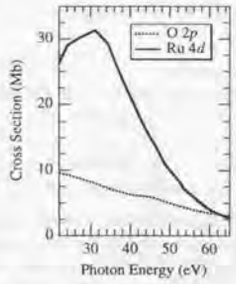

FIG. 6.5. Calculated photoexcitation cross-section for Ru 4*d* and O 2*p* atomic orbitals.[140]

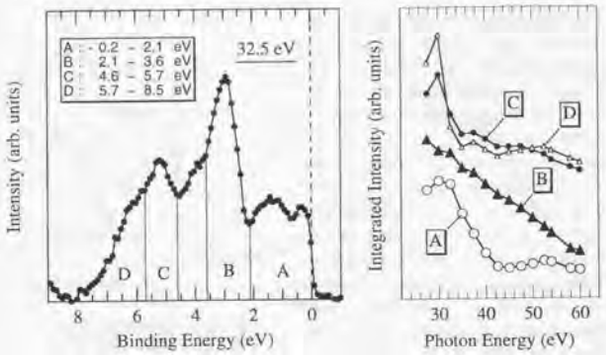

FIG. 6.6. **Left**: Definition of binding-energy regions A ($-0.2 \sim 2.1$ eV), B ($2.1 \sim 3.6$ eV), C ($4.6 \sim 5.7$ eV), and D ($5.7 \sim 8.5$ eV) for the UPS spectrum of Sr_2RuO_4. **Right**: Total area of each region is plotted against the photon energy.

The results of the above analysis for the photon-energy dependence are almost consistent with the prediction of the LDA band calculation,[132-134] where the Ru $4d$ character is dominant near the Fermi level and the O $2p$ character is superior around 2 to 4 eV.

The observed photon-energy dependence of the spectral intensity in this measurement is considerably different from what was reported so far by Yokoya *et al.*[138] The significant enhancement of the feature at ~ 6 eV toward the lower photon energy in Ref. 138 was not observed in our measurement. A resonance-like behavior over a fairly wide photon energy range about the peak at ~ 4 eV was also reported in Ref. 138; however, this, too, was not seen in our experiment.

Here we note that some features may show a Fano-like intensity modulation as a function of photon energy near the absorption threshold of a core-level, since quantum interference occurs between a direct excitation of a valence-band electron (photoemission) and autoionization (AI) or direct recombination, which follows the decay of the core-hole. The two processes can interfere with one another, resulting in greatly decreased transition rates below threshold and enhanced ones above it. This phenomenon is often referred to as resonance photoemission (RPES). Fig. 6.7 shows the core-level XPS spectrum of Sr_2RuO_4 for the Ru $4p$ and Sr $4s$ peaks. The binding energy of the Ru $4p$ peak (we cannot separate the $4p_{1/2}$ and $4p_{3/2}$ peaks, because the spin-orbit splitting energy is much smaller than the experimental resolution.) is ~ 46 eV, which should be the threshold energy (see Sec. 2.3.2) of the possible resonant behavior with the autoionization of

$$4d^4 \xrightarrow{\hbar\omega} \underline{4p}4d^5 \xrightarrow{\mathrm{AI}} 4d^3 + \text{photoelectron}\,,$$

where $\underline{4p}$ denotes the photohole in the Ru $4p$ level. Our measurement shows a weak but recognizable resonant behavior in the intensity of region A for the photon-energy range between ~ 44 eV and ~ 52 eV. On the other hand, region B does not show any resonant behavior in this photon energy range. These results corroborate our characterization for each feature of the UPS spectrum: *i.e.*, region A originate from the Ru $4d$ band, and region B from the O $2p$ band predominantly. For regions C and D, the photon-energy dependence is closer to that of A than that of B. Therefore, we can infer that the regions also contain some amount of Ru $4d$ character, consistent with the LDA band calculation. We could not observe such a strong resonance effect as is observed in $3d$ transition-metal oxides and rare-earth compounds. This means that the intermediate state is not as localized in Sr_2RuO_4, suggesting that electron correlations in this material are not so strong as those in some $3d$ transition metal compounds.

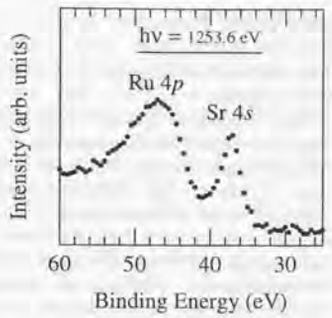

FIG. 6.7. Core-level XPS spectrum of Sr_2RuO_4 for the Ru $4p$ and Sr $4s$ peaks. The binding energy of the Ru $4p$ is ~ 46 eV, which should be the threshold energy of the possible resonant behavior.

Although we were circumspect in preparing the surface of this material as clean as possible, and have confirmed the reproducibility of the spectrum in several independent measurements using different batches of single crystalline samples, we cannot declare that our spectra reflect only the bulk properties, because the clean surface can form an "intrinsic" surface electronic state which is considerably different from that of the bulk. (See the discussion in Sect. 5.3.5.) Yokoya *et al.* cleaved the sample *in situ*,[138] while we scraped the sample surfaces *in situ* by a diamond file. A possible different condition of the sample surfaces due to the difference of the surface preparation might be a reason for the severe difference of the RPES results; we need to clarify this issue by more elaborate measurements.

6.3.3. Valence band ultraviolet photoemission spectroscopy

The UPS spectrum $\rho^{\sigma}_{\mathrm{exp}}(\omega)$ of Sr_2RuO_4 at ~ 80 K taken with the photon energy of 21.22 eV is compared with the density of states (DOS) $D^{\sigma}(\omega)$ calculated by the linear-augmented-plane-wave method using the local density approximation (LDA).[132] $D^{\sigma}(\omega)$ plotted in Fig. 6.8 is composed of the partial DOS's of Ru $4d$ and O $2p$ band multiplied by the photoexcitation cross sections of the corresponding atomic orbitals.[140]

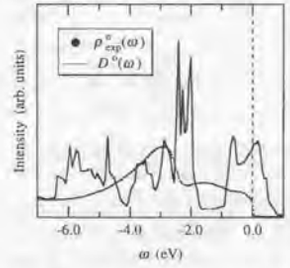

FIG. 6.8. UPS spectrum $\rho^{\sigma}_{\mathrm{exp}}(\omega)$ of Sr_2RuO_4 at ~ 80 K taken with the photon energy of 21.22 eV. Density of states $D^{\sigma}(\omega)$ obtained by the band calculation with LDA is also plotted for comparison.[132]

In order to compare $\rho^{\sigma}_{\mathrm{exp}}(\omega)$ and $D^{\sigma}(\omega)$ around E_{F}, we have adopted appropriate backgrounds representing a tail of the O $2p$ band below $\omega \approx -2$ eV. As shown in Fig. 6.9, we have subtracted the backgrounds from both $\rho^{\sigma}_{\mathrm{exp}}(\omega)$ and $D^{\sigma}(\omega)$, and thus obtained $\rho_{\mathrm{exp}}(\omega)$ and $D(\omega)$, respectively.[141] For $D(\omega)$,

a Fermi distribution function for the temperature of 80 K has been multiplied and a convolution with a gaussian corresponding to the instrumental broadening (45 meV) has also been applied. Finally, both spectra were normalized to the same area.

As is apparent from this figure, $\rho_{\rm exp}(\omega)$ is completely different from $D(\omega)$. Large spectral weight transfer from around $E_{\rm F}$ to the energy region $\omega \cong -1.5$ eV can be clearly seen in this figure.

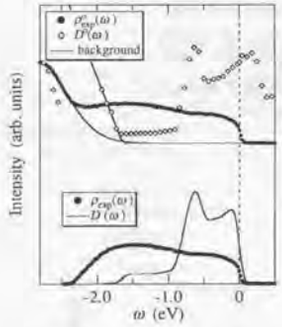

FIG. 6.9. From both $\rho^{o}_{\rm exp}(\omega)$ and $D^{o}(\omega)$ a tail of the O $2p$ band was subtracted, and thus we obtained $\rho_{\rm exp}(\omega)$ and $D(\omega)$. $D(\omega)$ has been multiplied by a Fermi distribution function for 80 K and has been convoluted by a gaussian corresponding to the instrumental broadening (45 meV).

This spectral weight redistribution is similar to those observed in the $3d^1$ correlated metals.[59,91] As discussed in the previous chapter, when we increase the electron correlation strength U/W from the non-interacting limit, one finds that DOS splits into a characteristic three-peak structure. The central "coherent" quasi-particle peak at $E_{\rm F}$ narrows as the electron correlation is increased, corresponding to the increase of the effective mass. This feature is accompanied by the emergence of the lower and upper Hubbard bands at energies of the order of $\pm \frac{U}{2}$. These "incoherent" peaks acquire the spectral weight which is transferred from the lower energy region as the coherent peak narrows.

There is another feature in the observed $\rho_{\rm exp}(\omega)$ that needs further attention. It is obvious in Fig. 6.9 that $\rho_{\rm exp}(E_{\rm F})$ is much smaller than $D(E_{\rm F})$. In the dynamical mean-field approach to the Hubbard model, the single-particle self-energy is local and hence one can map the problem to the single impurity Anderson model. Then, the coherent quasi-particle band corresponds to a Kondo resonance peak and $\rho_{\rm exp}(E_{\rm F})$ should be exactly equal to $D(E_{\rm F})$. This is inconsistent with our experimental results; the coherent peak is seen to be considerably suppressed. One may suspect that the suppression of $\rho_{\rm exp}(E_{\rm F})$ may be caused by smearing of a sharp peak at $E_{\rm F}$ due to limited resolution (45 meV). In that case, the peak would have to be extremely sharp (the width should be at most 45 meV), and correspondingly the effective mass should become extremely large. However, the electronic specific heat coefficient in Sr_2RuO_4 (39 mJ K^{-2} mol^{-1})[112] is not so enhanced, if one compares with the heavy Fermion system. The thermal effective mass $m^*/m_{\rm b}$ in Sr_2RuO_4 is 3.8, where the band mass $m_{\rm b}$ obtained by the LDA calculation.[132] These results are similar to what we have observed in $Ca_{1-x}Sr_xVO_3$ system (Chaps. 4 and 5); therefore, we try to consider the effect of nonlocal interaction also in this system. Since the importance of the ferromagnetic spin fluctuation has already been pointed out for Sr_2RuO_4, the self-energy in which all the interaction is included must be nonlocal; moreover the low dimensionality of this system limits the screening path, making the poorly screened long range Coulomb interaction play an important role.

This kind of nonlocal interaction, such as the long-range exchange/correlation, spin/orbital fluctuations, and so on, is known to suppress $\rho_{\rm exp}(E_{\rm F})$ as well as to supress the

effective-mass enhancement[59,62] (see, Chaps. 4 and 5).

Following this scenario, let us now turn to a more detailed comparison of $\rho_{\rm exp}(\omega)$ with $D(\omega)$. Here, we try to consider the effect of nonlocal interaction by the self-energy correction of LDA DOS with the phenomenological $\vec{k}$-dependent self-energy $\Sigma(\omega,\vec{k})$.[59] As mentioned in Chap. 5, LDA band calculation is generally used as a reference of a mean-field state to which the self-energy correction is applied. Although the LDA band-structure calculations give correct Fermi surfaces, these calculations do not consider electron correlation effects properly, because of the spurious self-interaction inherent in the LDA potential. Furthermore, since the exchange potential is approximated by a local potential in LDA, the $\vec{k}$-dependence of the self-energy should be taken into account if one analyzes photoemission spectra starting from the LDA band-structure.

As described in Sec. 2.5.2, the Green function can be written, in general, by the following continued fraction expansion (Eq. 2.7),

$$G(\omega,\vec{k}) = \cfrac{1}{\omega - \varepsilon^{\rm LDA}_{\vec{k}} - \omega_1 - \cfrac{{s_2}^2}{\omega-\omega_3-\cfrac{{s_4}^2}{\omega-\omega_5-\cdots}}},$$

which is valid asymptotically at high energies,[32] where $\varepsilon^{\rm LDA}_{\vec{k}}$ corresponds to the energy dispersion of a single-electron band obtained by the LDA band calculation. In this study, we use $\varepsilon^{\rm LDA}_{\vec{k}}$ instead of $\varepsilon^{\rm o}_{\vec{k}}$ which is the energy of a noninteracting Bloch electron.

$\Sigma(\omega,\vec{k})$, as used in Ref. 110, corresponds to $\Sigma(\omega,\vec{k})$ obtained by truncating the above expansion at the "modified Padé-level" $L=3$ (see, Sec. 2.5.2 for details), *i.e.*, up to s_4, and ω_5. Under the general requirements of the self-energy near $\omega=0$ and $\vec{k}=\vec{k}_{\rm F}$ together with the Fermi-liquid conditions, we write

$$\begin{aligned} \omega_1 &= (\alpha-1)\varepsilon^{\rm LDA}_{\vec{k}} \\ s_2 &= \sqrt{g\Delta\Gamma} \\ \omega_3 &= -i(\Delta+\Gamma) \\ s_4 &= \sqrt{\Delta\Gamma} \\ \omega_5 &= 0\,, \end{aligned}$$

where $\varepsilon^{\rm LDA}_{\vec{k}}$ denotes the one-electron energy of the LDA band calculation, and α, g, Δ, and Γ are controlling parameters, all of which are real and positive. ω_1 is thus the only $\vec{k}$-dependent parameter, while the other parameters are $\vec{k}$-independent.

Then, we obtain

$$\Sigma(\omega,\vec{k}) = \Sigma(\omega) + \Sigma(\vec{k})\,, \tag{6.1}$$

where

$$\Sigma(\omega) = g\omega\frac{\Delta}{\omega+i\Delta}\frac{\Gamma}{\omega+i\Gamma}\,, \tag{6.2}$$

and

$$\Sigma(\vec{k}) \equiv (\alpha-1)\varepsilon^{\rm LDA}_{\vec{k}}\,. \tag{6.3}$$

It should be noted here that this is exactly the same analysis explained in detail in Sec. 5.3.4, but later in this section, we introduce another level of the approximation.

Using this self-energy, we have calculated the quasi-particle spectrum $\rho(\omega)$ (see Eq. 2.6),

$$\rho(\omega) = -\frac{1}{\pi}\int_{-\infty}^{\infty} d\varepsilon^{\rm LDA}_{\vec{k}} D(\varepsilon^{\rm LDA}_{\vec{k}}) {\rm Im}G(\vec{k},\omega)$$

and compared it with the observed spectral DOS $\rho_{\rm exp}(\omega)$ using the adjustable parameters α, g, Δ ($\omega_5=0$) and Γ.

The $\vec{k}$-dependence of the self-energy leads the thermal effective mass to be expressed as the product of the "k-mass" $m_{\rm k}/m_{\rm b}$ and the "ω-mass" $m_\omega/m_{\rm b}$ (see Eq. 4.9),[35,59,73] *i.e.*,

$$\begin{aligned} \frac{m^*}{m_{\rm b}} &= \left(1-\left.\frac{\partial {\rm Re}\Sigma(\vec{k},\omega)}{\partial\omega}\right|_{\omega=E_{\rm F}}\right) \\ &\times \left|\frac{\left.\frac{d\varepsilon^{\rm LDA}_{\vec{k}}}{d\vec{k}}\right|_{\vec{k}=\vec{k}_{\rm F}}}{\left.\frac{d\varepsilon^{\rm LDA}_{\vec{k}}}{d\vec{k}}\right|_{\vec{k}=\vec{k}_{\rm F}} + \left.\frac{\partial {\rm Re}\Sigma(\vec{k},\omega)}{\partial\vec{k}}\right|_{\vec{k}=\vec{k}_{\rm F}}}\right| \\ &\equiv \frac{m_\omega}{m_{\rm b}}\times\frac{m_{\rm k}}{m_{\rm b}}\,, \end{aligned}$$

TABLE 6.I. Parameters used in the self-energy correction of the LDA DOS with Eqs. 6.1, 6.2, and 6.3 to fit the UPS spectrum of Sr_2RuO_4.

α	g	Δ (eV)	Γ (eV)
2.50	10.1	0.247	0.101

m^*/m_b	m_ω/m_b	m_k/m_b
4.43	11.1	0.40

In Fig. 6.10, it is demonstrated how $\rho(\omega)$ is obtained from LDA DOS $D(\omega)$ by the self-energy correction. First, $D(\omega)$ is uniformly widened

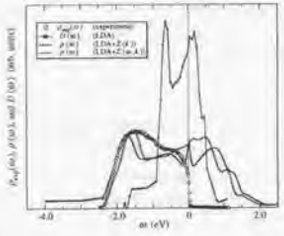

FIG. 6.10. $\rho(\omega)$ is obtained from LDA DOS $D(\omega)$ by the self-energy correction; $D(\omega)$ is widened by $\Sigma(\vec{k})$, and then, by the effect of $\Sigma(\omega)$, a narrow quasi-particle band appears at E_F. No correction for the finite temperature nor the instrumental broadening has been made.

by introducing $\Sigma(\vec{k})$, and then by the effect of $\Sigma(\omega)$, a narrow quasi-particle band appears at E_F. Once we multiply a Fermi distribution function to $\rho(\omega)$ and a gaussian for the instrumental broadening is convoluted, $\rho(\omega)$ gives a reasonable fit to $\rho_{exp}(\omega)$ as displayed in Fig. 6.11 (left) with the values of parameters listed in Table 6.I.

The value of m^*/m_b is in fairly good agreement with that obtained from the electronic specific heat coefficient: $m^*/m_b = 3.8$.

Nevertheless, in the above discussion, the naive introduction of the $\vec{k}$-dependent self-energy, by modeling $\omega_1 = (\alpha - 1)\varepsilon_k^{LDA}$ with $\alpha = 2.5$ and by leaving the other parameters $\vec{k}$-independent, results in the strong $\vec{k}$-dependence of the self-energy, *i.e.*, $\Sigma(\infty, \vec{k}) = 1.5\varepsilon_k^{LDA}$. This leads to a violation of the Koopman's theorem.[21]

Therefore, we introduce here the $\vec{k}$-dependence in a more appropriate fashion. However, since it is rather a tough issue to consider the $\vec{k}$-dependence for the self-energy up to s_4 and ω_5, we truncate the expansion at s_2 and ω_3 (single-pole expression), *i.e.*, the Padé approximation up to $L = 1$. Then, the self-energy is expressed as

$$\Sigma(\omega) = \omega_1 - \frac{\alpha\,{\omega_3}^2}{\omega - \omega_3},$$

where $\alpha = -\mathrm{Im}(\omega_1)/\mathrm{Im}(\omega_3)$.[142] The leading (0th-order of ω) term of the low energy expansion of $\Sigma(\omega, \vec{k})$ is $\omega_1 + \alpha\omega_3$. The Fermi liquid condition requires $\Sigma(0, k_F) = 0$, which means $\omega_1 + \alpha\omega_3 = 0$ at $k = k_F$. Thus we assume here that $\omega_1 + \alpha\omega_3$ would vary linearly in ε_k^{LDA} in the whole Brillouin zone, *i.e.*, $\omega_1 + \alpha\omega_3 = \gamma\varepsilon_k^{LDA}$. Eliminating ω_3 by this equality, we obtain an explicit expression for the self-energy:

$$\Sigma(\omega) = \frac{\omega_1(\alpha\omega + \gamma\varepsilon_k^{LDA}) - (\gamma\varepsilon_k^{LDA})^2}{\alpha\omega + \omega_1 - \gamma\varepsilon_k^{LDA}}. \tag{6.4}$$

In Fig. 6.11 (right), $\rho(\omega)$ calculated using this $\Sigma(\omega, \vec{k})$ is displayed with the LDA DOS $D(\omega)$ and the UPS spectrum $\rho_{exp}(\omega)$. Here we should note that we have focused our fit on the low energy region between -0.8 eV to 0.1 eV, where the single-pole expression is most precise. The parameters used here are listed in Table 6.II

The deduced value of m^*/m_b is again in good agreement with that obtained from the specific heat measurement. Thus, we have corroborated that it is a fairly reasonable ansatz to consider some appropriate $\vec{k}$-dependent self-energy, regardless of its precise shape, for

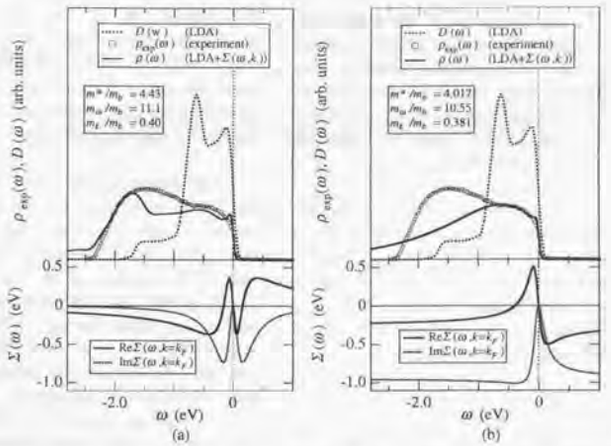

FIG. 6.11. **Left**: $\rho(\omega)$ calculated from LDA DOS $D(\omega)$ by the self-energy correction with Eqs. 6.1, 6.2, and 6.3. **Right**: $\rho(\omega)$ calculated from LDA DOS $D(\omega)$ by the self-energy correction with Eq. 6.4. For both figures, $D(\omega)$ has been multiplied by a Fermi distribution function for 80 K and has been convoluted by a gaussian corresponding to the instrumental broadening (45 meV).

TABLE 6.II. Parameters used in the self-energy correction of the LDA DOS with Eq. 6.4 to fit the UPS spectrum of Sr_2RuO_4.

γ	α	ω_1
1.625	-9.551	$-0.254 + 0.938i$

m^*/m_b	m_ω/m_b	m_k/m_b
4.017	10.55	0.381

explaining consistently the strong depletion of $\rho_{exp}(\omega)$ at E_F concomitant with the moderate mass-enhancement, each of which seems to be inconsistent with the other in the dynamical mean-field treatment of the electron correlations.

In case of Hubbard models at half-filling, regardless of dimensionality, the relation $s_2 = U/2$ holds exactly, where U is the effective value of the electron correlation. Applying the relation to the above parameters, we obtain $U \cong 1.3$ eV. Although $U \cong 1.3$ eV is not a small value, it is rather a reasonable value for this kind of relatively narrow 4*d* band system. However, the validity of this estimation of the U value remains debatable, since Sr_2RuO_4 is not half-filled and the ground state is degenerate.

With all these issues, a valid argument is that the large damping of the spectral intensity at E_F is caused by the $\vec{k}$-dependence of the self-energy. The small m_k/m_b means that $\partial\Sigma(\vec{k}_F, E_F)/\partial\vec{k}$ is large at $k = k_F$.[62,72] In conventional metals, where the Coulomb potential is short ranged because of the sufficient screening effect and the nonlocality of the exchange interaction is small, the above singularity of the momentum-derivative of the self energy is strongly reduced. As we dis-

cussed in Chap. 4, in most of the perovskite-type TM oxides, the carrier density is fairly small and thus the screening effect is very poor. Moreover, the degenerate ground state induces spin/orbital fluctuations. Therefore, the nonlocal effect will be larger, and this will become especially significant in the vicinity of the MIT point.

The Sr_2RuO_4 system has shown us another typical example of a material in which the Coulomb interaction is no longer a well screened short-range interaction. We think this is due to the limited number of screening paths inherent in low-dimensional systems, as well as the strong electron correlations.

6.4. Summary

Angle-integrated UPS measurements have been performed for the single-crystalline layered-perovskite-type superconductor Sr_2RuO_4. The surface of the samples was scraped in the ultra-high vacuum chamber at 80 K, the possible surface degradation was carefully checked by monitoring the O 1*s* core-level XPS spectrum, and we have confirmed with sufficient reproducibility the valence band spectra. This is thus the first well-characterized angle-integrated photoemission spectra of this material.

RPES measurements have corroborated the band-like (itinerant) nature of the Ru 4*d* electrons with weak $4p - 4d$ resonance enhancement. Nevertheless, we have found that the UPS spectrum of Sr_2RuO_4 around E_F shows significant spectral weight redistribution. This seems to be evidence of the extremely strong electron correlations, but the effective mass is, on the other hand, not as strongly enhanced as expected. This contradiction can be explained consistently by considering the $\vec{k}$-dependence of the self-energy; *i.e.*, the nonlocal exchange/correlation, that results from the poor screening inherent in the low dimensionality, and/or from the ferromagnetic fluctuation, are important in this system.

Chapter 7

Summary and Concluding Remarks

7.1. Summary

In this Thesis, we aimed at exploring the nature of the Mott Transition from the view point that the nonlocal interaction must play an important role, especially near the transition point from the correlated metal to the Mott insulator. For this purpose, two perovskite-related systems were studied. The first one was the metallic vanadate, $Ca_{1-x}Sr_xVO_3$, which has nominally one 3*d* electron per vanadium ion. The second one was the superconducting Sr_2RuO_4 with a layered-perovskite structure, which has the same crystal structure as that of $La_{2-x}Ba_xCuO_4$.

7.1.1. *Electronic states of $Ca_{1-x}Sr_xVO_3$*

We have succeeded in preparing single crystals of the metallic alloy system $Ca_{1-x}Sr_xVO_3$ using the FZ method, for the first time. The system has nominally one 3*d* electron per vanadium ion; as we substitute a Ca^{2+} ion for a Sr^{2+} ion, the one-electron bandwidth W decreases due to the buckling of the V-O-V bond angle from $\sim 180°$ for $SrVO_3$ to $\sim 160°$ for $CaVO_3$, which is almost equal to the analogous $3d^1$ insulator $LaTiO_3$.

As for $CaVO_3$, we have revealed that stoichiometric $CaVO_{3-\delta}$ ($\delta \cong 0.00$) shows better metallic conductivity than off-stoichiometric $CaVO_{3-\delta}$. In general, $CaVO_{3-\delta}$ has "oxygen-defects" and is difficult to oxidize further ($\delta <$ 0) around room temperature. Nevertheless, a very slight peroxidation ($\delta \cong -0.05$) leads the system insulating without inducing any significant structural changes. We have also found drastic, unconventional changes of the magnetoresistance, magnetic susceptibility, and Hall effect in single-crystalline $CaVO_{3-\delta}$ ($\delta > 0$). The mechanism of these phenomena, as well as the nature of the MI transition in $CaVO_{3-\delta}$ ($\delta < 0$), are still under investigations.

For the whole $Ca_{1-x}Sr_xVO_3$ system irrespective of the value of x, the Sommerfeld-Wilson ratio R_W is almost equal to 2. The Kadowaki-Woods ratio A/γ^2 lies in the same region as for the heavy Fermion compounds. There is also a large contribution from electron-electron scattering to the resistivity even at room temperature. These features above provide strong evidence of the large electron correlations in this system. However, the density of states at the Fermi level $D(E_F)$ obtained by the thermodynamic (γ) and magnetic (χ_P) measurements show only a moderate increase in going from $SrVO_3$ to $CaVO_3$ compared to $D(E_F)$ deduced from the LDA band calculations This is inconsistent to the divergence of the effective mass expected from the Brinkman-Rice picture.

Accordingly, we suggest that LDA DOS cannot be interpreted as the bare non-interacting DOS, required as an input to the *mean-field*-type many-body formalism of the electron correlations; this indeed invokes the

idea of the additional nonlocal electron correlations, *i.e.*, the $\vec{k}$-dependent self-energy.

In order to check the application of the $\vec{k}$-dependent self-energy, we have performed several high-energy spectroscopies, such as XPS, XAS, and UPS.

The core level XPS has shown that the V $2p$ and O $1s$ spectrum consist of three peaks even in the end members, $CaVO_3$ and $SrVO_3$; this can be attributed to the intrinsic surface electronic states, *i.e.*, the charge disproportionation ($2V^{4+} \rightarrow V^{3+} + V^{5+}$).

Both the O $1s$ edge and V $2p$ edge XAS spectra cannot be explained by either the cluster model calculations or the LDA band calculations; this may be understood by the overlapping surface contribution, or by the formation of the Hubbard bands.

UPS spectra were completely different from LDA DOS, and consist of two well-defined features: one is the quasiparticle peak at E_F, and the other is the high energy excitations $\sim 1.7\,\mathrm{eV}$ signaling the formation of LHB. As we increase the magnitude of U/W, a large amount of the spectral weight is transferred from the coherent band to the precursor of LHB.

We have succeeded to separate out the surface and bulk contributions from the total spectrum. We found a novel MI transition at the surface with a change in x, while the bulk remains metallic. This can be caused by the charge disproportionation at the surface, and has never been observed in any other material.

We have compared the ordinary UPS spectra to the bulk spectra of the newborn measurement in order to extract the common properties. We havee calculated a spectral DOS using the large-d Hubbard model within the LISA method, as well as by the phenomenological introduction of the self-energy correction to the LDA DOS. The suppression of $\rho(E_F)$, which was observed in both experiments, has indicated that there are some interactions treated insufficiently, thus, a correction to the local single-particle self-energy is necessary to reproduce the observed spectra. By squashing all those undetermined interactions, which are omitted in either LDA or LISA, into the tentative $\vec{k}$-dependence of the self-energy phenomenologically, we could obtain reasonable values of m^*/m_b as well as the reasonable fit to the experimental spectra.

7.1.2. Electronic states of Sr_2RuO_4

Sr_2RuO_4 is the only copper-free superconductor with the same crystal structure as that of $La_{2-x}Ba_xCuO_4$. Sr_2RuO_4 exhibits superconductivity below $T_c = 1.50\,\mathrm{K}$, and a great deal of work has been carried out into the nature of its superconductivity, particularly since some fingerprints of a peculiar p-wave superconductivity have been recently reported.

Angle-integrated photoemission spectroscopic measurements have been performed for the single-crystalline Sr_2RuO_4; this is the first well-characterized angle-integrated photoemission study on this material. Because of the recent controversy regarding the surface contribution to the photoemission spectrum of Sr_2RuO_4, we have taken particular care for the surface preparations. The surface of the samples was scraped in the ultra-high vacuum chamber at 80 K, the possible surface degradation was carefully checked by monitoring the O $1s$ core-level XPS spectrum, and we have confirmed with *sufficient reproducibility*, the valence band spectra by a number of independent measurements.

RPES measurements have corroborated the band-like (itinerant) nature of the Ru $4d$ electrons with weak $4p - 4d$ resonance enhancement. Nevertheless, we have found that the UPS spectrum of Sr_2RuO_4 around E_F shows significant spectral weight redistribution. This seems to be evidence of the extremely strong electron correlations, but the effective mass is, on the other hand, not as strongly enhanced as expected. This contradiction can be also explained consistently in the same fashion as we developed for the $Ca_{1-x}Sr_xVO_3$ system; *i.e.*, by considering the tentative $\vec{k}$-dependence of the self-energy correction to the LDA DOS. Therefore, Sr_2RuO_4 gives us another example in which the nonlocal interaction may become important. We consider that the origin of the nonlocal interaction is the nonlocal exchange or correlation interaction resulting from the poor screening of Coulomb interaction inherent in the low dimensionality of this system, and/or from the ferromagnetic as well as the orbital fluctuations.

7.2. Description of the Mott transition: Future problems

7.2.1. Alliance between large-d Hubbard model and LDA band calculations

As demonstrated by the UPS spectra, the LDA band calculation should include some form of self-energy correction, since, in the LDA approach, we completely fail to produce the satellite or the incoherent spectral features arising from many-body effects, that are not contained adequately in the LDA formalism. This local many-body effects, *i.e.*, the formation of the Hubbard band and its intensity, are well explained by the large-d Hubbard model within the LISA method.

We have also found that LDA overestimates $D(E_F)$ as well as underestimates the bare bandwidth compared to those of the large-d Hubbard model within the LISA method; *i.e.*, the DOS obtained from LDA cannot be interpreted as an input to the bare DOS of the mean-field type many-body formalism. This discrepancy between LDA DOS and bare DOS of LISA in terms of the bandwidth and the $D(E_F)$ was indeed the basis for invoking the nonlocal self-energy. We have also speculated that this nonlocal effect may become significant near the Mott transition or in a low dimension system, where poor screening of the Coulomb interactions exists.

Although we have succeeded to introduce an appropriate but tentative $\vec{k}$-dependent self-energy phenomenologically, it is no doubt a difficult task at present to estimate the *intrinsic* $\vec{k}$-dependent contribution to the self-energy experimentally, because in order to deduce the form of the $\vec{k}$-dependence, we have to compare the experimental data to a theoretical model of the non-interacting limit.

Especially, with regards to the comparison to the LDA band calculation as we actually did in this work, the obtained $\vec{k}$-dependence of the self-energy may be far from the intrinsic one, because the obtained $\vec{k}$-dependent self-energy might have only compensated the self-interaction effect inherent in the LDA potential. It is known that LDA includes the Coulomb interaction term within an effectively single-particle-wise but self-consistent manner, and that this leads to a considerable narrowing of the bandwidths compared to the Hartree-Fock approximation in which nonlocal exchange is properly taken into account.

On the other hand, for the large-d Hubbard model, the neglect of the degeneracy implicit in the practical use of the large-d Hubbard model may lead to a wider occupied bandwidth. Moreover, it is also not clear what the implications are of ignoring the oxygen sublattice in this case. Clearly it would be ideal, and therefore highly desirable, to include the more realistic lattice for the multiband Hubbard model (the alliance between the large-d Hubbard model and the LDA band calculation). But theoretical problems associated with such a task have not been made so far.

It is interesting to note that this important point has not been appreciated sufficiently in the context of electronic structures of strongly correlated systems. Thus, more elaborate theoretical as well as experimental studies in future are really expected to elucidate the nature of the nonlocal interaction, *i.e.*, to clarify the *true colors* of the Mott transitions.

7.2.2. A Tale of Two Energy Scales

This Thesisis one of the first experimental attempts to combine the high-energy spectroscopy spectrum to the thermodynamic property and the static magnetization in a single Mott-Hubbard system. To explain both of the experimental data consistently is a challenging problem, since they belong to vastly different energy scales. The photoemission spectroscopy is a probe for typically a high energy ($0.1 \sim 1\,\mathrm{eV}$), while the thermodynamic and magnetic measurements probe electrons typically within $k_{\mathrm{B}}T$ ($\sim 1\,\mathrm{meV}$) of E_{F}. Hence, our attempt may be likened to use a sledge-hammer to crack a nut. Actually, there is indeed *a-priori* no reason to believe that the same model physics will be valid in both the regimes.

Nevertheless, our trial seems to have succeeded to get a coherent view encompassing this vast energy scale.

With the high-energy probe, we have obtained the picture of the systematic evolution of the photoemission spectrum, where the DOS in the non-interacting limit splits into LHB, UHB, and the quasiparticle band at E_{F} by the effect of on-site electron correlation. Moreover, with this high-energy probe, we found the other interesting feature: the bare DOS, which is the non-interacting limit of the large-d Hubbard model with LISA method, can not be similar to LDA DOS. In order to bridge-build between the two approaches, we introduced the nonlocal self-energy phenomenologically, which worked, in this case, to broaden the LDA band and thus reduce $D(E_{\mathrm{F}})$; with this broadened DOS, we can fit the observed data sufficiently by the large-d Hubbard model.

With the low energy probe, on the other hand, we have confirmed the validity of this model; *i.e.*, the large enhancement of the ω-mass, which is expected from the large spectral weight transfer in the high-energy region, is actually canceled. This is considered to be due to the small k-mass; *i.e.*, the effective mass is the product of the ω-mass and k-mass

$$\frac{m^*}{m_{\mathrm{b}}} \equiv \frac{m_\omega}{m_{\mathrm{b}}} \times \frac{m_{\mathrm{k}}}{m_{\mathrm{b}}},$$

the former corresponds to the high-energy spectral weight redistribution, and the latter comes from the nonlocal self-energy.

The elucidation of what kind of interaction is actually squashed into the above phenomenological nonlocal self-energy, as well as to investigate whether this picture may valid in the very vicinity of the Mott transition are still an open question to be studied in the future work. This kind of study will give us the ***detail*** of two energy scale, which is one of the most important problems in the physics of strongly correlated electron systems, attracting a great deal of attention.[9,92] We hope this work can be a milestone of this attempt.

References

[1] N. F. Mott, Proc. Phys. Soc. London Sect. **A62**, 416 (1949).

[2] Borrowed from "Images of Physicists" (http://charm.physics.ucsb.edu/people/hnn/physicists.html).

[3] J. H. Van Vleck, Rev. Mod. Phys. **25**, 220 (1953).

[4] J. C. Slater, Phys. Rev. **49**, 537 (1936); *ibid* **49**, 931 (1936).

[5] R. E. Peierls explained this idea in 1938. see N. F. Mott, Proc. Phys. Soc. London Sect. **A371**, 56 (1980).

[6] J. Hubbard, Proc. R. Soc. London A **276**, 238 (1963).

[7] N. F. Mott, *Metal Insulator Transitions, Second Edition* (Taylor and Francis, London 1990).

[8] D. B. McWhan, A. Menth, J. P. Remeika, W.F. Brinkman, and T. M. Rice, Phys. Rev. B **7**, 1920 (1973); S.A. Carter, T. F. Rosenbaum, P. Metcalf, J. M. Honig, and J. Spalek, *ibid.* **48**, 16841 (1993); S.A. Carter, T. F. Rosenbaum, M. Lu, H. M. Jaeger, P. Metcalf, J. M. Honig, and J. Spalek, Phys. Rev. Lett. **77**, 1378 (1994).

[9] M. Imada, A. Fujimori, and Y. Tokura, Rev. Mod. Phys. **70**, (Oct. 1998).

[10] W. F. Brinkman and T. M. Rice, Phys. Rev. B **2**, 4302 (1970).

[11] M. C. Gutzwiller, Phy. Rev. Lett. **10**, 159 (1963).

[12] R. S. Roth, J. Research NBS **58**, RP2736 (1957).

[13] A. Fujimori, J. Phys. Chem. Solids **53**, 1595 (1992).

[14] M. Marezio, J. P. Remeika, and P. D. Dernier, Acta Crystallogr. B **26**, 2008 (1970); D. A. MacLean, Hok-Nam Ng, and J.E. Greedan, J. Solid State Chem. **30**, 30 (1979).

[15] J. G. Bednorz, and K. A. Müller, Z. Phys. B **64**, 189 (1986).

[16] For a concise review, see A. Fujimori and T. Mizokawa, Curr. Opin. Solid State Mater. Sci. **2**, 18 (1997).

[17] "laueX" is a freeware written by Alain Soyer in C language, and designed for UNIX workstations. It requires X-Window and OSF-Motif libraries. The code is available by anonymous ftp at ftp.lmcp.jussieu.fr under the directory pub/sincris/software/general/laueX.

[18] Y. Ueda, private communication.

[19] I. H. Inoue, K. Morikawa, H. Fukuchi, T. Tsujii, F. Iga, and Y. Nishihara, Jpn. J. Appl. Phys. **32**, 451 (1993).

[20] M. Ishikawa, Y. Nakazawa, T. Takabatake, A. Kishi, R. Kato, and A. Maesono, Solid State Comm. **66**, 201 (1988).

[21] T. A. Koopman, Physica **1**, 104 (1933).

[22] C. N. Berglund and W. E, Spicer, Phys. Rev. A **136**, 1030 (1964); *ibid* 1044 (1964).

[23] L. C. Davis, J. Appl. Phys. **59**, R25 (1986); U. Fano, Phys. Rev. **124**, 1866 (1961).

[24] J. C. Fuggle, in *Unoccupied Electronic States*, edited by J. C. Fuggle and J. E. Inglesfield (Splinger-Verlag, Berlin 1992).

[25] I. Lindau and W. E. Spicer, J. Electr. Spectrosc. Relat. Phenom. **3**, 409 (1974).

[26] D. D. Sarma, N. Shanthi, S. R. Barman, N. Hamada, H. Sawada, and K. Terakura, Phys. Rev. Lett., **75**, 1126 (1995).

[27] D.D. Sarma, N. Shanthi, and Priya Mahadevan, Phys. Rev. B **54**, 1622 (1997).

[28] K. Maiti, Priya Mahadevan, and D. D. Sarma, Phys. Rev. Lett. **80**, 2885 (1998).

[29] M.P. Seah and W.A. Dench, Surf. Interface Anal. **1**, 2 (1979).

[30] A. Kotani, in *Handbook of Synchrotron Radiation* **2**, edited by G. V. Marr (Elsevier, Amsterdam 1992).

[31] O. Gunnarson and K. Schönhammer, Phys. Rev. B **28**, 4315 (1983).

[32] The continued fraction expansion is equivalent to the Laurent expansion of the Green's function, *i.e.*, the finite sums over pole contributions. This is generally valid in high energy behavior such as a photoemission response. [see, K. Matho, J. Phys. Chem. Solids **56**, 1735 (1995).]

[33] W. Nolting and W. Borgiel, Phys. Rev. B **39**, 6962 (1989).

[34] K. Matho, private communication.

[35] H. R. Glyde, S. I. Hernádi, Phys. Rev. B **28**, 141 (1983); C. W. Greeff, H. R. Glyde, and B. E. Clements, *ibid* **45**, 7951 (1992).

[36] A. Fukushima, F. Iga, I. H. Inoue, K. Murata, and Y. Nishihara, J. Phys. Soc. Jpn. **63**, 409 (1994).

[37] F. Lichtenberg, D. Widmer, J. G. Bednorz, T. Williams, and A. Reller, Z. Phys. **B82**, 211 (1991); D. A. Crandles, T. Timusk, and J. E. Greedan, Phys. Rev. B **44**, 13250 (1991); D. A. Crandles, T. Timusk, J. D. Garrette, and J. E. Greedan, Physica C **201**, 407 (1992).

[38] Y. Okada, T. Arima, Y. Tokura, C. Murayama and N. Môri, Phys. Rev. B **48**, 9677 (1993).

[39] J. C. Phillips, Phys. Rev. B **46**, 8542 (1992).

[40] N. Shirakawa, K. Murata, H. Makino, F. Iga, and Y. Nishihara, J. Phys. Soc. Jpn. **64**, 4824 (1995).

[41] Z. Hiroi and M. Takano, private communication.

[42] I. Hase (private communication). See also K. Takegahara, J. Electron Spectrosc. Relat. Phenom. **66**, 303 (1994).

[43] A. N. Gerritsen, Physica **25**, 489 (1959).

[44] B. Barbara, V. S. Amaral, J. Filippi, A. G. M. Jansen, J. B. Sousa and J. M. Moreira, J. Appl. Phys. **70**, 5813 (1991).

[45] M. J. Naughton, S. Dickinson, R. C. Samaratunga, J. S. Brooks, and K. P. Martin, Rev. Sci. Instrum. **54** 1529 (1983).

[46] I. H. Inoue, O. Goto, H. Makino, N. E. Hussey, M. Ishikawa, Phys. Rev. B **58**, 4372 (1998).

[47] I. H. Inoue, N. Shirakawa, I. Hase, O. Goto, H. Makino, M. Ishikawa, J. Phys. Condens. Matter (London) **10**, 11541 (1998).

[48] For a recent review, see *Spectroscopy of Mott Insulator and Correlated Metals*, edited by A. Fujimori and Y. Tokura (Springer-Verlag, Berlin, 1995).

[49] Y. Tokura, Y. Taguchi, Y. Okada, Y. Fujishima, T. Arima, K. Kumagai, and Y. Iye, Phys. Rev. Lett. **70**, 2126 (1993).

[50] T. Katsufuji and Y. Tokura, Solid State Phys. **30**, 15 (1995): Y. Okada, Master thesis, University of Tokyo, 1993, unpublished.

[51] Y. Tokura, Y. Taguchi, Y. Moritomo, K. Kumagai, T. Suzuki, and Y. Iye, Phys. Rev. B **48**, 14063 (1993).

[52] F. Iga, Y. Nishihara, J. Sakurai, and M. Ishikawa, Physica B **237-238**, 14 (1997).

[53] J. B. Torrance, P. Lacorre, A. I. Nazzal, E. J. Ansaldo, and Ch. Niedermayer, Phys. Rev. B **45**, 8209 (1992); X. Granados, J. Fontcuberta, X. Obradors, and J. B. Torrance, *ibid.* **46**, 15683 (1992); X. Obradors, L. M. Paulis, B. Maples, J. B. Torrance, A. I. Nazzal, J. Fontcuberta, and Y. Granados, *ibid.* **47**, 12353 (1993); P. C. Canfield, J. D. Thompson, S. -W. Cheong, and L. W. Rupp, *ibid.* **47**, 12357 (1993); J. L. García-Muñoz, J. Rodríguez-Carvajal, and P. Lacorre, *ibid.* **50**, 978 (1994); T. Arima and Y. Tokura, J. Phys. Soc. Jpn. **64**, 2488 (1995).

[54] J. A. Wilson and G. D. Pitt, Philos. Mag. **23**, 1297 (1971); G. Czyzek, J. Fink, H. Schmidt, G. Krill, M. F. Lapierre, P. Paissod, F. Gautier, and C. Robert, J. Magn. Magn. Mater. **3** 58 (1976); S. Ogawa, J. Appl. Phys. **50**, 2308 (1979); H. Takagi, H. Eisaki, S. Uchida, and R. J. Cava, in Ref. 48, p. 185; Y. Sekine, H. Takahashi, N. Môri, T. Matsumoto, and T. Kosaka, Physica B **237-238**, 148 (1997).

[55] J. Zaanen, G.A. Sawatzky, and J.W. Allen, Phys. Rev. Lett. **55**, 418 (1985).

[56] S. Hüfner, Z. Phys. B **61**, 135 (1985).

[57] R. D. Shannon, Acta Crystallogr. A **32**, 751 (1976).

[58] The $GdFeO_3$ type lattice distortion possibly causes anisotropy and affects electron-phonon interactions. However, in this system, these contributions are not predominant for the metallic properties, as revealed by our measurements and the following discussion. This could also justify our claim that the metallic $Ca_{1-x}Sr_xVO_3$ alloy is an ideal compound.

[59] I. H. Inoue, I. Hase, Y. Aiura, A. Fujimori, Y. Haruyama, T. Maruyama, and Y. Nishihara, Phys. Rev. Lett. **74**, 2539 (1995).

[60] M. J. Rozenberg, I. H. Inoue, H. Makino, F. Iga, and Y. Nishihara, Phys. Rev. Lett. **76**, 4781 (1996).

[61] H. Makino, I. H. Inoue, M. J. Rozenberg, I. Hase, Y. Aiura, S. Onari, Phys. Rev. B **58**, 4384 (1998). This article appears in Appendix of this Thesis.

[62] K. Morikawa, T. Mizokawa, K. Kobayashi, A. Fujimori, H. Eisaki, S. Uchida, F. Iga, and Y. Nishihara, Phys. Rev. B **52**, 13711 (1995).

[63] For $D(E_F)$, we have used the LDA DOS at E_F for $CaVO_3$ and $SrVO_3$, and have simply made a linear interpolation for the intermediate Sr/Ca stoichiometries.

[64] J. H. Van Vleck, in *The Theory of Elecronic and Magnetic Susceptibilities* (Oxford University Press, Oxford, United Kingdom, 1932).

[65] H. Kontani and K. Yamada, J. Phys. Soc. Jpn. **65**, 172 (1996).

[66] This term corresponds to the Van Vleck paramagnetism in insulating materials, and becomes large when the "quenching" of the orbital angular moment is not sufficient. Moreover, this term can be enhanced by the electron correlation, since electron correlations change the electron configuration as well as the crystal field, and the Van Vleck term cannot be treated by a one-body approximation. The x-dependence of the fourth term in the $Ca_{1-x}Sr_xVO_3$ system is still an open question: see *e.g.*, H. Kontani and K. Yamada, J. Phys. Soc. Jpn. **65**, 172 (1996).

[67] J. P. Pouget, H. Launois, T. M. Rice, P. Derrier, A. Gossard, G. Villeneuve, and P. Hagenmuller, Phys. Rev. B **10**, 1801 (1974).

[68] J. -S. Zhou and J. B. Goodenough, Phys. Rev. B **54**, 13393 (1996).

[69] K. Wilson, Rev. Mod. Phys. **47**, 773 (1975).

[70] P. Nozières, J. Low Temp. Phys. **17**, 31 (1974).

[71] A. Yoshimori, Prog. Theor. Phys. **55**, 67 (1976).

[72] Even in the case where only the on-site Coulomb interaction is included in the model Hamiltonian, the self-energy can be nonlocal (momentum dependent). For example, the effect of antiferromagnetic fluctuation due to Fermi surface nesting has already been discussed in the literature: A. Kampf and J. R. Schrieffer, Phys. Rev. B **41**, 6399 (1990); M. Langer, J. Schmalian, G. Grabowsky, and K. H. Bennemann, Phys. Rev. Lett. **75**, 4508 (1995); J. J. Deisz, D. W. Hess, and J. W. Serene, *ibid* **76**, 1312 (1996).

[73] A. Fujimori, K. Morikawa, T. Mizokawa, T. Saitoh, M. Nakamura, Y. Tokura, I. Hase, and I. H. Inoue, in Ref. 48, p. 174.

[74] Ashcroft N W and Mermin N D 1987 *Solid State Physics: HRW International Edition* (Hong Kong: Saunders College / CBS Publishing Asia Ltd.) p 334

[75] T. Hirano and M. Kaise, J. Appl. Phys. **68**, 627 (1990).

[76] E. Hashimoto, Y. Ueda, H. Tamura, and T. Kino, J. Phys. Soc. Jpn. **62**, 4178 (1993).

[77] B. R. Watts, J. Phys. F **17**, 1703 (1987).

[78] When the rate of crystal growth is fairly large, it is hard to explain this process on a plane by plane basis. However, if the crystal contains a screw dislocation, it is never necessary to nucleate a new plane, as the local planar structure can wind endlessly about the screw dislocation. This kind of process might be realized in some cases during our crystal growth.

[79] S. Koshino, Prog. Theor. Phys. **24**, 1049 (1960); *ibid* **30**, 415 (1963); P. L. Tayler, Phys. Rev. **135**, A1333 (1964); Yu. Kagán and A. P. Zhernov, Zh. Eksp. Teor. Fiz. **50**, 1107 (1966) [Sov. Phys. JETP **23**, 737 (1966)]; D. H. Damon, M. P. Mathur, and P. G. Klemens, Phys. Rev. **176**, 876 (1968); H. Takayama, Z. Phys. **263**, 329 (1973); P. J. Cote and L. V. Meisel, Phys. Rev. Lett. **39**, 102 (1977); F. J. Ohkawa, J. Phys. Soc. Jpn. **44**, 1105 (1978).

[80] M. Gurvitch, Phys. Rev. Lett. **56**, 647 (1986).

[81] B. Bucher, P. Steiner, J. Karpinski, E. Kaldis, and P. Wachter Phys. Rev. Lett. **70**, 2012 (1993).

[82] In strongly correlated electron systems, the electron-electron scattering is the dominant process to induce incoherence of the wave function, which thus determines the relaxation time τ under the presence of the umklapp process. Then, the quasiparticle – quasiparticle scattering time is given by $\tau^{-1} \propto Z^{-1}\mathrm{Im}\Sigma$, where Z is the quasiparticle weight and Σ is the self-energy.

[83] K. Kadowaki and S. B. Woods, Solid State Commun. **58**, 507 (1986).

[84] N. G. Ptitsina, G. M. Chulkova, K. S. Il'in, A. V. Sergeev, F. S. Pochinkov, E. M. Gershenzon, and M. E. Gershenson, Phys. Rev. B **56**, 10089 (1997), and references therein.

[85] When we apply a hydrostatic pressure up to 8 GPa to $CaVO_3$, the resistance at room temperature decreases by $\sim$30 % monotonically: F. Iga (unpublished).

[86] Preliminary results of inverse photoemission obtained by the collaboration with D. D. Sarma and K. Maiti.

[87] Y. Okimoto, T. Katsufuji, Y. Okada, T. Arima, and Y. Tokura, Phys. Rev. B **51**, 9581 (1995).

[88] P. Lombardo, J. Schmalian, M. Avignon, and K. H. Bennemann, Physica B **230-232**, 415 (1997).

[89] I. H. Inoue, I. Hase, Y. Aiura, A. Fujimori, K. Morikawa, T. Mizokawa, Y. Haruyama, T. Maruyama, and Y. Nishihara, Physica C **235-240**, 1007 (1984).

[90] I. H. Inoue, H. Makino, I. Hase, Y. Aiura, Y. Haruyama, and Y. Nishihara, Physica B **230-232**, 780 (1997).

[91] A. Fujimori, I. Hase, H. Namatame, Y. Fujishima, Y. Tokura, H. Eisaki, S. Uchida, K. Takegahara, and F. M. F. de Groot, Phys. Rev. Lett. **69**, 1796 (1992).

[92] A. Georges, G. Kotliar, W. Krauth and M. J. Rozenberg, **68**, 13 (1996), and references therein.

[93] W. Metzner and D. Vollhardt, Phys. Rev. Lett. **62**, 324 (1989).

[94] M. Jarrell, J. K. Freericks and Th. Pruschke, Phys. Rev. B **51**, 11704 (1995).

[95] A. Yagishita and E.Shigemasa, Rev. Sci. Instrum. **63**, 1383 (1992); A. Yagishita, S. Masui, T. Toyoshima, H. Maezawa, and E.Shigemasa, Rev. Sci. Instrum. **63**, 1351 (1992)

[96] K. Morikawa, Thesis (University of Tokyo, 1995).

[97] D. A. Shirley, Phys. Rev. B **5**, 4709 (1972).

[98] S. Tougaard, Surface and Interface Analysis **11**, 453 (1988), and the references therein.

[99] M. O. Klause and J.H. Oliver, J. Phys. Chem. Ref. Data **8**, 329 (1979)

[100] For more precise analysis, it is necessary to take into account the overlapping plasmon-loss satellites accompanying the photoemission peaks, because these satellites may affect the results of the line-shape analysis to some extent. The energy and the width of the plasmon peak can be obtained from the electron energy loss spectrum. This remains for the future investigation.

[101] H. Pen, Thesis (University of Groningen, 1997).

[102] Pen proposed that the presence of the O 1s core hole may pull the spectral weight towards the lower edge of the t_{2g} and e_g bands, and this effect may be significant for the e_g band.[101]

[103] M. Abbate, J. B. Goedkoop, F. M. F. de Groot, M. Grioni, J. C. Fuggle, S. Hofmann, H. Petersen, and M. Sacchi, Surf. Intl. Anal. **18**, 65 (1992).

[104] E. Müller-Hartmann, Int. J. Mod. Phys. B **3**, 2169 (1989).

[105] G.Tréglia, F. Ducastelle, and D. Spanjaard, J.Phys. (Paris) **43**, 341 (1982).

[106] K. Morikawa *et al.* estimated the ω-mass of $CaVO_3$ and $SrVO_3$ in this way.[62] The values are roughly equal to the values obtained in this study.

[107] Since the system is metallic, U/W should be less than 1. This discrepancy is due to the naive estimation assuming that the $3d$ band is symmetric with regard to E_F.

[108] I. H. Inoue, I. Hase, Y. Aiura, Y. Haruyama, Y. Nishihara, A. Fujimori, S. Nishizaki, Y. Maeno, T. Fujita, F. Lichtenberg, and J. G. Bednorz, in Proceedings of International Conference of Physical Phenomena on High Magnetic Field II (PPHMF-II), Tallahassee, May 1995. (World Scientific, Singapore, 1996).

[109] I. H. Inoue, Y. Aiura, Y. Nishihara, Y. Haruyama, S. Nishizaki, Y. Maeno, T. Fujita, J. G. Bednorz, and F. Lichtenberg, Physica B **223&224**, 516 (1996).

[110] I. H. Inoue, Y. Aiura, Y. Nishihara, Y. Haruyama, S. Nishizaki, Y. Maeno, T. Fujita, J. G. Bednorz, and F. Lichtenberg, J. Electron Spectrosc. Relat. Phenom. **78**, 175 (1996).

[111] The fundamental differences of the electronic states between the cuprates and Sr_2RuO_4 are:

- Doping is necessary to realize the superconductivity in the cuprates, while Sr_2RuO_4 is superconducting without any carrier doping.
- In the cuprates, Cu $e_g(3d_{x^2-y^2})$ and O $2p\sigma$ bonding orbitals are relevant, while the antibonding Ru $t_{2g}(3d_{xy}, 3d_{yz}, 3d_{zx})$ and O $2p\pi$ orbitals are important in Sr_2RuO_4.
- Cu^{2+} ($3d^9$) valence state has spin 1/2, while Ru^{4+} ($4d^4$) is in a state with spin 1.

[112] Y. Maeno, H. Hashimoto, K. Yoshida, S. Nishizaki, T. Fujita, J. G. Bednorz, and F. Lichtenberg, Nature **372** 532 (1994).

[113] A. P. Mackenzie, R. K. W. Haselwimmer, A. W. Tyler, G. G. Lonzarich, Y. Mori, S. Nishizaki, and Y. Maeno, Phys. Rev. Lett. **80**, 161 (1998). The impurity-free intrinsic T_c of 1.5 K was suggested in this paper. Very recently, crystals that in fact exhibit $T_c = 1.50$ K have been obtained.

[114] Y. Maeno, K. Yoshida, H. Hashimoto, S. Nishizaki, S. Ikeda, M. Nohara, T. Fujita, A. P. Mackenzie, N. E. Hussey, J. G. Bednorz, and F. Lichtenberg, J. Phys. Soc. Jpn. **66**, 1405 (1997).

[115] K. Yoshida, Y. Maeno, S. Nishizaki, S. Ikeda, T. Fujita, J. Low Temp. Phys. **105**, 1593 (1996).

[116] N. Shirakawa, K. Murata, Y. Nishihara, S. Nishizaki, Y. Maeno, T. Fujita, J. G. Bednorz, F. Lichtenberg, N. Hamada, J. Phys. Soc. Jpn. **64** 1072 (1995).

[117] A. P. Mackenzie, S. R. Julian, A. J. Diver, G. J. McMullan, M. P. Ray, G. G. Lonzarich, Y. Maeno, S. Nishizaki, and T. Fujita, Phys. Rev.

Lett. **76**, 3786 (1996); *ibid* **78**, 2271 (1997); A. P. Mackenzie, S. Ikeda, Y. Maeno, T. Fujita, S. R. Julian and G. G. Lonzarich, J. Phys. Soc. Jpn. **67**, 385 (1998).

[118] N. E. Hussey, A. P. Mackenzie, J. R. Cooper, Y. Maeno, S. Nishizaki, and T. Fujita, Phys. Rev. B **57**, 5505 (1998).

[119] A. P. Mackenzie, N. E. Hussey, A. J. Diver, S. R. Julian, Y. Maeno, S. Nishizaki, and T. Fujita, Phys. Rev. B **54**, 7425 (1996).

[120] T. M. Rice and M. Sigrist, J. Phys. Condens. Matter **7**, L643 (1995).

[121] M. Cuoco, C. Noce, and A. Romano, Phys. Rev. B **57**, 11989 (1998).

[122] M. Sigrist and M. E. Zhitomirsky, J. Phys. Soc. Jpn. **65**, 3452 (1996).

[123] K. Machida, M. Ozaki, and T. Ohmi, J. Phys. Soc. Jpn. **65**, 3720 (1996).

[124] G. Baskaran, Physica B **223&224**, 490 (1996).

[125] D.F. Agterberg, T. M. Rice, abd M. Sigrist, Phys. Rev. Lett. **78**, 3374 (1997).

[126] I. I. Mazin and D. J. Singh, Phys. Rev. Lett. **79**, 161 (1997).

[127] K. Ishida, Y. Kitaoka, K. Asayama, S. Ikeda, S. Nishizaki, Y. Maeno, K. Yoshida, and T. Fujita, Phys. Rev. B **56**, R505 (1997).

[128] Y. Maeno, S. Nishizaki, K. Yoshida, S. Ikeda, and T. Fujita, J. Low Temp. Phys. **105**, 1577 (1997); S. Nishizaki, Y. Maeno, S. Farner, S. Ikeda, and T. Fujita, J. Phys. Soc. Jpn. **67**, 560 (1998).

[129] N. Shirakawa, K. Murata, S. Nishizaki, Y. Maeno, and T. Fujita, Phys. Rev. B **56**, 7890 (1997).

[130] K. Yoshida, Y. Maeno, S. Nishizaki, and T. Fujita, Physica C **263**, 519 (1996).

[131] G. M. Luke, Y. Fudamoto, K. M. Kojima, M. I. Larkin, J. Merrin, B. Nachumi, Y. J. Uemura, Y. Maeno, Z. Q. Mao, Y. Mori, H. Nakamura, and M. Sigrist, Nature, **394**, 558 (1998).

[132] T. Oguchi, Phys. Rev. B **51**, 1385 (1995).

[133] D. J. Singh, Phys. Rev. B **52**, 1358 (1995).

[134] I. Hase and Y. Nishihara, J. Phys. Soc. Jpn. **66**, 1405 (1997).

[135] T. Yokoya, A. Chainani, T. Takahashi, H. Katayama-Yoshida, M. Kasai, and Y. Tokura, Phys. Rev. Lett. **76**, 3005 (1996); T. Yokoya, A. Chainani, T. Takahashi, H. Ding, J. C. Campuzano, H. Katayama-Yoshida, M. Kasai, and Y. Tokura, Phys. Rev. B **54**, 13311 (1996).

[136] D. H. Lu. M. Schmidt, T. R. Cummins, S. Schuppler, F. Lichtenberg, and J. G. Bednorz, Phys. Rev. Lett. **76**, 4845 (1996).

[137] Y. Maeno, private communication.

[138] T. Yokoya, A. Chainani, T. Takahashi, H. Katayama-Yoshida, M. Kasai, Y. Tokura, N. Shanthi, and D. D. Sarma, Phys. Rev. B **53**, 8151 (1996).

[139] M. Schmidt, T. R. Cummins, M. Bürk, D. H. Lu, N. Nücker, S. Schuppler, and F. Lichtenberg, Phys. Rev. B **53**, R14761 (1996).

[140] J. J. Yeh and I. Lindau, Atomic Data and Nuclear Data Tables **32**, 1 (1985).

[141] Validity of the subtraction is debatable, so we note here that we have done the analyses under this assumption for the background.

[142] Since $\Sigma(\omega, \vec{k})$ should be analytic in the lower half of the ω-plane, one of the necessary conditions is $s_2 = \sqrt{-\alpha}\omega_3$.

Appendix. Optical Conductivity of $Ca_{1-x}Sr_xVO_3$

This chapter has been published by Phys. Rev. B **58**, *4384 (1998) by H. Makino, I. H. Inoue, M. J. Rozenberg, I. Hase, Y. Aiura, and S. Onari.*

Optical conductivity spectra of single crystals of the perovskite-type $3d^1$ metallic alloy system $Ca_{1-x}Sr_xVO_3$ have been studied to elucidate how the electronic behavior depends on the strength of the electron correlation without changing the nominal number of electrons. The reflectivity measurements were made at room temperature between 0.05 eV and 40 eV. The effective mass deduced by the analysis of the Drude-like contribution to the optical conductivity and the plasma frequency do not show critical enhancement, even though the system is close to the Mott transition. Besides the Drude-like contribution, two anomalous features of the intraband transition within the 3*d* band were observed in the optical conductivity spectra. These features can be assigned to transitions involving the incoherent and coherent bands near the Fermi level. The large spectral weight redistribution in this system, however, does not involve a large mass enhancement.

A.1. Introduction

Over the past few decades, a considerable number of studies have been performed on 3*d* transition-metal oxides which have a considerably narrow 3*d* band. In particular, a metal-to-insulator transition caused by a strong electron correlation[1] (Mott transition) as well as anomalous electronic properties in the metallic phase near the Mott transition have attracted the interest of many researchers. Since the discovery of the high-T_c cuprate superconductors, there has been much discussion relating to the importance of two different experimental approaches to the Mott transition, namely a filling control and a band-width control. The former involves doping holes or electrons into the system, and the latter varying the strength of the electron correlation U/W, where U is the electron correlation due to Coulomb repulsion and W is the one-electron band-width.

In recent years, the systematic evolution of optical conductivity spectra in going from a correlated metallic phase to the Mott-Hubbard insulating phase have been reported on both the filling controlled[2-6] and the band-width controlled Mott-Hubbard systems.[7-10] The smallest energy gap for charge excitations of the Mott-Hubbard insulator is the excitation energy of the charge fluctuation $d^n + d^n \rightarrow d^{n-1} + d^{n+1}$, so-called a Mott-Hubbard gap.[11] The optical conductivity of the Mott-Hubbard insulator is considered to show a gap feature due to the above charge excitation from the lower Hubbard band to the upper Hubbard band.

V_2O_3 and related compounds have been ex-

tensively studied as typical materials which show the Mott transition with varying the strength of the U/W ratio. The temperature dependent optical conductivity of V_2O_3 was reported by Thomas *et al.* through the metal-to-insulator transition.[9,10] The optical conductivity of V_2O_3 in the insulating phase shows a gap feature, which is attributed to the Mott-Hubbard gap excitation. On the other hand, in the metallic state, a low-energy contribution to the optical conductivity shows an anomalous feature, which is reproduced by two Lorenzians. Moreover, the optical conductivity shows an anomalous enhancement of the spectral weight as a function of temperature. Rozenberg *et al.* reported that these experimental results are in good agreement with the theoretical prediction obtained by the infinite-dimension Hubbard model within the mean-field approach.[10] Since the formation of the Mott-Hubbard bands are predicted even in the metallic state for this kind of strongly correlated system, the optical conductivity spectra should be affected by the precursor features.[12] It is very interesting to see how the spectral weight varies with the electron correlation in the correlated metallic state near the Mott transition. For a detailed discussion, however, we need to control the strength of the electron correlation more precisely.

The perovskite-type early $3d$ transition-metal oxides are ideal Mott-Hubbard systems for controlling the band filling and band-width by chemical substitutions. It has been reported that, for the filling controlled systems $La_{1-x}Sr_xTiO_3$ and $R_{1-x}Ca_xTiO_3$ (R=rare earth), the spectral weight of the optical conductivity transfers from the higher energy feature corresponding to an excitation through the Mott-Hubbard gap, to the mid-infrared inner-gap region corresponding to the Drude-like absorption extending from $\omega = 0$.[2,3,6] The rate of the spectral weight transfer by doping increases systematically with the increase of the one-electron band-width W.

On the other hand, the Ti–O–Ti bond angle can be decreased as we decrease the ionic radius of the R site. The decrease of the Ti–O–Ti bond angle gives rise to the decrease of the value of W. A systematic change of the optical conductivity spectra was reported on $RTiO_3$ (R=La, Ce, Pr, Nd, Sm, and Gd).[7] The lowest gap-like feature systematically increases as the ionic radius of the R site decreases, namely, as the value of W decreases. A similar change was also observed on an alloy system, $La_{1-x}Y_xTiO_3$.[8] These systematic variations of the optical conductivity are interpreted as a successive increase of the Mott-Hubbard gap with increasing the strength of the U/W ratio. In these materials, however the system remains an insulator even for the least correlated $LaTiO_3$; therefore one cannot study the evolution of the metallic properties under the band-width control in this system.

The purpose of this chapter is to clarify the evolution of the optical conductivity spectrum in the metallic phase near the Mott transition, as we control the strength of the electron correlation U/W without changing the band filling. A perovskite-type $3d^1$ vanadate $CaVO_3$ is considered to be a strongly correlated metal close to the Mott transition.[13,14] We can control the strength of the U/W ratio, by chemical substitution of a Sr ion for a Ca ion of the same valence without varying the nominal $3d$-electron number per vanadium ion.[15] We report the optical conductivity spectra in this strongly correlated alloy system $Ca_{1-x}Sr_xVO_3$. The effective mass m^*/m_b estimated from the optical measurements are shown in Sec. A.3.2. The evolution of the optical conductivity is discussed in Sec. A.3.3.

A.2. Experiments

Single crystals of $Ca_{1-x}Sr_xVO_3$ (x=0, 0.25, 0.5, 1) were grown by a floating-zone method using an infrared image furnace with double halogen lamps. Since as-grown samples are slightly oxygen deficient, all the samples were annealed in air at 200 °C for 24 hours in order to make the oxygen concentration stoichiometric.[13,16,17]

Raman scattering spectra were measured at room temperature in back-scattering geometry using a triple spectrometer system (Jasco TRS-600) equipped with a charge coupled device (CCD; Photometrics TK512CB) cooled by liquid nitrogen. The samples were excited by the 514.5 nm Ar ion laser line. Polarization of the incident light was taken to be parallel to that of the scattered light.

Optical reflectivity measurements were carried out at room temperature ($\sim$300 K) in the energy range between 0.05 eV and 40 eV using a Michelson-type Fourier-transform infrared spectrometer (0.05–0.6 eV), a grating monochromator (0.5–5.6 eV), and a Seya-Namioka-type grating for the synchrotron radiation (5–40 eV) at the beamline BL-11D of Photon Factory, Tsukuba. The surfaces of the samples were mechanically polished with diamond paste for the optical measurements. The absolute reflectivity was determined by referring to the reflectivity of an Al or Ag film which was measured at the same optical alignment.

We have calculated a complex dielectric function $\epsilon(\omega) \equiv \epsilon_1(\omega)+i\epsilon_2(\omega)$ by the Kramers-Kronig (K-K) transformation of the measured reflectivity $R(\omega)$, where ω is the photon energy. The real part of the complex optical conductivity $\mathrm{Re}[\tilde{\sigma}(\omega)]$ is related to the imaginary part of the dielectric function $\epsilon_2(\omega)$ by $\mathrm{Re}[\tilde{\sigma}(\omega)] = (\omega/4\pi)\epsilon_2(\omega)$. Since the K-K analysis requires $R(\omega)$ for $0 < \omega < \infty$, two assumptions must be made to extrapolate the observed data beyond the upper and lower bounds of the measurements. In the present study, the reflectivity data were first extrapolated from the lowest measured energy down to $\omega = 0$ with the Hagen-Rubens formula which is an approximation for $R(\omega)$ of conventional metals. Then, beyond the highest measured energy, the reflectivity data were extrapolated up to $\omega \to \infty$ with an asymptotic function of ω^{-4}.

A.3. Results and discussion

A.3.1. Band-width control due to orthorhombic distortion

Powder x-ray diffraction measurements were carried out to characterize the samples and to determine the lattice constants. In Fig. 7.1, we present the lattice constants, a, b, and c against the Sr content x. The crystal structure of $Ca_{1-x}Sr_xVO_3$ belongs to the perovskite-type structure with orthorhombic distortion ($GdFeO_3$-type).[18] The amount of the distortion is almost proportional to the amount of the Ca content; *i.e.*, $SrVO_3$ is a cubic perovskite. However, we assumed the crystal structure of all samples ($0 \le x \le 1$) to be orthorhombic and deduced the lattice constants. The lattice constants increase monotonically with the increase of x, ensuring the

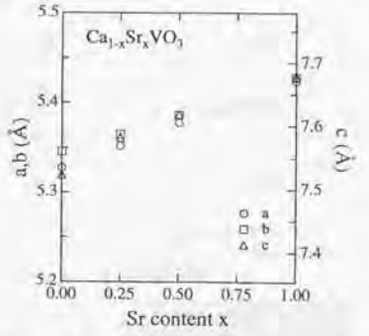

FIG. 7.1. Lattice constants, a, b, and c of the $Ca_{1-x}Sr_xVO_3$ single crystals plotted against the Sr content x. The data were estimated from powder x-ray diffraction patterns.

appropriate formation of the solid solution over the whole composition range.

Raman scattering measurements give indirect information about the crystal symmetry, because the appearance of some Raman-active phonon lines depends crucially on the crystal symmetry of the system. In Fig. 7.2, we show the Raman spectra of $Ca_{1-x}Sr_xVO_3$ at room temperature in the wave-number range of 80–400cm^{-1}. In this wave-number range,

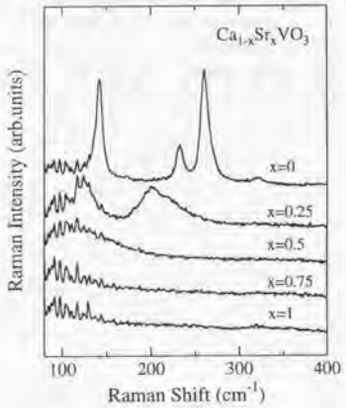

FIG. 7.2. Raman spectra of $Ca_{1-x}Sr_xVO_3$ at room temperature. Polarization of the incident light was taken to be parallel to that of the scattered light.

four Raman active A_g phonon lines are observed in orthorhombic $CaVO_3$ ($x = 0$). The energies of the phonon lines shift to the lower energy side, and the width of the peaks become broader, as we increase the Sr content x. The Raman active phonon lines disappear completely in $SrVO_3$.

According to the group theory analysis,[19] it is predicted that several Raman active phonon modes $7A_g + 7B_{1g} + 5B_{2g} + 5B_{3g}$ can exist in the orthorhombically distorted perovskite which belongs to the point group symmetry of D_{2h}. On the other hand, the cubic perovskite which belongs to the point group symmetry of O_h is "Raman forbidden", namely it has no Raman-active phonon modes. Therefore, the experimental results tell us that the crystal symmetry actually changes from the orthorhombic distorted perovskite ($CaVO_3$) to the cubic perovskite ($SrVO_3$). The orthorhombic to cubic transition is considered to occur between $x = 0.5$ and 0.75.

The orthorhombic distortion implies that the V–O–V bond angle is deviated from 180°, *i.e.*, there is an alternately tilting network of the VO_6 octahedra. The V–O–V bond angle of $SrVO_3$ is 180° same as an ideal perovskite structure, while that of $CaVO_3$ is $\sim 160°$. The bond angle deviation from 180° reduces the overlap between the neighboring V $3d$ orbital mediated by the O $2p$ orbital. Therefore, the one-electron band-width W of V $3d$ band decreases with decreasing the V–O–V bond angle. Accordingly, we can control the value of W by chemical substitution of the Ca^{2+} ion for the Sr^{2+} ion of the same valence without varying the nominal $3d$-electron number per vanadium ion. Since the electron correlation energy U is almost the same in $CaVO_3$ and $SrVO_3$, we can thus control the strength of the U/W ratio by chemical substitution. The V–O–V bond angle of $CaVO_3$, in addition, is almost equal to that of $LaTiO_3$ which is a Mott-Hubbard type insulator, so that it seems reasonable to consider that $CaVO_3$ is close to the Mott transition. Moreover, there is considerable evidence for the presence of strong electron correlations.[13–17] Thus, $Ca_{1-x}Sr_xVO_3$ system is ideal for the study of the metallic states near the Mott transition.

A.3.2. Effective mass

In Fig. 7.3, we show optical reflectivity spectra of $Ca_{1-x}Sr_xVO_3$ measured at room temperature (~300 K), for four single crystals with different x (x=0, 0.25, 0.50, 1). The chemical substitution of Sr^{2+} for Ca^{2+} seems

to make no remarkable change at the lower-energy region (below ~5 eV) in the optical reflectivity spectra. All the samples exhibit high reflectivity from far-infrared to near-infrared region, and we can recognize a sharp reflectivity edge appearing at ~1.3 eV. Since $Ca_{1-x}Sr_xVO_3$ is metallic over the whole composition range, the optical reflectivity is dominated by the signal of conduction electrons in this photon energy region. Systematic spectral changes with x are observed in the energy range of the ultra-violet and vacuum-ultra-violet light. The changes are partly due to the differences in the conduction bands of the Ca^{2+} and Sr^{2+} cations. But this is irrelevant for the discussion of the main subject.

First of all, we will concentrate on the low energy response of the itinerant carriers. The contribution of the conduction electrons to the

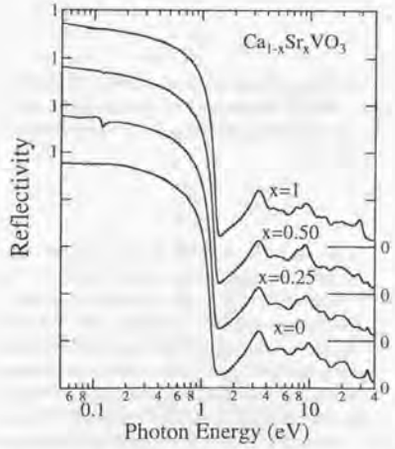

FIG. 7.3. Reflectivity spectra for the $Ca_{1-x}Sr_xVO_3$ single crystals measured at room temperature. The feature at ~0.1 eV for $x = 0.25$ is an experimental artifact.

complex dielectric function $\epsilon(\omega)$ is well described by the Drude model. According to the generalized Drude model,[20,21] $\epsilon(\omega)$ is expressed as

$$\epsilon(\omega) = \epsilon_\infty - \frac{4\pi\tilde{\sigma}(\omega)}{i\omega} \equiv \epsilon_\infty - \frac{\omega_p^2(\omega)}{i\omega(\gamma(\omega) - i\omega)}, \quad \text{(A.1)}$$

where ϵ_∞ is the high-energy dielectric constant, which is a high-energy contribution of the interband transitions, $\tilde{\sigma}(\omega)$ is the complex conductivity, $\gamma(\omega)$ is the energy-dependent scattering rate, and $\omega_p(\omega)$ is the plasma frequency. The plasma frequency $\omega_p(\omega)$ is defined as

$$\omega_p^2(\omega) \equiv \frac{4\pi n e^2}{m^*(\omega)},$$

where n is the total density of conduction electrons, and $m^*(\omega)$ is the energy-dependent effective mass.

To begin, let us confine our attention to the plasma frequency. If we assume that the nominal electron number per vanadium ion is exactly 1 for the whole composition range, we can deduce the carrier density n from the unit-cell volume. Then, we can estimate a variation of the effective mass $m^*(\omega)$ from the value of $\omega_p(\omega)$.

The Energy-loss function $\mathrm{Im}(-1/\epsilon)$ is obtained by Kramers-Kronig analysis of the measured reflectivity spectra $R(\omega)$. Provided that $\gamma(\omega)$ and $m^*(\omega)$ do not depend on ω strongly, we can estimate $\omega_p(= const.)$ from the Energy-loss function, because, the Energy-loss function peaks at the energy of ω_p^* ($\omega_p^* = \omega_p/\sqrt{\epsilon_\infty}$). Accordingly, we can obtain the energy-independent plasma frequency ω_p from the peak position of the energy-loss function.

In Fig. 7.4, the spectra of $\mathrm{Im}(-1/\epsilon)$ of $Ca_{1-x}Sr_xVO_3$ are shown in the photon energy range from 0.6 to 2.0 eV to focus on the peak near the reflectivity edge (around

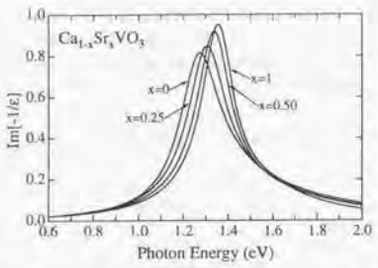

FIG. 7.4. Energy-loss function $\mathrm{Im}[-1/\epsilon(\omega)]$ obtained by the Kramers-Kronig transformation of the reflectivity data. The data in the photon energy range between 0.6 eV and 2.0 eV are shown to focus on the plasmon peak (around 1.3 eV).

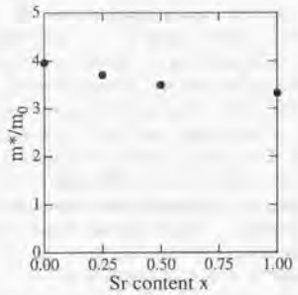

FIG. 7.5. Effective mass m^* estimated by the plasma frequencies compared with the bare electron mass m_0. The value of m^*/m_0 systematically increases in going from $SrVO_3$ ($x = 1$) to $CaVO_3$ ($x = 0$).

1.3 eV). The peak position of the Energy-loss function ω_p^* systematically shifts to higher energy with increasing x. At first, we have estimated ω_p^* from the peak energy, and deduced $\omega_p = \sqrt{\epsilon_\infty}\omega_p^*$. If we consider only the response of the conduction electrons, ϵ_∞ is the contribution from the high-energy interband transitions. Since the interband transition appeared above ~ 2.5 eV, the value of ϵ_∞ can be taken from the real part of the dielectric function $\epsilon_1(\omega)$ at around 2.5 eV.[22] Then, we can deduce the value of m^*/m_b using the lattice constants and the value of ω_p.

In Fig. 7.5, the ratios of the deduced effective mass m^* to the bare electron mass m_0 are plotted as a function of the Sr content x. The value of m^*/m_0 systematically increases as varying x from $SrVO_3$ to $CaVO_3$. This carrier-mass enhancement, however, is not so large, even though the system is near the Mott transition. This result is consistent with the value of m^*/m_b estimated from the results of the specific heat measurements.[14]

It is instructive to compare the measured low frequency $\tilde{\sigma}(\omega)$ with the simple Drude model, in which $\gamma(\omega)$ and $m^*(\omega)$ do not depend on ω. According to Eq. (A.1), the real part of the optical conductivity $\mathrm{Re}[\tilde{\sigma}(\omega)] \equiv \sigma(\omega)$ is given by the formula

$$\sigma(\omega) = \frac{\sigma_{dc}}{1+\omega^2/\gamma^2},$$

where σ_{dc} is the dc conductivity. The dc conductivity is expressed by the scattering rate γ and the plasma frequency ω_p by the following relation:

$$\sigma_{dc} = \frac{ne^2}{m^*\gamma} = \frac{\omega_p^2}{4\pi\gamma}.$$

Here, we have used the value of σ_{dc} obtained by electric resistivity measurements at room temperature. Then the value of γ can be deduced from the above relation. Fig. 7.6 shows the comparison of the experimentally obtained $\sigma(\omega)$ for $CaVO_3$ to the optical conductivity calculated by the simple Drude model. As shown in Fig. 7.6, the low-energy contribution to the optical conductivity, which is a response of the itinerant carriers, is not properly reproduced with this simple Drude model. As we increase the photon energy, the experimentally obtained $\sigma(\omega)$ deviates from that of the simple Drude model. The observed $\sigma(\omega)$ has a

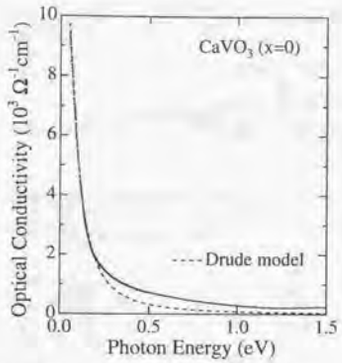

FIG. 7.6. Comparison between the optical conductivity calculated by the simple Drude model and that of the experiment of $CaVO_3$.

tail decaying slower than the Drude-type ω^{-2} dependence.

We consider that the discrepancy between the simple Drude model and the experimental results is attributed to the energy-dependence of the scattering rate $\gamma(\omega)$ and the effective mass $m^*(\omega)$. We can determine $\gamma(\omega)$ and $m^*/m_b(\omega)$ from Eq. (A.1); *i.e.*, when we define $\epsilon(\omega) \equiv \epsilon_1(\omega) + i\epsilon_2(\omega)$,

$$\gamma(\omega) = \frac{\omega\epsilon_2(\omega)}{\epsilon_\infty - \epsilon_1(\omega)},$$

$$m^*(\omega) = \frac{4\pi e^2 n\gamma(\omega)}{\epsilon_2(\omega)\,\omega\,(\gamma^2(\omega)+\omega^2)}.$$

Figs. 7.7(a) and 7.7(b) show $\gamma(\omega)$ and $m^*(\omega)$ of $Ca_{1-x}Sr_xVO_3$ as a function of photon energy. In case of the simple Drude model, the scattering rate γ is taken to be independent on the photon energy. But, in this system, $\gamma(\omega)$ actually increases as we increase the photon energy, as shown in Fig. 7.7(a).

The energy-dependent scattering rate is generally attributed to electron-phonon scattering or electron-electron scattering. Since an

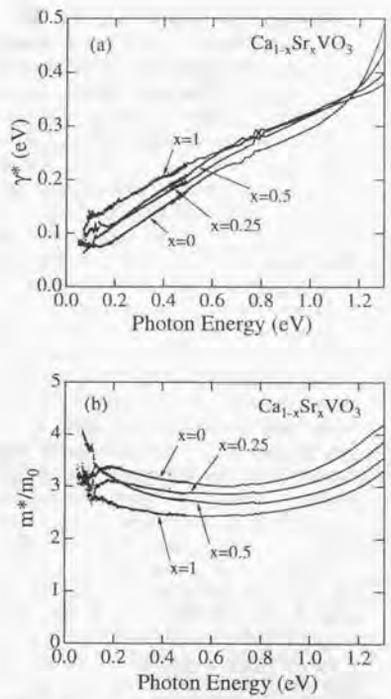

FIG. 7.7. (a) Energy dependent scattering rates $\gamma(\omega)$ of $Ca_{1-x}Sr_xVO_3$; (b) effective mass $m^*(\omega)$ of $Ca_{1-x}Sr_xVO_3$. $m^*(\omega)$ is normalized to the bare electron mass m_0.

extremely large T^2-dependence of the dc conductivity observed in the $Ca_{1-x}Sr_xVO_3$ system can be well ascribed to electron-electron scattering,[14] it is reasonable to consider that electron-electron scattering governs the behavior of $\gamma(\omega)$. According to the Fermi liquid theory, the electron-electron scattering rate is proportional to ω^2. Fig. 7.7(a), however, indicates that $\gamma(\omega)$ looks more proportional to ω rather than ω^2. On the contrary, since the

electron-phonon scattering is proportional to ω^5 up to the Debye frequency, it is necessary to elucidate the scattering process which contributes to $\gamma(\omega)$. This is still an open question.

On the other hand, the energy dependence of $m^*(\omega)$ is not so large. Except for the low energy region ($\omega <\sim 0.2$ eV), the value of $m^*/m_b/m_0$ increases with the decrease of Sr content x. In the $Sr_{1-x}La_xTiO_3$ system, which is a typical doping system, as one approaches $x = 1$, a large energy dependence of m^*/m_b as well as a critical enhancement at the low-energy region are observed.[2] However, in $Ca_{1-x}Sr_xVO_3$ system, m^*/m_b does not exhibit such a critical enhancement with varying x in going from $SrVO_3$ to $CaVO_3$, although there is a difference between the filling control and the band-width control.

In the low energy limit ($\omega = 0$), m^* should correspond to the effective mass estimated by the specific heat measurement. We have interpolated $m^*/m_b(\omega)$ down to $\omega = 0$ with two kinds of tangential lines drawn from 0.4 eV and 0.15 eV. As shown in Fig. 7.8(a), the intercepts, at which the two tangential lines from 0.4 eV and 0.15 eV cut the vertical axis, are defined as m_a and m_b. Fig. 7.8(b) indicates x-dependence of the values of m_a and m_b. The value of m_b does not show any systematic behavior, presumably because phonons, randomness, or other extrinsic contributions cause this non-systematic change. However, the value of m_a increases systematically with decreasing x; moreover, the values are almost equal to the value of m^* deduced from plasma frequency. We regard m_a as a good measure of m^*/m_0 for this system.

The effective mass estimated from the plasma frequencies and the generalized Drude analysis (m_a) appear in Table 7.I. It is expected that we should observe, near the Mott transition, a critical enhancement of the effective mass of the $3d$ conduction electrons. If we substitute the Ca^{2+} ion for the Sr^{2+} ion in the $Ca_{1-x}Sr_xVO_3$ system, the $3d$ band-

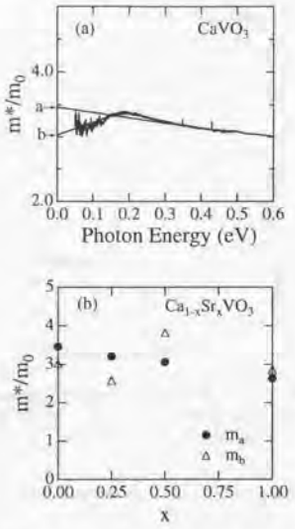

FIG. 7.8. (a) Energy dependent effective mass $m^*(\omega)$ of $CaVO_3$ compared with the bare electron mass. "a" and "b" indicate intercepts at which tangential lines drawn from 0.4 eV and 0.15 eV cut the vertical axis, corresponding to the values of m_a and m_b. (b) m_a and m_b are plotted against the Sr content x.

width successively decreases. Then, the value of m^*/m_0 is expected to increase drastically reflecting the change of the U/W ratio. HOwever, it is clear from our observations that such a large mass enhancement does not actually take place in this system.

A.3.3. Spectral weight redistribution of 3d-band

The density of states (DOS) of orthorhombic $CaVO_3$ and cubic $SrVO_3$ calculated using the full-potential augmented plane-wave method with the local density approximation (LDA) are shown in the top of Fig. 7.9. The

TABLE 7.I. Effective mass m^*/m_0 deduced from the plasma frequencies ω_p and the generalized Drude model (m_a).

x	0	0.25	0.5	1
m^*/m_0 (deduced from ω_p)	3.9	3.7	3.5	3.3
m_a (generalized Drude analysis)	3.5	3.2	3.1	2.7

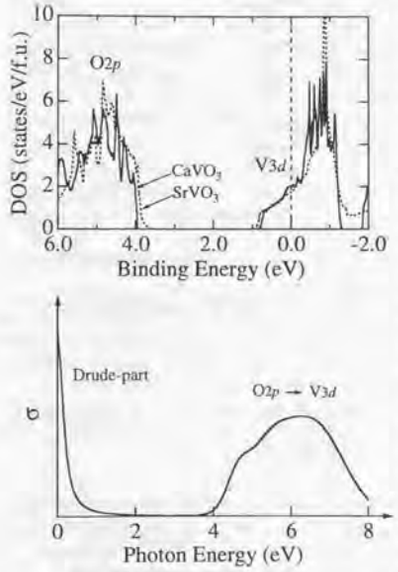

FIG. 7.9. DOS of $CaVO_3$ and $SrVO_3$ obtained by the LDA band calculation (top) and a schematic picture of optical conductivity expected from the calculated DOS (bottom).

band-calculation shows that the DOS near the Fermi level E_F is dominated by the V $3d$ electrons. The V $3d$ band crosses the Fermi level, and the DOS below 4 eV is mainly the O $2p$ band.

In the metallic state, $\sigma(\omega)$ is expected to consist of two basic components: intraband transitions within the V $3d$ conduction band, *i.e.*, the Drude part extending from $\omega = 0$, and interband transitions appearing at much higher energy. The latter is regarded from the calculated DOS as the charge-transfer contribution (an excitation from the O $2p$ band to the unoccupied part of the V $3d$ band above E_F). A corresponding schematic picture of the optical conductivity is shown in the bottom of Fig. 7.9. As seen in this picture, the charge-transfer contribution is expected to appear above ~ 4 eV, and the absorption edge of the charge-transfer transition in $SrVO_3$ is considered to shift slightly to lower energy than that of $CaVO_3$, reflecting the shift of the O $2p$ band.

Based on this picture, let us now look at the experimental results, Fig. 7.10 shows the real part of the optical conductivity, $\sigma(\omega)$, of the $Ca_{1-x}Sr_xVO_3$ single crystals (x=0, 0.25, 0.50, 1). The optical conductivity spectra are different from our naive schematic picture (Fig. 7.9 bottom); they show the presence of two anomalous features in the intraband transition part below 4 eV besides the Drude-like absorption (discussed above): a small peak which appears at ~ 1.7 eV and a large peak at ~ 3.5 eV. It must be noted that the two peak-like structures below 4 eV have no naive origin as far as we can infer from the calculated DOS (Fig. 7.9). This large spectral weight redistribution is generally believed to be a manifestation of the strong electron correlation in this system.

Fig. 7.11 shows a comparison of the optical conductivity spectra of $CaVO_3$ to those of other perovskite oxides, $Sr_{0.95}La_{0.05}TiO_3$

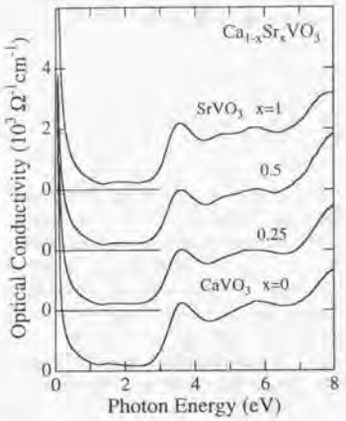

FIG. 7.10. Optical conductivity spectra of the $Ca_{1-x}Sr_xVO_3$ single crystals (x=0, 0.25, 0.50, 1) at room temperature obtained by the Kramers-Kronig transformation of the reflectivity data.

(lightly doped $3d^{0.05}$ metal),[23] and $YTiO_3$ ($3d^1$ insulator) reported by Okimoto *et al.*[8] In the optical conductivity of $Sr_{0.95}La_{0.05}TiO_3$, the most prominent low-energy feature, that distinctly rises around 4 eV, can be interpreted as originating in a transition from the O $2p$ band to the Ti $3d$ band, which corresponds to the optical gap of the parent insulator $SrTiO_3$.[24] The doped $3d$ electrons contribute to $\sigma(\omega)$ with a small spectral weight extending from $\omega = 0$. On the other hand, $YTiO_3$ is considered to be a Mott-Hubbard insulator. Two electronic gap-like features are observed around 1 eV and 4 eV. These features have been respectively interpreted as originating in excitations through the Mott-Hubbard gap, namely, from the lower-Hubbard band (LHB) to the upper-Hubbard band (UHB), and excitations through the charge-transfer gap, *i.e.*, from the O $2p$ band to the UHB.[8,25] Recently, Bouarab

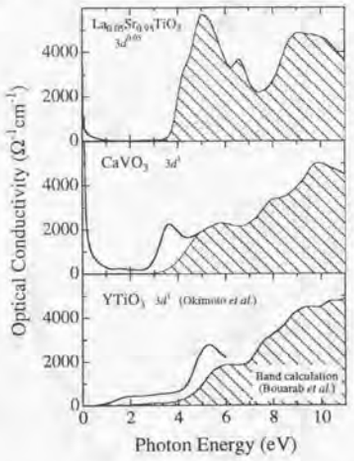

FIG. 7.11. Comparison of the optical conductivity spectra of $CaVO_3$ to those of other perovskite oxides, $Sr_{0.95}La_{0.05}TiO_3$ (lightly doped $3d^0$ metal),[23] and $YTiO_3$ ($3d^1$ insulator) reported by Okimoto *et al.*[8] Shaded portions correspond to the interband transition, and remaining white portions correspond solely to the intraband transitions within the V $3d$ band.

et al. have reported interband optical conductivities obtained by the energy-bands calculation of the YMO_3 (M=Ti-Cu) system with a local spin-density approximation.[26] Their calculated results of interband optical conductivity in $YTiO_3$ is shown in the bottom of Fig. 7.11 as a shaded portion. We find from this comparison that the peak at around 5 eV cannot be explained by the transition between the O $2p$ band and the Ti $3d$ band alone.

In $CaVO_3$, photoemission spectroscopy[15,27] has revealed that the O $2p$ band is located at a binding energy which is almost the same as that of metallic $Sr_{0.95}La_{0.05}TiO_3$; hence, the absorption edge of the charge-transfer excitation of $CaVO_3$ should be approximately equal to that of $Sr_{0.95}La_{0.05}TiO_3$. Therefore, it is

reasonable to consider that the shaded portions of $\sigma(\omega)$ in Fig. 7.11 correspond to the charge-transfer type transitions as well as the other interband transitions with much higher energies, by analogy with the band-calculation in $YTiO_3$.[26] Accordingly, the remaining white portions correspond solely to the intraband transition within the V $3d$ band.

In order to focus on the spectral weight of the optical conductivity arising from intra-$3d$-band transitions, we have subtracted the shaded portion in the middle of Fig. 7.11 as background, assuming an appropriate function of $(\omega-\Delta)^{3/2}$, where Δ has been obtained by fitting the lower energy tail of the O $2p$ band in photoemission spectroscopy spectra of $Ca_{1-x}Sr_xVO_3$ single crystals.[28]

A quantitative measure of the spectral weight has been obtained by deducing the effective electron number per vanadium ion defined by the following relation

$$N_{\rm eff}(\omega) \equiv \frac{2mV}{\pi e^2}\int_0^{\omega}\sigma(\omega')d\omega',$$

where e is the bare electronic charge and m is the bare band mass of a non interacting Bloch electron in the conduction band. V is the cell volume for one formula unit (one V atom in this system). The significance of $N_{\rm eff}$ will be appreciated by considering the sum rule of the conductivity

$$\int_0^{\infty}\sigma(\omega)d\omega = \frac{\pi Ne^2}{2mV}$$

where $N \equiv N_{\rm eff}(\infty)$ corresponds to the total number of electrons in the unit formula. That is, $N_{\rm eff}(\omega)$ is proportional to the number of electrons involved in the optical excitations up to ω. In Fig. 7.12, we show $N_{\rm eff}$ of the $Ca_{1-x}Sr_xVO_3$ system, after subtracting the higher-energy background. Since, in Fig 7.12, we have assumed $m = m_0$, where m_0 is the bare electronic mass, the total number $N \equiv N_{\rm eff}(\omega=\infty) \simeq N_{\rm eff}(\omega = 5$ eV) turns

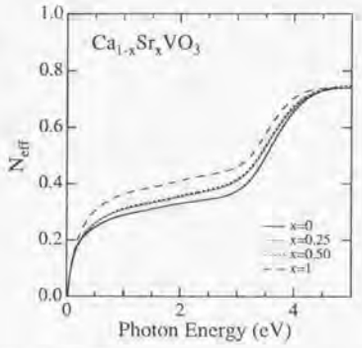

FIG. 7.12. Effective electron number per vanadium atom $N_{\rm eff}$ obtained after subtracting the higher-energy background (Fig. 7.11).

out to be smaller than 1, reflecting the difference between m and m_0 ($m > m_0$). If instead we use the value m obtained from LDA, $m \sim 1.5m_0$ for the V $3d$ band, we find $N_{\rm eff}(5$ eV$) \approx 1$. Thus, we conclude that the assumed background (shaded area in Fig. 7.11) is reasonable to deduce the intrinsic contributions of the interband transition.

The initial steep rise of $N_{\rm eff}$ is due to the Drude-like contributions extending from $\omega = 0$. The Drude-like contribution can be distinguished below $\sim$1.5 eV, where $N_{\rm eff}$ exhibits a flat region. Therefore, $N_{\rm eff}$ at $\sim$1.5 eV is considered to be a good measure for the effective mass of the carriers. The values of m^*/m_0 estimated from $N_{\rm eff}(\omega = 1.5$ eV) are 3.1(6), 3.0(5), 3.0, 2.7 for $x = 0$, 0.25, 0.50, 1, which are almost equivalent to the values of m^*/m_0 discussed in Sec. A.3.2.

Fig. 7.13 shows the optical conductivity spectra $\sigma(\omega)$ of the $Ca_{1-x}Sr_xVO_3$ single crystals (x=0, 0.25, 0.50, 1) in the photon energy range of 0$\sim$5 eV. The high-energy background corresponding to the interband transition has already been subtracted. As discussed above,

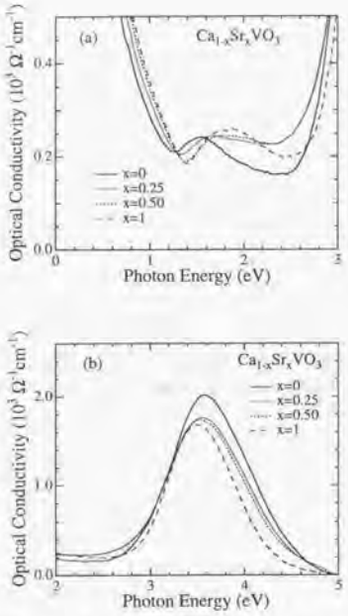

FIG. 7.13. Optical conductivity spectra of the $Ca_{1-x}Sr_xVO_3$ in the photon energy range of 0∼5 eV. The high-energy background corresponding to the interband transition has been subtracted. (a) a small peak at ∼1.7 eV is denoted as peak "A" in the text. (b) a large peak at ∼3.5 eV is denoted as peak "B" in the text.

$\sigma(\omega)$ $(0 \leq \omega \leq 5\text{eV})$ reflects only the intraband transitions of the V 3*d* electrons. In the spectrum, there is a small feature at ∼1.7 eV, which we call peak "A" [Fig. 7.13(a)] and also a large feature at ∼3.5 eV, which we call peak "B" [Fig. 7.13(b)]. With the increase of x, the excitation energy of peak "B" shifts slightly to lower energy, and its spectral weight decreases; whereas, the excitation energy of peak "A" shifts to higher energy, and its spectral weight increases. In addition, the width of peak "A" broadens with increasing x. Fig. 7.14 shows the excitation energy, the full-width at half maximum (FWHM), and the spectral weight of peak "A" and peak "B" as functions of x.[29]

In the valence band photoemission spectra of the $Ca_{1-x}Sr_xVO_3$ system, two features have been observed: one is a peak at ∼1.5 eV below E_F and the other is the emission from a broad quasiparticle band which lies on E_F.[15,27] The former is assigned to an incoherent emission associated with the formation of the lower Hubbard band and the latter corresponds to a renormalized 3*d* band at E_F. We reported that, upon increasing the strength of U/W in $Ca_{1-x}Sr_xVO_3$ system, the spectral weight is systematically transferred from the quasiparticle band to the incoherent part.[15] In the inverse-photoemission spectra of $CaVO_3$ and $SrVO_3$, Morikawa *et al.* have found a prominent peak at 2.5∼3 eV above E_F and a shoulder within around 1 eV of E_F.[27] These features have been also assigned to the incoherent and coherent parts of the spectral function of the V 3*d* electron.

These results lead us to consider that the two features (peaks "A" and "B") observed in the optical conductivity spectra originate from possible combinations of the transitions among the incoherent and coherent features of V 3*d* electron around the Fermi level.

The experimental results of the optical conductivity can be compared to the theoretical prediction obtained by the self-consistent local-impurity approximation of the infinite-dimension Hubbard model.[12] The theory seems to give us a clue to understand the origin of the two features. According to the prediction, the optical response is composed of basically three contributions in addition to the Drude part: a broad part centered at a frequency $\omega = U$, a few narrow features near $\omega = U/2$, and an "anomalous" part that is present in the range $\omega = 0$ to 1 eV approximately. The contribution at U corresponds to direct excitations between the Hubbard bands, the features at $U/2$ corresponds to excitations from the LHB to the empty part of the quasiparticle band and from the filled part of the quasiparticle band to the UHB, and finally, the "anomalous" part corresponds to excitations from the filled to the empty part of the quasiparticle band. In our previous paper,[30] we analyzed the spectrum of $CaVO_3$ in the light of these predictions. The parameters U and W, which were used in the model calculation, were taken from the results of photoemission spectroscopy.[30] Although it was expected that the parameter W would systematically change with composition, we chose to vary U for the sake of simplicity, given that fits of equivalent quality could be obtained for the photoemission spectra. In $CaVO_3$, which has the narrowest 3*d* band in the $Ca_{1-x}Sr_xVO_3$ system, the peaks "A" and "B" have been well described by the features at $U/2$ and U, respectively, so that the infinite-dimension Hubbard model seems to reproduce the experimentally obtained optical conductivity reasonably well.[30]

We find that our experimental gives results as summarized in Fig. 7.14: with increasing x, the peak energy of peak "B" shifts slightly to lower energies and its spectral weight gradually increases. The spectral weight of peak "A" increases with x. Peak "A", however, shifts slightly to higher energy. We should now like to emphasize an important point. Our present systematic study of the $Ca_{1-x}Sr_xVO_3$ compound gives conclusive evidence that we can tune the band-width of the system by controlling x. The position of peak "B" gives a direct measure of the value of U, and the fact that it remains almost a constant is a clear evidence that the ratio U/W is controlled by a change of the band-width W. This situation is in sharp contrast with our previous analysis[30] based on photoemission data which did not allow us to resolve

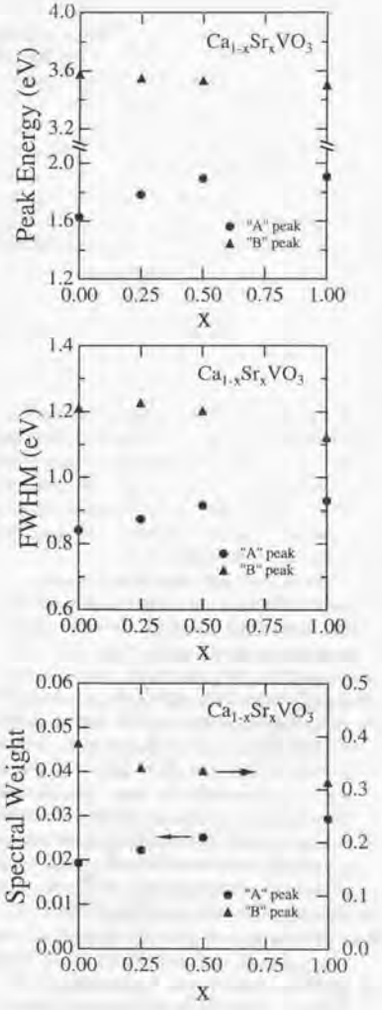

FIG. 7.14. Excitation energy, full-width at half maximum (FWHM), and spectral weight of peak "A" and peak "B" plotted as functions of x.

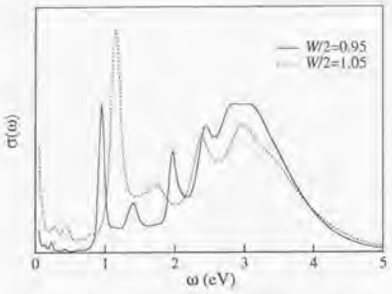

FIG. 7.15. Calculated optical conductivity by IPT for the parameters $U = 3$ eV and W indicated in the figure.

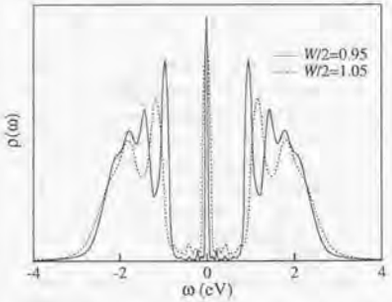

FIG. 7.16. Theoretical spectral density of states obtained by IPT at $T = 0$ for the parameters $U = 3$ eV and W indicated in the figure.

which parameter was actually controlling the U/W ratio. A crucial ingredient that makes the study of the optical response so valuable for this analysis is that, unlike photoemission, it probes also the unoccupied part of the spectra, therefore, it is sensitive to the relative position of the Hubbard bands.

In order to gain some further insight in the qualitative behavior of the systematic evolution of our experimental data, we have used our initial estimates for U and W as input parameters in a calculation of the optical response of the Hubbard model and changed the value of W instead of U. We shall consider the model within the dynamical mean field theory which becomes exact in the limit of large lattice connectivity (or large dimensionality). For convenience we have computed the optical response using the iterated perturbation theory (IPT) method which allows for a simple evaluation of this quantity at $T = 0$ and near the Mott-Hubbard transition.[31,32]

In Fig. 7.15 we show the theoretical prediction using the value of $U = 3$ eV for the local repulsion and for the half-bandwidth $W/2 = 1.05$ and 0.95 eV for $SrVO_3$ and $CaVO_3$, respectively. Note that the spectra do not display the Drude contribution as it corresponds to a delta-function at $\omega = 0$ since our model does not contain disorder and the calculation is performed at $T = 0$. The particular lineshape that we obtain is originated in the behavior of the spectral density of states that is obtained within the IPT method as shown in Fig. 7.16. We should point out that while the details of the line shape may not be correctly given by this method, the main distribution of the spectral weight of the various contributions and their systematic evolution are very reliably captured.[12]

We observe that the theoretical results for the systematic dependence of the various contributions to the optical response by controlling the value of W are in a better qualitative agreement with the experimental data of Fig. 7.14 than the previous calculation where we changed the value of U. One of the most notable improvements is that the unexpected systematic evolution of the feature at $U/2$, which shifts upward with increasing W, is well captured qualitatively. This peculiar effect can be interpreted as a "band repulsion" between the Hubbard band and the quasiparticle band. As we increase W, the latter becomes broader and "pushes" the Hubbard band further out.

However, there are still some discrepancies. Such a large spectral weight redistribution is predicted to be concomitant with a large effective mass in the mean-field treatment of the Hubbard model.[12,33] This is, however, inconsistent with the observed effective mass in this system. Moreover, in the optical conductivity spectra, there is apparently a notable discrepancy in respect to the relative spectral weight of peak "A" to peak "B"; it is much more suppressed in the experimental data, than in the theoretical data.

Other discrepancies between some experimental results and the prediction of the mean-field approach for the electron correlation were also reported in the photoemission spectroscopy measurements in this system.[15,27] In the mean-field Fermi liquid approach, the renormalized quasiparticle band at E_F should be narrowed with increasing the value of U/W,[12,33] but, in those experiments, the quasiparticle band-width remains broad, even if the system approaches the Mott transition. Since peak "A" has been assigned to transitions associated with the quasiparticle band, the conspicuous suppression in spectral intensity of peak "A" reflects the broadness of the quasiparticle band. The broad quasiparticle band also accounts for the lack of a strong mass enhancement in this system.

The momentum-dependent self-energy becomes significant near the Mott transition, resulting in a reduction of the mass enhancement. Although our measurements cannot clarify the validity of introducing a momentum-dependent self-energy, we conclude that there must be other interactions not present in the mean-field treatment of the electron correlation in the metallic regime close to the Mott transition.

Finally, the presence of the "anomalous" contribution at low frequencies that extends down to $\omega = 0$ in the theoretical data sheds a different light for the interpretation of the Drude-like response discussed in Sec. A.3.2. It may be possible to say that the deviation from the simple Drude model would be partly due to this "anomalous" contribution. The origin of this effect is again traced to the presence of the incoherent contribution coming from the low energy tails of the Hubbard bands that is observed in the theoretical density of states. However, it is experimentally very difficult to disentangle unambiguously the contribution of the coherent optical response of carriers and that of the incoherent process in optical conductivity, so this issue remains an open question.

A.4. Summary

This study has aimed at elucidating the electronic structure of the correlated metallic vanadate by means of the optical spectroscopy measurements. We have synthesized the $Ca_{1-x}Sr_xVO_3$ system to control solely the $3d$ band-width without varying the band filling.

We have found that the low energy contribution to the optical conductivity spectra cannot be reproduced by the simple Drude model with the energy-independent scattering rate and effective mass. The energy-dependent $\gamma(\omega)$ determined by the generalized Drude model shows relatively large energy dependence. However, $\gamma(\omega)$ is proportional to ω rather than that of the electron-electron scattering ω^2.

The effective mass of the V $3d$ electron has been evaluated from the plasma frequency. The value of m^*/m_0 gradually increases with decreasing the band-width W. However, any symptom of the critical mass enhancement has not been observed, even though the system is close to the Mott transition.

We observed two anomalous peaks in the optical conductivity spectra around 1.7 eV and 3.5 eV. These features can be assigned to the possible combinations of transitions be-

tween the incoherent peaks and the coherent quasiparticle band around the Fermi level. This large spectral weight redistribution substantiates the strong electron correlation in this system, which is, however, not concomitant with a large effective-mass enhancement.

---

[1] N. F. Mott, *Metal Insulator Transitions, Second Edition* (Taylor and Francis, London 1990).

[2] Y. Fujishima, Y. Tokura, T. Arima, and S. Uchida, Phys. Rev. B **46**, 11167 (1992).

[3] Y. Taguchi, Y. Tokura, T. Arima, and F. Inaba, Phys. Rev. B **48**, 511 (1993).

[4] M. Kasuya, Y. Tokura, T. Arima, H. Eisaki, and S. Uchida, Phys. Rev. B **47**, 6197 (1993).

[5] D. A. Crandles, T. Timusk, J. D. Garrett, and J. E. Greedan, Phys. Rev. B **49**, 16207 (1994).

[6] T. Katsufuji, Y. Okimoto, and Y. Tokura, Phys. Rev. Lett. **75**, 3497 (1995).

[7] D. A. Crandles, T. Timusk, and J. E. Greedan, Phys. Rev. B **44**, 13250 (1991); D. A. Crandles, T. Timusk, J. D. Garrett, and J. E. Greedan, Physica C **201**, 407 (1992).

[8] Y. Okimoto, T. Katsufuji, Y. Okada, T. Arima, and Y. Tokura, Phys. Rev. B **51**, 9581 (1995).

[9] G. A. Thomas, D. H. Rapkine, S. A. Carter, A. J. Millis, T. F. Rosenbaum, P. Metcalf, and J. M. Honig, Phys. Rev. Lett. **73**, 1529 (1994); G. A. Thomas, D. H. Rapkine, S. A. Carter, T. F. Rosenbaum, P. Metcalf, and D. F. Honig, J. Low Temp. Phys. **95**, 33 (1994).

[10] M. J. Rozenberg, G. Kotliar, H. Kajueter, G. A. Thomas, D. H. Rapkine, J. M. Honig, and P. Metcalf, Phys. Rev. Lett. **75**, 105 (1995).

[11] J. Zaanen, G. A. Sawatzky, and J. W. Allen, Phys. Rev. Lett. **55**, 418 (1985).

[12] A. Georges, G. Kotliar, W. Krauth, and M. J. Rozenberg, Rev. Mod. Phys. **68**, 13 (1996).

[13] I. H. Inoue, K. Morikawa, H. Fukuchi, T. Tsujii, F. Iga, and Y. Nishihara, Jpn. J. Appl. Phys. **32**, 451 (1993).

[14] I. H. Inoue, O. Goto, H. Makino, N. E. Hussey, and M. Ishikawa, Phys. Rev. B. **58**, 4372 (1998)

[15] I. H. Inoue, I. Hase, Y. Aiura, A. Fujimori, Y. Haruyama, T. Maruyama, and Y. Nishihara, Phys. Rev. Lett. **74**, 2539 (1995).

[16] A. Fukushima, F. Iga, I. H. Inoue, K. Murata, and Y. Nishihara, J. Phys. Soc. Jpn. **63**, 409 (1994).

[17] N. Shirakawa, K. Murata, H. Maikino, F. Iga, and Y. Nishihara, J. Phys. Soc. Jpn. **64**, 4824 (1995).

[18] B. L. Chamberland and P. S. Danielson, J. Solid State Chem. **3**, 243 (1971).

[19] M. Couzi and P. V. Huong, J. Chim. Phys. **69**, 1339 (1972).

[20] J. W. Allen and J. C. Mikkelsen, Phys. Rev. B **15**, 2952 (1977).

[21] B. C. Webb, A. J. Sievers, and T. Mihalisin, Phys. Rev. Lett. **57**, 1951 (1986).

[22] In fact, we should take into account a small contribution of a peak around 1.7 eV in the $\epsilon_1(\omega)$ spectra. The peak corresponds to "A" peak in the optical conductivity. But here, we have disregarded the small peak.

[23] H. Makino *et al.*, unpublished.

[24] M. Cardona, Phys. Rev. **140**, A651 (1965).

[25] T. Arima, Y. Tokura, and J. B. Torrance, Phys. Rev. B **48**, 17006 (1993).

[26] S. Bouarab, A. Vega, and M. A. Khan, J. Phys.: Condens. Matter **9**, 6267 (1997).

[27] K. Morikawa, T. Mizokawa, K. Kobayashi, A. Fujimori, H. Eisaki, S. Uchida, F. Iga, and Y. Nishihara, Phys. Rev. B **52**, 13711 (1995).

[28] I. H. Inoue, H. Makino, I. Hase, Y. Aiura, Y. Haruyama, and Y. Nishihara, Physica B **230-232**, 780 (1997).

[29] We have divided peaks "A" and "B" by fitting the $\epsilon_2(\omega)$ data with two Gaussians. And the spectral weight has been defined as an amount of the contribution to $N_{\rm eff}(\omega)$ from peak "A" and from peak "B".

[30] M. J. Rozenberg, I. H. Inoue, H. Makino, F. Iga, and Y. Nishihara, Phys. Rev. Lett. **76**, 4781 (1996).

[31] A. Georges and G. Kotliar, Phys. Rev. B **45**, 6479 (1992).

[32] X. Y. Zhang, M. J. Rozenberg and G. Kotliar, Phys. Rev. Lett. **70**, 1666 (1993).

[33] W. F. Brinkman and T. M. Rice, Phys. Rev. B **2**, 4302 (1970).